Trinity College Dublin
Coláiste na Tríonóide, Baile Átha Cliath
The University of Dublin

Theoretical Insights into Ammonia Production and Conversion via Heterogeneous Catalysis

by

Kevin Brennan

under the supervision of

Prof Max García-Melchor

A thesis submitted in partial fulfilment

of the requirements for the degree of

Doctor of Philosophy

at the

University of Dublin, Trinity College

2024

Declaration of Authorship

I declare that this thesis has not been submitted as an exercise for a degree at this or any other university and it is entirely my own work.

I agree to deposit this thesis in the University's open access institutional repository or allow the Library to do so on my behalf, subject to Irish Copyright Legislation and Trinity College Library conditions of use and acknowledgement.

I consent to the examiner retaining a copy of the thesis beyond the examining period, should they so wish (EU GDPR May 2018).

Kevin Brennan

31/03/2024

Trinity College, The University of Dublin

Summary

The actualisation of the electrochemical synthesis of ammonia from atmospheric nitrogen is a long-term goal for transitioning into a green and sustainable economy. However, it is just that, long-term. Electrochemical nitrogen reduction is hindered by the challenging activation of the nitrogen bond. Moreover, it is a linear process. The transition to a purely circular economy is regarded as a priority for the European Union and as such, waste products should be viewed as a valuable resource, and in the case of ammonia synthesis they are. Such waste involves already fixed nitrogen, immediately avoiding the issue of nitrogen activation. The field of nitrate reduction is well established in the literature, and using that as a proof of concept, we endeavour to examine the much less investigated reduction of cyanide, with the intent to drive interest in a circular economy. We also investigate the short-term solution to the energy crisis that is the blue nitrogen economy, wherein blue ammonia produced by the Haber-Bosch process is used as a chemical storage unit for hydrogen. As such we study, through theoretical methods, ammonia decomposition catalysts, one of the bottlenecks of this process.

We employ periodic density functional theory calculations to first investigate the reduction of cyanide on a nickel cathode. We reveal that the formation of the major product, methylamine, over the much more desired minor products, methane and ammonia, is due to the desorption of methylamine. This suggests, that should we manage to stabilise methylamine on the cathode, then methane and ammonia formation could occur. We also investigate the reduction of cyanide via sourcing hydrogen atoms from the surface coverage which reveals a pathway wherein we decouple the formation of the minor products, first producing ammonia, and then in a separate step, methane. Additionally, this mechanism foregoes the production of methylamine, hinting at complete faradaic efficiencies towards the minor products.

This pathway is inhibited by the presence of a large transition state which may be avoided by the inclusion of water, which shuttles hydrogen from the surface towards the *CN intermediate, resulting in *CNH. The inclusion of a solvent water molecule prompted the studying of the various methods used to account for the solvent in theoretical calculations. In particular, we model the electrochemical reduction of hydrogen cyanide using both implicit and explicit solvation models, with the dual purpose of comparing solvation

models, as well as uncovering the role of the solvent in the reduction mechanism. We find that, while the implicit solvent model results in negligible changes, the inclusion of explicit solvent allows for drastic differences compared to the same reaction calculated under vacuum conditions. We note an absence of chemisorbed intermediates due their competing interactions between the cathode and the explicit solvent. The explicit solvent also allowed for the investigation of some of the kinetics involved in the hydrogenation of HCN, revealing the metastable CHNH intermediate, which undergoes a Grotthuss mechanism to give the CH_2N intermediate. The discovery of these intermediates as well as the overall change in binding modes highlights the need to account for site-specific interactions between the substrate and the solvent environment. We have also accounted for the applied electrochemical potential, sampling both zero and reducing potentials, in the reduction of hydrogen cyanide. This investigation yielded two intermediates that appeared to be independent of the applied potential. Applying reducing potentials also induced several changes in geometry, most notably the lone pairs of intermediates being directed away from the negatively charged cathode, a feature which is not accounted for through constant charge models.

In Chapter 6 we endeavoured to investigate the decomposition of ammonia on a MOF derived iron catalyst (Fe@C), a material that is comprised of metallic iron, iron oxides and iron carbides, developed by the group of Prof. Jorge Gascon from the King Abdullah University of Science & Technology. This material achieved high conversions of ammonia when irradiated with light and at low temperatures, whereas in the absence of light much higher temperatures were needed to convert ammonia. The simulation of Fe@C involved two surface models, namely metallic Fe and Fe_3O_4. We find that the decomposition of ammonia on metallic Fe has a rate determining step with an activation energy of 2.00 eV, in good agreement with the experimentally derived value. Additionally, an energy sink, generated upon the full dehydrogenation of ammonia, disappears at temperatures matching the experimental onset temperature. We also report our findings regarding Fe_3O_4, which was found to be able to localise an extra electron in an approximation to light, and in doing so raised the thermodynamic profile of all intermediates which resulted in decreasing the effective barrier for N–H cleavage. As such, we attribute the activity of Fe@C in the absence of light to the metallic Fe phase and its activity at low temperatures under light irradiation to Fe_3O_4.

Abstract

The global population is heavily dependent upon the production of ammonia via the Haber-Bosch process. This is an environmentally unfriendly process that demands pure hydrogen, obtained from the steam reforming of methane. As such there is an incentive to move to more sustainable procedures such as the electrochemical reduction of atmospheric nitrogen to ammonia. This process, however, is limited by the difficult activation of nitrogen, as well as competition with the evolution of hydrogen. We circumvent the first issue by reducing a different substrate that is an already fixed form of nitrogen, cyanide, towards methane and ammonia. The reduction of nitrates to ammonia serves as a proof of concept, and if the world intends to move to a circular economy, then investigating the reduction of cyanide is a necessity. This thesis begins by shedding light on the possible mechanisms of cyanide reduction through theoretical calculations. These reaction mechanisms serve as a foundation upon which we add layers of detail to our calculations, such as the inclusion of implicit and explicit solvation models, or the external applied potential. The final chapter of this thesis then delves into the photo-thermal decomposition of ammonia for chemical hydrogen storage. This is presented as a short-term solution to the energy crisis, wherein blue ammonia is still produced by the Haber-Bosch process and employed as an energy vector.

Acknowledgements

Firstly, I would like to thank my supervisor Prof. Max García-Melchor for all his support, guidance and especially his patience throughout my PhD. I would also like to thank Prof. Graeme Watson for his advice, particularly regarding the modelling of oxides and the dangers of bread. I cannot overstate how fortunate I am to have two such experts overseeing my PhD.

I have also been incredibly lucky to have made some incredible friends as part of the CCEM group, without whom the PhD would have been a much poorer experience: Eric, Michael, Arantxa, Cian, Timo, Manting, Marconi, Jody, Alejandro, and Mattia. A special thank you goes out to Anna, my next-door neighbour, agony aunt, and my partner in crime in VASP.

I would also like to thank the Provost's PhD fund and the Science Foundation Ireland, who generously funded this PhD, as well as the Higher Education Authority and Trinity College Dublin who allowed an extension of my PhD due to Covid.

The calculations performed in this thesis would not have been performed without the resources of several organisations. With that in mind I would like to thank the TCHPC, ICHEC and KAUST HPC staff for the work they do maintaining the compute clusters and for their support and patience when dealing with my various requests.

I'd like to thank my family for their support and encouragement throughout my education (and before it as well). I'd also like to thank them for putting up with me throughout the PhD experience. I'd also like to thank Lucy, who is factually the best dog in the world, for being excited to see me every time I came home.

And lastly, but certainly not least, I'd like to thank my girlfriend, Shannon, who for 11 years has encouraged me, supported me and has picked me up when I was down. Without you there is no chance I would have started a PhD, let alone finish one, so thank you so much.

Publications

K. Brennan, G. W. Watson and M. García-Melchor, *Catalysis Science & Technology*, 2021, **11**, 5633–5640.

K. Brennan, G. W. Watson and M. García-Melchor, *Catalysis Science & Technology*, 2024, **14**, 1043–1051.

A. Sousa, D. Mateo, L. Garzon-Tovar, K. Brennan, N. Morlanés, J. C. Navarro, X. Wang, J. Ruiz-Martinez, M. García-Melchor, J. Gascon, *Manuscript submitted for peer review.*

List of Abbreviations

BCC	Body-Centred Cubic	MvK	Mars-van Krevelen
CHE	Computational Hydrogen Electrode	NEB	Nudged Elastic Band
CI–NEB	Climbing Image Nudged Elastic Band	NHE	Normal Hydrogen Electrode
DFT	Density Functional Theory	PCET	Proton Coupled Electron Transfer
eCNRR	Electrochemical Cyanide Reduction Reaction	PDS	Potential Determining Step
eHCNRR	Electrochemical Hydrogen Cyanide Reduction Reaction	PES	Potential Energy Surface
eN_2RR	Electrochemical Nitrogen Reduction Reaction	RDS	Rate Determining Step
FCC	Face-Centred Cubic	RHE	Reversible Hydrogen Electrode
GGA	Generalised Gradient Approximation	SCF	Self-Consistent Field
HF	Hartree Fock	SHE	Standard Hydrogen Electrode
HER	Hydrogen Evolution Reaction	SIE	Self-Interaction Error
LDA	Local Density Approximation	TS	Transition State
$Li–N_2RR$	Lithium Mediated Electrochemical Nitrogen Reduction Reaction	vdW	Van der Waals
MEP	Minimum Energy Path	ZPE	Zero-Point Energy

Table of Contents

Chapter 1 Introduction

The colour green has many connotations. It is the colour of nature, of chlorophyll. It is also the colour of money and profit. Ultimately it is still a colour, a pre-existing concept, unchanged by these symbolic associations. Similarly, green chemistry is not a new field of chemistry, rather it is a conscious steering of science towards the sensible idea of prevention being better than the cure. The concept is defined, by Paul Anastas and John Warner in their seminal book, *Green Chemistry: Theory and Practice*, as "the utilisation of a set of principles that reduces or eliminates the use or generation of hazardous substances in the design, manufacture and application of chemical products".[1] The development of green technologies is now of the utmost importance due to the current climate crisis.

Unfortunately, green chemistry practices need to be profitable before they are ever implemented. The green synthesis of adipic acid, essential for the manufacturing of nylon, is a particularly illustrative example of this concept. This synthesis was done via the direct oxidation of cyclohexane by hydrogen peroxide, avoiding the use of solvent, corrosive nitric acid, and also, the production of waste N_2O.[2] However, H_2O_2 itself is more expensive than the product, meaning this synthesis will never be financially viable unless incentivised by economic actions.

Regardless of how effective green chemistry is at reducing waste, it is still limited by the confines of the current linear economic system. A *linear economy* is a system that uses a process to convert a resource into a product while discarding any waste product. As is evident with the current climate crisis, the "throwing away" of waste products is not feasible in the long term, and consequently, we must transition to a *circular economy*. This model views waste as a valuable resource and strives to reuse all compounds involved in a synthesis, resulting in a "net-zero waste" process. The adapting of a linear "take-make-dispose" process to be circular is commonly referred to as "closing the loop", and is regarded as a top priority by the European Commission in the EU Circular Economy Action Plan (EU CEAP).[3] In fact, it has been estimated that at the current rate of consumption, by 2050 the equivalents of three Earth's will be required to meet the demand.[4]

For every industrial process, there is a multitude of moving parts which all need to be optimised relative to each other, a daunting task. In this PhD thesis, I have focused my

efforts on investigating ammonia synthesis and decomposition processes to contribute to a circular, nitrogen economy.

1.1 Nitrogen Reduction to Ammonia

1.1.1 The Haber-Bosch Process

Fritz Haber received the Nobel Prize in 1918 for the synthesis of ammonia from its elements. In his Nobel lecture he credited his motivation to the ever-increasing demand for food and the need to supplement crops with synthetic nitrogen sources.[5] Prior to this, feeding the ever growing global population was seen as a serious concern by the chemical community with the then president of the British Association for the Advancement of Science, Sir William Crookes stating that, "*England and all civilised nations stand in deadly peril of not having enough to eat*".[6] Thus began an international race to fix atmospheric dinitrogen which attracted many notable chemists such as Le Chatelier, Ostwald and Nernst, though it was Fritz Haber who prevailed. Originally, Haber produced small amounts of ammonia directly from gaseous nitrogen and hydrogen at a temperature of 1,000 ºC and at atmospheric pressure using an iron catalyst.[7] With the help of Carl Bosch, large conversions of nitrogen were achieved by combining gas recycling and an osmium catalyst at 500 ºC and 200 atm. Shortly after, Alwin Mittasch ran a large scale screening of catalysts and discovered that a cheaper multicomponent catalyst comprised of magnetite and aluminium oxide displayed high activity.[8] Since this development by Mittasch, little has changed in the industrial synthesis of ammonia.

While the synthesis of ammonia has fed billions around the world, it is also responsible for the death of millions. The mass production of ammonia allowed for Germany to churn out massive quantities of explosives and munitions, extending the length of World War 1 by an estimated two years. Haber's legacy as the man who fed the world would be tarnished by his active role in the war by advocating for the use of, and leadership in developing the field of chemical warfare.[9]

Prior to the work of Haber and Bosch, processes for nitrogen fixation were widely regarded as inefficient for industry. The Birkeland-Eyre method of nitrogen fixation involved the conversion of air to nitric oxide, an appreciable yield of which would require temperatures of 3,000 K, which was achieved at the time by the generation of an electric arc.[6] Another

method, the Frank-Caro process, entailed the synthesis of calcium cyanamide from calcium carbide and atmospheric nitrogen.[6] The product of this could be directly used as a fertiliser, although temperatures of 2300 K were still necessary for its synthesis. The method developed by Fritz Haber and Carl Bosch revolutionised the field of nitrogen fixation. Ammonia synthesis via the Haber-Bosch process is given as:[10]

$$N_2(g) + 3H_2(g) \rightarrow 2NH_3(g) \quad \Delta H^0_{298\,K} = -92\ kJ\ mol^{-1} \tag{1.1}$$

The fact that this is an exothermic reaction means that low temperatures should favour ammonia production. However, N_2 has an incredibly high bond dissociation energy (BDE) of 941 kJ mol^{-1} and is regarded as one of the most stable molecules in chemistry.[11] Because of this, high temperatures are needed to favour the dissociative adsorption of N_2 and provide a reasonable rate of production for industry. The application of high temperature, however, shifts equilibrium towards the reactants, explaining the need for high pressures of reactants to shift the equilibrium to the product.

The need for H_2 is another drawback for the Haber-Bosch process, giving rise to huge amounts of greenhouse gases being released. The pure hydrogen gas necessary for the reaction is supplied by the application of the steam reforming of methane followed by use of the water gas shift reaction.

$$CH_4 + H_2O \rightleftharpoons CO + 3H_2 \tag{1.2}$$

$$CO + H_2O \rightleftharpoons CO_2 + H_2 \tag{1.3}$$

Hydrogen sourced in this manner is referred to as grey hydrogen. Consequently, apart from atmospheric nitrogen, the main feedstocks for the ammonia industry are natural gas and coal, fossil fuels. Along with their use in Eqs. 1.2 and 1.3, fossil fuels are used to maintain the temperatures needed for N_2 activation. Current NH_3 production stands at *ca.* 170 million tonnes a year, a figure that is expected to increase with the rising demand of the global population.[12] On average, for every ton of NH_3 synthesised 2.86 tons of CO_2 are generated, accounting for 1.44% of global CO_2 emissions.[13]

As the mass production of NH_3 is a necessity, its reaction mechanism has been scrutinised over the course of a century to optimise the process. The Haber-Bosch process is a relatively simple reaction and as a result, the nature of the catalyst and the reaction mechanism has been the focus of much research. Industrial NH_3 synthesis follows the Langmuir-

Hinshelwood mechanism (LH), where both N_2 and H_2 dissociate and are adsorbed onto the surface of the catalyst before any reaction occurs.[14] The rate determining step (RDS) has been found to be the dissociative adsorption of nitrogen on to the industrial iron catalyst surface.[15] Regarding industry, the most commonly used catalyst is a multicomponent one, where magnetite (Fe_3O_4) is fused with oxides, usually K_2O, Al_2O_3 and CaO. Some plants however, use a Ru-based catalyst, which displays a greater activity but is more expensive and less robust.[16] The role of the aluminium and calcium oxides is very similar, in that they are both reported to dissolve in the magnetite lattice and prevent sintering. On the other hand, the presence of Al_2O_3 has been found to decrease the catalyst pore size while increasing porosity ultimately increasing internal surface area of the catalyst,[17] while K_2O has a much more different role. In particular, the presence of adsorbed potassium atoms on the surface of the iron catalyst aids in dissociative nitrogen adsorption, however adsorbed potassium would not stand up to the intense temperatures required by the Haber-Bosch process.[18,19] As such it is thought that a composite layer of Fe, O and K is the chemical state of the promoter as opposed to any bulk potassium compound.[18] The adsorption of oxygen alone is reported to inhibit nitrogen adsorption, explaining the modest effect of the potassium promoter when in this composite form.[20]

Despite a century of study, there has been very few changes in the Haber-Bosch process since the contribution made by Mittasch. Current reaction conditions in industrial Haber-Bosch plants remain at 500 ºC and 200 atm, and an iron catalyst is still employed.[21] With the ongoing climate change crisis, ammonia synthesis as an industry is in dire need of change and new technology. Fortunately, a large portion of the academic community is agreed upon this fact with a vast amount of research dedicated to alternate means of producing ammonia, as outlined below.

Ultimately, the Haber Bosch process is an excellent example of a process that satisfies some of the principles of green chemistry, namely by using a cheap and robust catalyst for increased energy efficiency, yet it is still unsustainable. As we will see later, the industrial synthesis of ammonia has had an unforeseen and debilitating impact on the nitrogen cycle.

1.1.2 Alternative Methods for Ammonia Production using H_2 gas

Several efforts have been made to replace the Haber-Bosch process with a sustainable or less environmentally damaging process. The area of ammonia synthesis is one of the most

varied in the field of catalysis with several different approaches and methods being developed.

Chemical looping combustion (CLC) is a process employed to convert fossil fuels to electricity and allow for carbon capture without any loss in efficiency. CLC occurs between two reactors, namely a fuel and an air reactor. An oxygen carrying species, usually a metal oxide, provides the oxygen for combustion within the fuel reactor. The now reduced metal oxide is then transferred to the air reactor where it is oxidised again before being reintroduced to the fuel reactor again. Using only oxygen without any of the trace impurities or nitrogen found in air allows for the production of nitrates and other pollutants to be avoided. This process outputs a stream of CO_2 and H_2O which is easy to separate allowing for efficient carbon capture.

The same logic has been employed to reduce atmospheric nitrogen and create ammonia. Methods have been developed where N_2 is reduced via a metal oxide to give a nitride, which is then followed by reduction with hydrogen supplied by either dihydrogen or water. Both of these processes can be done at atmospheric pressure, albeit temperatures of over 550 and 1,000 ºC are required respectively.[22,23] It should be noted that this process is still being refined, with reports of alkali and alkaline-earth metal hydrides working in conjunction with transition metals to synthesise ammonia from its elements. These transition metal hydride mixtures are prepared via ball milling and allow for ammonia to be synthesised at 350 ºC.[24]

The mechanochemical method in which these mixtures are prepared has itself been applied to the area of ammonia synthesis. Though a relatively new field, ball milling mechanochemistry is expanding into almost every area of chemistry, from the Suzuki C–C cross-coupling reaction to creating metal-organic frameworks.[25,26] Ball milling has shown great promise for feasible ammonia production via the use of iron powder as a catalyst.[27] Steel balls and iron powder are loaded into the mill reactor, which is then sealed and flooded with N_2 gas. Ball milling then occurs, where the iron powder is ground and pulverised allowing for high defect densities to be obtained. The low coordination defects generated are considered as very active sites for the dissociative adsorption of N_2. The reactor is then filled with H_2 gas. Adsorbed nitrogen is then hydrogenated during ball milling to give adsorbed NH_3 species, followed by its desorption with the aid of mechanical heat generated

by ball milling. In this manner, NH_3 concentrations of 82.5 vol% were obtained at 1 bar and 45 ºC.[27] While, this method does show great promise it does not address the issue of H_2 generation by steam reforming of methane.

In the same vein as mechanochemistry, plasma-enabled catalysis addresses the challenging bottleneck that is N_2 activation. However, while mechanochemistry deals with the catalyst, plasma-enabled catalysis revolves around treating the N_2 gas. Promoting a reactant gas into a less stable excited state may reduce the price tag associated with activation, without altering or influencing any subsequent steps in the reaction.[28] Weakly ionising nitrogen gas by electrical discharge generates a non-thermal plasma, rich in both electronic and vibrational excited states. It has been shown that the mechanism of NH_3 synthesis via plasma enabled catalysis does not affect the subsequent NH_x hydrogenation steps or desorption, rather only the dissociative adsorption of the plasma-induced excited N_2 gas.[29] While displaying great potential in tackling the bottleneck of N_2 activation, the large environmental issue involved in supplying hydrogen is still not addressed by this method.

The majority of greenhouse gas emissions associated with the Haber Bosch process is due to the use of grey hydrogen. As such, there is the possibility of employing green hydrogen, hydrogen sourced from water electrolysis powered by renewable energy sources, so as to make the Haber Bosch process more environmentally friendly. Ammonia produced in this manner is referred to as green ammonia. However, this technology is limited by the efficiency of current electrolysers. Three main electrolyser types exist, alkaline water electrolysers (AWE), proton exchange membrane water electrolysers (PEM WE), and solid oxide water electrolysers (SOWE). The choice of electrolyser is dependent upon the specific needs of the green ammonia plant in question. For example, an ammonia plant that is powered via energy sources that can fluctuate very rapidly, *i.e.*, wind or solar power, PEM WEs may be employed, due to their capacity to operate at higher densities (*ca.* 2 A cm^{-1}) during peak weather conditions, thereby maximising H_2 production and minimising any energy losses.[30,31] Conversely, at off-peak weather conditions, PEM WEs may operate at lower current densities. However, the current state of the art PEM WEs are composed of precious metals, namely platinum and iridium, which limits their widespread usage.[32,33] SOWEs are accruing interest due to their dependence earth abundant materials, namely zirconia, yttria, nickel and steel, as well as their high efficiencies.[32] These efficiencies, 90% compared to the 82% and 84% reported for AWEs and PEMWEs respectively, can be

attributed to the high operating temperatures of *ca*. 650 – 1000 ºC, which result in more favourable thermodynamics and kinetics.[34] AWEs are the most mature technology, and are highly scalable. However, the hydrogen produced by these systems tends to be less pure in comparison to the other electrolyser types and therefore not appropriate for the Haber Bosch process without post processing of the H_2 gas.[35]

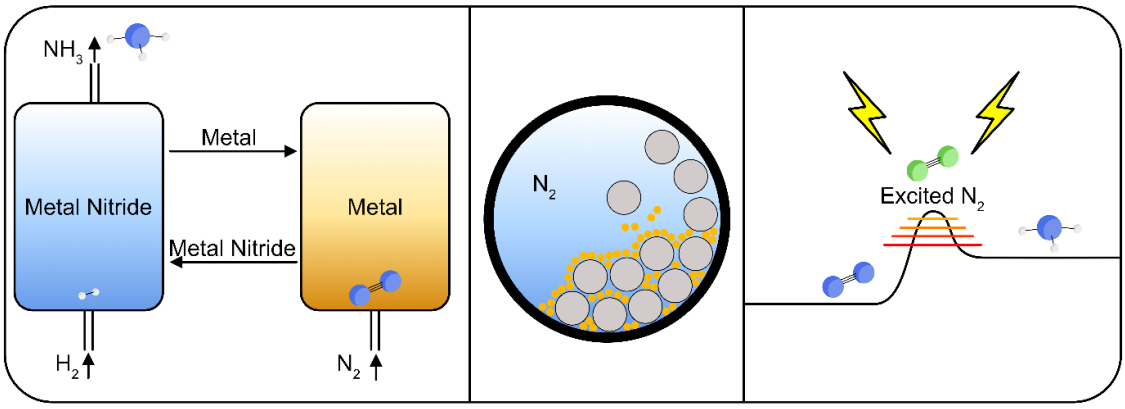

Figure 1.1. Summary of some alternative strategies for ammonia synthesis. From left to right: chemical looping, ball milling mechanochemistry, and plasma-enabled catalysis. There have been many creative attempts at optimising the process of ammonia synthesis, and while they all display fantastic and promising results, a large portion of these methods are still not sustainable in the long term due to the requirement of H_2 gas.

1.1.3 Electrochemical Reduction of N_2

Taking inspiration from nature has always been a cornerstone of Science, having fuelled some of the greatest inventions offered by history. The submarine, sonar and flight were all technologies developed by observing nature, and it stands to reason that sustainable NH_3 synthesis could be aided by mimicking the natural world. It was not until the mid-17th century that the process of nitrogen fixation in plants was discovered. Nitrogen fixation can be done by lightning to convert atmospheric N_2 and O_2 to nitrates which are usable by plants. Otherwise, most natural nitrogen fixation is done by microorganisms known as diazotrophs which contain an enzyme called nitrogenase. The most common form of the nitrogenase enzyme is comprised of two proteins, an Fe protein and a MoFe protein, though there are other versions with FeFe and VFe proteins.[16] The MoFe protein contains a cofactor which is regarded as the active site for nitrogen fixation.[36] Nitrogenase catalyses nitrogen fixation to ammonia by the following equation.[37]

$$N_2 + 8H^+ + 8e^- + 16ATP \rightarrow 2NH_3 + H_2 + 16ADP + 16P_i \quad (1.4)$$

Regarding biological ammonia synthesis, it is extremely important to note that protons and electrons are employed in the hydrogenation of N_2 rather than H_2. Energy is supplied to this reaction via the splitting of adenosine triphosphate (ATP) into adenosine diphosphate (ADP) and inorganic phosphate (P_i, HPO_4^{2-}) releasing *ca.* 29.75 kJ mol^{-1} of energy.[38] This equates to 476 kJ mol^{-1} or 4.93 eV being spent to reduce one molecule of N_2. Furthermore, it should be noted that a quarter of the protons and electrons are directed towards the production of H_2. This high energetic price tag coupled with non-selective production of NH_3 tells us that even nature struggles with the challenge that is nitrogen reduction. Much effort has been put into developing synthetic replacements for nitrogenase, with Mo, V, and Fe serving as the basis for organometallic catalysts.[39] While many have focused on emulating the structure of the enzyme's cofactor, others have taken inspiration from the process, aiming to utilise protons and electrons rather than H_2 directly.

The concept of reducing N_2 directly via protons and electrons has allowed for the field of electrochemical ammonia synthesis to flourish. The electrochemical nitrogen reduction reaction (eN_2RR), as seen in Eq 1.5, is an attractive method for sustainable ammonia synthesis.

$$N_2 + 6H^+ + 6e^- \rightarrow 2NH_3 \quad (1.5)$$

Via this reaction, ammonia can be produced by renewable energy sources under ambient conditions. Homogeneous approaches, while providing a wide range of catalytic performance via ligand modulation, have seen less development due to their associated high costs and low current densities attained.[40] As a result, heterogeneous catalysts have dominated this area of the literature, although eN_2RR still has its own associated challenges, namely the activation of the inert N_2 molecule (BDE of 941 kJ mol^{-1}) as well as the competition with the hydrogen evolution reaction (HER). This competition stems from the fact that HER occurs at less negative applied potentials than eN_2RR, allowing for HER to dominate the surface of the catalyst effectively robbing N_2 of any active sites for reduction. Thus, a large portion of electrons is transferred away from the electrochemical synthesis of ammonia, *i.e.* the faradaic efficiency of eN_2RR is reduced by the competing HER.

The mechanism of eN_2RR can vary from the industrial Haber-Bosch process. As mentioned before, the Haber-Bosch process proceeds via dissociative adsorption of N_2, subsequent hydrogenation of the nitrogen fragments, and desorption of NH_3. The high industrial temperature is responsible for the splitting of N_2, so for reactions at ambient conditions how is N_2 activated onto the surface?

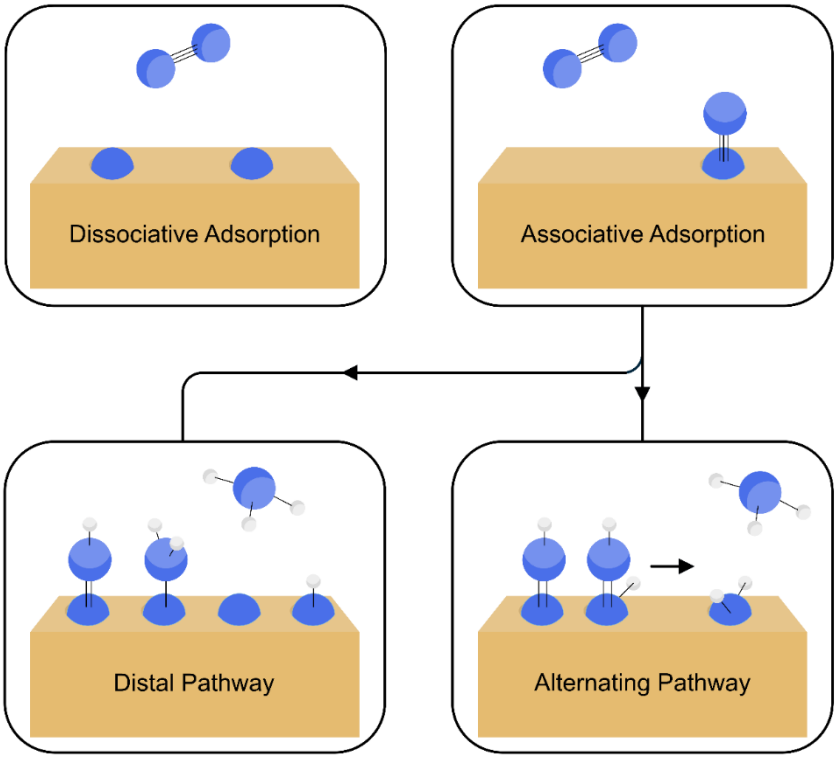

Figure 1.2. Dissociative and associative adsorption of nitrogen, as well as the reaction pathways seen with associative adsorption.

In addition to the dissociate adsorption associated with the Haber Bosch process, eN_2RR can also occur through an associative adsorption mechanism which further leads to two types of reaction pathways, *distal* and *alternating* displayed in Figure 1.2. In the distal path, only one nitrogen atom in the adsorbed N_2 molecule (*N_2, where * denotes an active surface site) is hydrogenated at a time, producing NH_3 before the second *N atom is hydrogenated. On the other hand, the alternating path sees both N atoms hydrogenated in turns, leading to the formation of the reaction intermediates *N_2H_2 and *N_2H_4 before desorption of NH_3 occurs. The operation of either pathway depends on the nature of the catalyst as well as the reaction conditions, although hybrid pathways have been reported in the literature.[41,42] Although the Volmer-Tafel and Volmer-Heyrovsky mechanisms are specific to HER, the

reduction of nitrogen can occur in a similar fashion, wherein the Volmer step is replaced by nitrogen adsorption. For ease of reading, we refer to the two hydrogenation schemes displayed below in Figure 1.3 as Tafel type and Heyrovsky type mechanisms.

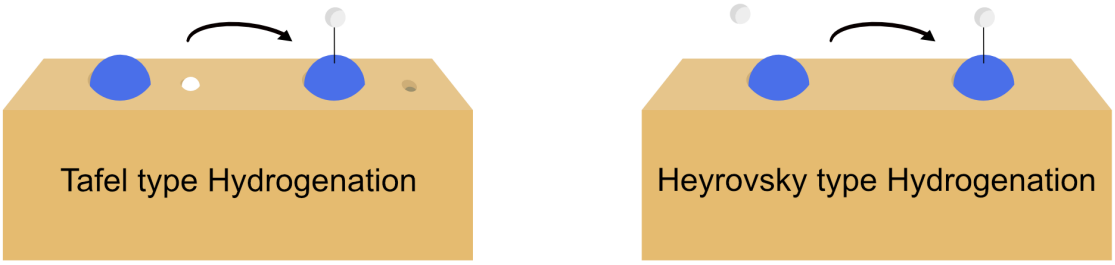

Figure 1.3. Tafel type and Heyrovsky type hydrogenation schemes for the formation of *NH from *N.

Tafel type hydrogenation refers to when H^+ is combined with electrons on the cathode surface to give adsorbed hydrogen (*H) before subsequent hydrogenation with $*NH_x$ to give $*NH_{x+1}$ species, whereas the Heyrovsky type hydrogenation mechanism sees adsorbed nitrogen intermediates directly hydrogenated by protons from the electrolyte and electrons from the electrode. It has been reported that the Tafel type hydrogenation of $*NH_x$ to $*NH_{x+1}$ has activation barriers of *ca.* 1.0 eV for most transition metal surfaces, implying the Tafel type mechanism occurs slowly at ambient conditions.[43]

There also exists a third pathway, specific to the reduction of N_2 on metal nitrides, known as the Mars-van Krevelen (MvK) pathway, summarised in Figure 1.4 below.[44]

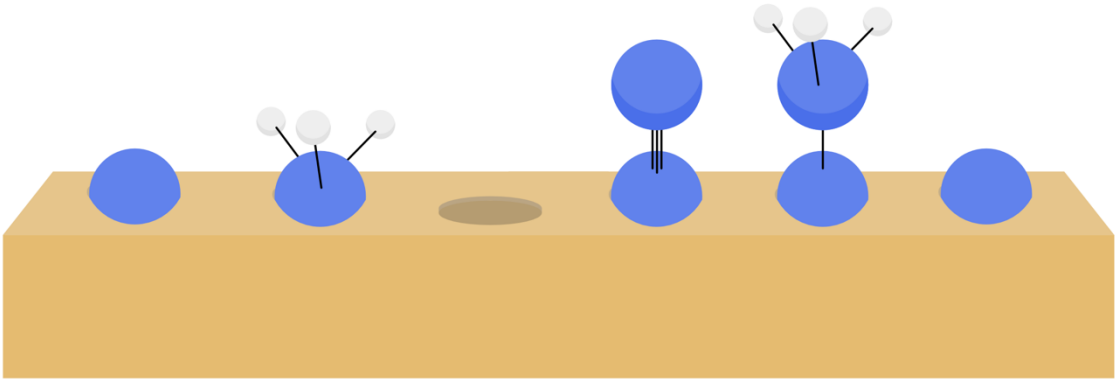

Figure 1.4. Nitrogen reduction to ammonia via the Mars-van Krevelen pathway.

The MvK pathway involves the nitrogen in the metal nitride being reduced to ammonia, which then desorbs from the surface and leaves a vacancy. This vacancy is occupied by N_2,

which undergoes hydrogenation via the distal pathway, resulting in ammonia formation and a new lattice nitrogen. Skúlason *et al*. found via theoretical calculations that the onset potential for the reduction of N_2, on a wide range of transition metal mononitrides, was less negative for the MvK mechanism as opposed to the associative or dissociative pathways.[45] In a further study, Skúlason and co-workers also investigated the regeneration of the vacancy, comparing the occupation of the vacancy by gaseous N_2 with nitrogen atoms that have migrated from the bulk nitride.[46] This study found that for a model vanadium nitride system, regeneration of the vacancy is much more achievable via the migration of bulk nitrogen atoms, implying the eventual decomposition of the VN surface. This is an important factor to consider when studying the MvK mechanism as the stability of the catalyst is of particular importance.

Due the vast space in the literature that is occupied by the eN_2RR, there have been several meta analyses of the field.[47–50] These studies report a troubling consensus in the literature regarding the reproducibility of results for the eN_2RR. It is recommended to validate eN_2RR studies in several ways. For example, employing isotope labelling experiments, *i.e.*, using $^{15}N_2$ as a substrate and observing the amount of $^{15}NH_3$ produced, or repeating the experiment under an argon atmosphere to ensure that no nitrogen contaminants are present to bias the results.[47] The requirements for the eN_2RR to be competitive with the Haber-Bosch process, according to the U.S. Department of Energy are, a rate of 10^{-6} mol s^{-1} cm^{-2}, faradaic and energy efficiencies of 90 and 60%, a current density of 300 mA cm^{-2}, and a rate of catalyst degradation of 0.3% over 1,000 hours.[48,51] Currently, the vast majority of faradaic efficiencies and rates reported in the literature are within 10% and 3×10^{-10} mol s^{-1} cm^{-2}, respectively.[16,47,48,50]

Building on the foundation of eN_2RR, the area of lithium-mediated nitrogen reduction (Li-N_2RR) has seen a recent surge in interest as of 2019, although the area dates back to the seminal work of Tsuneto, Kudo and Sakata.[52] In this work, a faradaic efficiency of 48.7% was reported using a non-aqueous solution of $LiClO_4$ at a high N_2 pressure of 50 atm. It was found that using $NaClO_4$ and Bu_4NClO_4 resulted in negligible amounts of NH_3 implying mediation by Li. Being a relatively novel area of eN_2RR the reaction mechanism is not fully understood. It is tentatively believed that Li^+ ions in solution are reduced to

metallic Li, which forms lithium nitride, Li_3N. This nitride then reacts with protons in solution to form ammonia and Li^+ ions.

Electrolytic effects pertaining to the Li-N_2RR have been extensively investigated by both Chorkendorff *et al*.[53] and Simonov *et al*.[54] in separate works. Both studies report outstanding faradaic efficiencies of *ca*. 100% when introducing lithium via fluorine containing salts, lithium tetrafluoroborate ($LiBF_4$) and lithium bis(trifluoromethylsulfonyl)imide ($LiNTf_2$) respectively. Additionally, these works concluded that the impressive performance of their systems could be related to the solid electrolyte interphase (SEI) layer. Both studies found that their respective fluoride containing SEIs suppressed the undesired degradation of the electrolyte and facilitated the transfer of Li^+. The study performed by Chorkendorff *et al*.[53], which was performed on a porous Cu cathode, also reported an impressive NH_3 production rate of 2.5 μmol s^{-1} cm^{-2} at a current density of –1.0 A cm^{-2}, albeit at a reduced faradaic efficiency of 71%. Simonov *et al*.[54], using a nickel wire, achieved an NH_3 production rate of 0.233 μmol s^{-1} cm^{-2} whilst maintaining high faradaic efficiencies of 99%. While both of these works display promising results for the Li-N_2RR as an alternative to the Haber Bosch process, it should be kept in mind that Li is a critical material as designated by the European Union Critical Materials Act. This has warranted the exploring of alternatives to Li, such as Na, Mg and Ca, however, these candidates pale in comparison to Li as of yet.[55]

To summarise this section, the Haber-Bosch process is an excellent example of a process that satisfies several of the principles of green chemistry yet is unsustainable. It uses a cheap, robust catalyst to allow for increased energy efficiency. However, it uses pure hydrogen gas sourced from the catalytic cracking of methane, a process that releases CO_2. A great many efforts have been made to electrify the process; however, they are currently inefficient or require raw materials that are deemed as politically critical. In short, rapid breakthroughs are needed for the eN_2RR to become competitive with the Haber-Bosch process. It is also important to note that the production of ammonia is only one piece of a larger picture, and that the easing of industrial demand, and the associated emissions, should be explored to the fullest.

1.2 Circular Economy of Nitrogen

The production of ammonia is only one part of the global nitrogen cycle, and while it is important to optimise that process, further stages of the cycle must not be neglected.

1.2.1 Nitrate Reduction

We have determined that even nature, with the aid of nitrogenase, struggles to convert the inert nitrogen to a fixed form. However, this biological fixation was the only feasible route for millions of years. It must be recognised that this, well established, global nitrogen cycle was fundamentally changed by the Haber-Bosch process.[56] It is usually stated that ammonia is used as a fertiliser, when in fact, it is a precursor to a fertiliser. Ammonia is typically converted to ammonium nitrate, NH_4NO_3, or urea, $CO(NH_2)_2$. These two species, when introduced to soil, break down to give ammonium (NH_4^+) and nitrate (NO_3^-) ions, which are then taken up and used by plants. Any excess ions, usually converted into nitrates or nitrites (NO_x species), move downward via the internal drainage of the soil, until they eventually reach the groundwater *i.e.*, water that is found underground, in soil pore spaces and in rock formation fractures. For context, groundwater accounts for 30% of all freshwater on Earth, 40% of all drinking water, and half of the water used in irrigation.[57,58] Additionally, there is ample run-off of these NO_x species into rivers and lakes. Alarmingly, Grizzetti *et al*.[59] found that half of the population of Europe resides in areas where the nitrate concentration of surface water is higher than 25 mg NO_3^- L^{-1}, a concentration higher than the maximum contaminant levels of 10 mg L^{-1} that are recommended by the World Health Organisation.[56] NO_x species are responsible for the disease methemoglobinemia, which involves the oxidation of Fe^{2+} to Fe^{3+} in the blood, damaging the oxygen transporting capability of the red blood cells. Nitrates are also suspected to, when working with other compounds, be carcinogenic.[56]

There is also the impact on the environment to be considered. Nutrient levels in aquatic systems are a limiting factor for the growth of phytoplankton and algae. The sudden removal of a limiting factor, *i.e.*, nutrient fertilisers, resulting in excessive algal growth is referred to as eutrophication. Eutrophication is a disastrous phenomenon for the environment, as the resulting algal blooms will not only disrupt the ecosystem, but more importantly, they will die. The algae will then be decomposed by microorganisms in a

process that consumes the dissolved oxygen in the aquatic environment, eradicating marine life by hypoxia and creating so-called "dead-zones".[60,61] As of 2008, 400 dead zones (affecting a total area of nearly 250,000) were accounted for by Diaz and Rosenberg, who also noted that the number of dead zones were doubling each decade since 1960.[61]

The employment of denitrifying bacteria to convert the nitrates to N_2 gas is a pollution free method that is unfortunately sluggish even in the absence of anthropogenic nitrates. These bacteria demand strict living conditions, meaning these micro-organisms will need to become more tolerant to increased nitrate levels.[60,62] An alternative approach to biological remediation strategies is the employment of electrocatalytic methods. It has been found that the electroreduction of nitrates to harmless nitrogen is a very complex process, with several possible products that may be physically and environmentally damaging, such as NO, NH_4^+, N_2O, and NH_3OH^+. Despite the experimentally observed products being well known, the exact mechanism of nitrate reduction is currently unknown, and still disputed.[63,64]

There is a growing interest in the development of electrocatalysts targeted towards the selective reduction of nitrates to useful ammonia. Nitrates are an already fixed form of nitrogen, with a much smaller BDE of 204 kJ mol^{-1}. As such, it is an ideal substrate for the synthesis of ammonia. Despite the relative novelty of this field, especially compared to the century old Haber-Bosch process, excellent results have been reported in the literature. Sargent *et al*.[65] reported CuNi alloys with a 1:1 ratio that achieved a faradaic efficiency of 99 $\pm$ 1% towards NH_3 synthesis. Compared to a pure Cu electrode, a 6-fold increase in nitrate reduction activity was reported for this alloy system, as well as a reduction of 0.2 V for the overpotential required to achieve this high faradaic efficiency. Another report, by Yu *et al*.[66] achieved a selectivity of nearly 100% towards NH_3 using strained ruthenium nanoclusters at a current density of *ca.* 120 mA cm^{-2}. This study accredited an exceptionally high rate of ammonia formation (5.56 mol g_{cat}^{-1} h^{-1}) to hydrogen radicals. These radicals can attribute their generation to lattice strain which suppresses the coupling of these radicals. Consequently, the radicals can be used to hydrogenate nitrate intermediates to ammonia. It is important to note that this rate of ammonia formation is reported to exceed that of the industrial Haber-Bosch process (*ca*. 200 mmol g_{cat}^{-1} h^{-1}).[66]

Clearly, this area of research has yielded some truly excellent faradaic efficiencies towards NH_3 production. This vast improvement over the field of eN_2RR can be (broadly) attributed to the fact that nitrates are already a fixed form of nitrogen. Nitrate has been reported to have a BDE of *ca.* 204 kJ mol^{-1}, which is substantially lower than the 941 kJ mol^{-1} needed to break the N≡N bond.[11]

1.2.2 Cyanide Reduction

The successful reduction of nitrate serves as an important precedent for the employment of previously fixed forms of nitrogen as a substrate. One of the foci of this thesis is the catalytic electroreduction of cyanide, which is a promising candidate for upcycling. Cyanide is quite a common species in nature, being found in over 2,500 plant species in the form of cyanogenic glycosides, *e.g.*, linamarin, amygdalin, dhurrin, via a process called cyanogenesis. Many of these plants are economically important crops, such as apples, cassava, bamboo, and sorghum which are sometimes treated to remove excessive amounts of cyanide.[67,68]

Cyanogenesis usually serves a defensive purpose, and is triggered by a physical disruption, *i.e.*, cutting of the plant or herbivore attack.[69] When this occurs, the glycoside undergoes action by glycoside hydrolase enzymes to liberate cyanide via hydrolysis of the glycosidic bond. For example, dhurrin is broken down into glucose and p-hydroxymandelonitrile by dhurrinase, which is in turn, converted into cyanide and p-hydroxybenzaldehyde by the enzyme α-hydroxynitrile lyase.[70] This has been performed on the laboratory scale by manually pulverising cyanogenic plant matter and adding water, however this was done in a qualitative sense to demonstrate the presence of cyanide.[71]

Cyanides are also ubiquitous in industry, seeing application in the fields of pharmaceuticals, agriculture, cosmetics, and synthetic rubber, although it is most closely associated with metallurgical processes such as electroplating, jewellery and most famously, mining.[72] Cyanide is used extensively in mining to extract gold in the form of dicyanoaurite. The Elsner equation (Eq. 1.6) describes the leaching of gold via an aerated aqueous solution of sodium cyanide.[73]

$$4Au + 8NaCN + O_2 + 2H_2O \rightleftharpoons 4[NaAu(CN)_2] + 4NaOH \qquad (1.6)$$

Cyanidation is also used in heap leach mining to extract gold from large amounts of low-grade ore. The cyanide solution is sprayed onto large heaps of ore and extracts gold whilst trickling through the ore.[67] Gold can be recovered from the dicyanoaurite solution via several methods, although the most well-known is the Merrill Crowe process, wherein zinc dust is added to solution and gold is precipitated out.[74] The cyanide waste products are referred to as cyanide tailings (CTs). CTs are solid wastes whose composition is dependent on the ore mined, although they can contain several valuable metals such as gold, silver, copper, iron, and zinc. The fate of these CTs is to be deposited in tailings dams. Cyanide tends to exist in the effluent as free cyanide, weak acid dissociable cyanide (CN_{WAD}), or string acid dissociable cyanide (CN_{SAD}).[75] At pH values of around 3 – 5, it is expected that $HCN_{(aq)}$ and CN_{WAD} are converted to $HCN_{(g)}$, although more acidic pH values would be necessary to convert CN_{SAD}.[76]

Should this $HCN_{(g)}$ be collected, (some mining facilities capture HCN for reuse in the cyanidation process via air stripping[77]) and stored in a more useable form, *i.e.*, an alkali salt, it could be readily used as a substrate for NH_3 synthesis. Cyanide was first shown to be reduced to methane and ammonia via nitrogen fixing bacteria *Azotobacter vinelandii* and *Clostridium pasteurianum* by the seminal work of Hardy and Knight.[78] It was found that cyanide reduction can occur in two ways.

$$HCN \rightarrow CH_4 + NH_3 \quad (1.7)$$

$$HCN \rightarrow CH_3NH_2 \quad (1.8)$$

Methylamine was found to be the minor product, with observable amounts equivalent to 10% of the major products, methane, and ammonia. It was also reported that these reductions were inhibited by the presence of carbon monoxide (*ca.* 0.9 atm).

Imitating nature has subsequently, led to studies on nitrogenase metalloenzymes for the catalytic reduction of CN^-. The more recent work of Ribbe *et al*. has shown that in the presence of a strong reductant, namely europium(II) diethylenetriamine pentaacetate [Eu^{II}–DTPA], these metalloenzymes can catalyse the reduction of CN^-, producing NH_3 and both alkanes and alkenes ranging from two to seven carbon atoms in length.[79] Ribbe *et al*. furthered this study via the inclusion of an even stronger reductant, samarium(II) iodide (SmI_2).[80] Nitrogenase cofactors when working in concert with SmI_2 were found to be capable of not only catalytically turning over CN^-, but also CO and CO_2 under ambient

conditions, with TONs of 13–15, 2.7–4.5, and 1.4–2.3 for each substrate, respectively. Moving on from extracted metalloenzyme cofactors, Rittle and Peters developed an Fe-based coordination complex, [SiP$^{iPr}_3$]Fe(CN), capable of producing significant amounts of NH_3 and CH_4 from cyanide (*ca.* < 41%).[81] However, this process required reagents kept at very low temperatures (–78 °C) and is not catalytic.

Electrochemical methods for the reduction of cyanide to methane and ammonia have also been explored. Augustynski *et al*. performed the electrochemical reduction of cyanide over various metallic cathodes under ambient conditions at a pH of 6.[82] Interestingly, in contrast with the studies performed by Hardy and Knight, formation of methylamine was found to be the major product, and methane and ammonia were the minor products. Additionally, Augustynski and co-workers reported Ni as drastically outperforming all other cathode materials, including precious metals like Pd, Pt and Au, with a reported faradaic efficiency of 71.7 %. In fact, the next best cathode was also an earth-abundant metal, Cu, with an associated efficiency of 27.6 %.

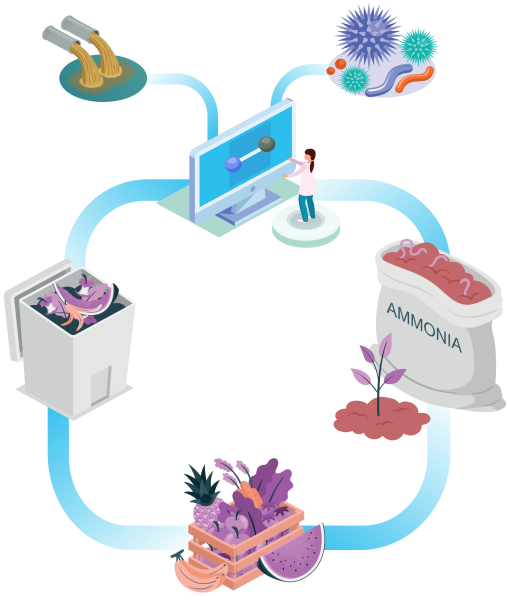

Figure 1.5. Circular economy model applied to cyanide.

These heterogeneous catalytic studies push the reduction of cyanide closer to immediate application. However, despite the benefits of electrochemical cyanide reduction, two valuable chemical feedstocks, a cheap metal catalyst, as well as a fixed nitrogen containing substrate, there is a distinct absence of cyanide reduction in the literature. This can be attributed to the fact that the extraction of cyanide from food and waste effluent has not been perfected, as well as the fact, that in the framework of our current economy, the reduction of cyanide would not replace the Haber-Bosch process, nor the potential offered by electrochemical nitrogen reduction. However, it should be kept in mind that in a circular economy, we should only need to activate nitrogen once, and valorise cyanide waste products as seen in Figure 1.5, as well as other fixed forms of nitrogen back to ammonia.

1.3 Ammonia as an Energy Carrier

Throughout this thesis we have explored the possibility of substituting N_2 with already fixed forms of nitrogen as a substrate for the electrocatalytic synthesis of ammonia. However, the chief limitation of such an approach, when evaluated against the Haber-Bosch process and in the context of the current linear economy, is the availability of reactants when compared to atmospheric nitrogen. Should we transition to a circular economy we may be able to produce a sufficient quantity of NH_3 using the current infrastructure, and recycle it, potentially removing the need to reduce nitrogen in the first place. As of now, the Haber-Bosch process is a necessity. As said previously, it has changed little throughout a century of study and optimisation. The electrochemical reduction of atmospheric nitrogen is seen as a final, long-term solution that will replace the Haber-Bosch process. The looming climate crisis warrants the exploration of any possible substitutive approaches that can be implemented quickly and efficiently. One of the more immediate actions that could be taken is to supplement the Haber-Bosch process with carbon capture technology and use ammonia as a carbon-free energy carrier.

Ammonia is a considered to be a viable candidate for the chemical storage of H_2 due to its high gravimetric hydrogen density (17.8 wt.%), its decomposition to H_2 and benign N_2, and its relative ease of storage.[83–85] For example, the storage of NH_3 over a period of 182 days is much cheaper per energy unit than storing pure H_2 (0.54 vs 14.95 \$/kg–H_2, respectively).[83] Additionally, and not insignificantly, there is pre-existing infrastructure for the handling and transport of massive quantities of liquid ammonia.[86] However, one of the limiting factors regarding the use of NH_3 as a hydrogen energy carrier is the development of cheap and efficient decomposition catalysts that can feasibly perform on-site hydrogen production.

1.3.1 Ammonia Decomposition

Being the reverse reaction of the Haber Bosch process (Eq. 1.1), the decomposition of ammonia is endothermic and favoured at high temperatures and low pressures.

$$2NH_3(g) \rightarrow N_2(g) + 3H_2(g) \quad \Delta H^0_{298\,K} = 92\ kJ\ mol^{-1} \tag{1.9}$$

As such, many studies have been performed at moderate to high temperatures and at atmospheric, or low pressures.[87] The thermal decomposition reaction is thought to proceed via the binding of ammonia onto an active site of the catalytic material, followed by successive NH bond scissions. Upon being completely dehydrogenated, associative desorption of the products, N_2 and H_2, occurs. While the dissociative adsorption of N_2 is known to be the RDS in ammonia synthesis, there is still speculation as to whether the first NH bond scission or the associative desorption of N_2 is rate limiting for ammonia decomposition. Masel *et al.*[88] examined the decomposition reaction on several different transition metal catalysts supported on alumina pellets and found that while some metals (Fe, Co, Ni, Cr and Ru) were limited by the recombination of bound N atoms, others (Pd, Rh, Pt, Ir, and Cu) were limited by the first NH cleavage. Among the investigated metals, Ru is the most active one for NH_3 decomposition.[89] Consequently, the role of the support material has been thoroughly investigated for Ru catalysts, with good activities generally being displayed on carbon nanotubes (CNTs) which are believed to be effective due to their high dispersions of Ru particles as well as their electron conductivity.[90] This latter factor is particularly relevant when the catalyst is paired with a KOH promoter, as it facilitates electron donation from the promoter to the active site of the catalyst.[89,91] In summary, the state of the art catalyst is one comprised of Ru supported on CNTs with a KOH promoter, however MOFs, alkaline amides, and other metal oxides are being employed to support Ru nanoparticles with promising results.[92–95]

Ru is expensive and there is an incentive to develop catalysts that require only earth abundant, and cheap materials. The employment of new techniques enables the feasibility of cheaper transition metal catalysts, despite their natural underperformance relative to Ru. The field of photothermal catalysis is one such technique, wherein photochemical and thermal effects are used in concert. Absorption of a photon can lead to several different effects, depending on the material in question. For example, in a semiconductor, should the photon be equal or higher in energy than the gap between the conduction and valence bands, then an electron hole pair is generated. These charge carries can then be taken up by adsorbates to initiate or facilitate chemical processes. On metallic nanoparticles, the absorption of light can result in the localised surface plasmon resonance (LSPR) of conducting electrons.

This phenomenon is commonly described in terms of the Drude model, wherein the conductivity of a metal is likened to that of an electron gas moving in an ionic lattice.[96] LSPR occurs when incident light (or some other electromagnetic wave) causes the polarisation of the nanoparticle, accumulating opposite charges at either end of the structure. Due to this charge separation, a restoring force acts upon the electron cloud. The combination of the incident light and the restoring Coulombic force results in the oscillation of the electron cloud.[96] When the incident electromagnetic wave and the resonant frequency of the electron cloud are in phase, the electric field is maximised in certain "hot spots" of the nanoparticle. The decay of the energy associated with LSPR can occur via a radiative (involving fluorescence) or non-radiative pathway.

Non-radiative decay can occur via the excitation of an electron-hole pair, or by electron-electron collisions, which may generate local heating.[97] The photogenerated electron and hole, or charge carriers, can be referred to as "hot" carriers if their energies are larger than what the thermal distribution of electrons at ambient temperature would allow, *i.e.*, occupying states normally not allowed by the Fermi-Dirac distribution.[98]

Despite the formation of these hot carriers and generation of strong heating via light, there are few photothermal studies focused on the catalytic decomposition of ammonia. Halas *et al.*[99] reported, on an alloy consisting of a Cu nanoparticle antenna with Ru reactor sites, a reduction in the activation energy, E_a, from 1.21 eV to 0.35 eV upon illumination. It was found that this decrease is due to hot carriers exciting bound N atoms, facilitating the associative desorption of N_2. Halas and co-workers expanded on this work and replaced Ru in their catalyst with Fe.[100] This catalyst displayed an impressive improvement in turn over frequency (TOF), increasing from 0.00017 s^{-1} to 1.7 s^{-1} when illuminated. The surface temperature was reported to be 625 K for both systems, implying a photochemical effect. Theoretical calculations based on embedded correlated wavefunction methods were carried out to investigate the activation barriers for N–H bond scission and the associative desorption of N_2. In both cases, the ground state barrier was larger in comparison to the excited state, with a reduction in energy from 1.20 eV to 0.53 eV and from 2.67 eV to 0.50 eV for the scission and desorption steps respectively.

Should NH_3 decomposition be made feasible, and a change to a nitrogen economy occur, the ammonia synthesis industry would have to increase to around five times its current size

to meet the demand.[84] Additionally, pursuing a nitrogen economy is heavily dependent on the sustainable production of H_2, ideally from renewable energy sources via water splitting. However, should this not be feasible, the widespread usage of blue hydrogen via carbon capture technology would have to be implemented.

Chapter 2 Computational Theory

2.1 Schrödinger Equation and Quantum Mechanics

The advent of the 20th century was the domain of classical mechanics, which appeared to be able to explain most phenomena. Maxwell's equations had synchronised the fields of electromagnetism and optics. August Kekulé had put the controversial matter of the structure of benzene to rest. The Periodic Table had been shown by Dmitri Mendeleev to have logical trends. The field of thermodynamics was developed by Josiah Gibbs, which incidentally, remains practically unchanged to this day. It appeared as if all of the fundamental discoveries of science had been made, bar a few small details. However, as is usually the case, these small details were proven to have the greatest effect on science. The matter of explaining blackbody radiation, the photoelectric effect, as well as the work of de Broglie unveiled the field of quantum mechanics.

2.1.1 Schrödinger Equation

One of the quintessential concepts of quantum mechanics is that of the wavefunction. For any chemical system there is a wavefunction, that when acted upon by an appropriate operator, returns the observable properties of the system. For example,

$$H\psi = E\psi \tag{2.1}$$

H, the Hamiltonian operator acts upon the wavefunction of a chemical system, ψ, also known as the eigenfunction, to give the energy of the system, E, an eigenvalue. This particular equation is referred to as the time independent Schrödinger equation, and is usually written in a more expansive way, where the Hamiltonian is only slightly expanded upon.

$$\left\{-\frac{\hbar}{2m}\nabla^2 + V\right\}\psi = E\psi \tag{2.2}$$

When written in this form, the Hamiltonian operator has been expanded to be the sum of two terms, the kinetic and potential energies, respectively. This is still a very vague description of the system. Further expanding the Hamiltonian operator provides us with five contributions to the total energy.

$$H = -\sum_{i=1}^{N} \frac{\hbar^2}{2m_e} \nabla_e^2 - \sum_{A=1}^{M} \frac{\hbar^2}{2m_A} \nabla_A^2 - \sum_{i=1}^{N} \sum_{A=1}^{M} \frac{e^2 Z_A}{r_{iA}} + \sum_{i}^{N} \sum_{j>1}^{N} \frac{e^2}{r_{ij}} + \sum_{A=1}^{M} \sum_{B>1}^{M} \frac{e^2 Z_A Z_B}{r_{AB}} \quad (2.3)$$

Where i and j run over electrons, A and B run over nuclei, e is the charge of the electron, m_e and m_A are the masses of the electrons and nucleus A, respectively, Z is the atomic number, $\hbar$ is Planck's constant divided by 2π, and r_{ab} is the distance between particles a and b. Additionally, ∇^2 is the Laplacian operator, which, in cartesian coordinates, has the form,

$$\nabla_q^2 = \frac{\partial^2}{\partial x_q^2} + \frac{\partial^2}{\partial y_q^2} + \frac{\partial^2}{\partial z_q^2} \quad (2.4)$$

We can "tidy up" the Hamiltonian, by moving to atomic units, thereby reducing our constants to 1.

$$H = -\frac{1}{2} \sum_{i=1}^{N} \nabla_i^2 - \frac{1}{2} \sum_{A=1}^{M} \frac{1}{M_A} \nabla_A^2 - \sum_{i=1}^{N} \sum_{A=1}^{M} \frac{Z_A}{r_{iA}} + \sum_{i=1}^{N} \sum_{j>1}^{N} \frac{1}{r_{ij}} + \sum_{A=1}^{M} \sum_{B>1}^{M} \frac{Z_A Z_B}{r_{AB}} \quad (2.5)$$

The first two terms describe the kinetic energies of the electrons and nuclei, respectively. The latter three terms are potential energy terms and correspond to, in order, electron-nuclei, electron-electron and nuclei-nuclei interactions.

2.1.2 Born Oppenheimer Approximation

The Born-Oppenheimer is one of the most common approximations to make in computational chemistry. The nuclei in a chemical system are so much larger, and consequently, move much more slowly than the electrons. For the sake of practicality, we decouple nuclei and electrons in our calculations, computing electronic energies for nuclear positions that are fixed. This leads us to the electronic Hamiltonian operator, H_e.

$$H_e = -\frac{1}{2} \sum_{i=1}^{N} \nabla_i^2 - \sum_{i=1}^{N} \sum_{A=1}^{M} \frac{Z_A}{r_{iA}} + \sum_{i=1}^{N} \sum_{j>1}^{N} \frac{1}{r_{ij}} \quad (2.6)$$

We have removed the kinetic energy contribution of the nuclei entirely. The nuclear-nuclear interactions do still provide a meaningful contribution to the energy, but they are a constant value and need only be calculated once per atomic configuration. Applying this electronic Hamiltonian gives us our electronic Schrödinger equation,

electronic wavefunction, ψ_e, and corresponding electronic energy, E_e, which are all dependent on the electronic and nuclear coordinates. Subsequently, the total energy for a particular configuration can be calculated by adding the nuclear-nuclear interaction term to the electronic energy.

2.1.3 Variational Principle

So far, we have only discussed the application of the Hamiltonian operator to the wavefunction, but how do we acquire the wavefunction in the first place? And even if we do have a wavefunction, how do we ensure that it is the wavefunction of the ground state of our system? In this case, we can apply the variational principle. Assuming that we have an arbitrary real wavefunction, ψ_i, we can write our Schrödinger equation as the expectation value below.

$$E_i = \frac{\int \psi_i H \psi_i \partial r}{\int \psi_i \psi_i \partial r} \tag{2.7}$$

It should be stated at this point that our wavefunctions satisfy the orthonormality condition,

$$\int \psi_i \psi_j \, dr = \langle \psi_i | \psi_j \rangle = \delta_{ij} \tag{2.8}$$

Where the Kronecker delta, δ_{ij}, is equal to 1 if i and j are equal, and 0 otherwise. Subsequently, the denominator in Eq. 2.7 can be reduced to unity. Of the possible eigenvalues, we know that the ground state, E_0, serves as a *lower bound* to the eigenvalues, and consequently, the eigenfunctions.

$$E_0 \leq \int \psi_i H \psi_i dr \tag{2.9}$$

When looking for wavefunctions to describe the ground state, we can look at the associated energies and follow the simple rule of, the lower the energy, the closer we are to the ground state. The implications of this principle cannot be understated. This has turned the determination of ground state energies into an optimisation problem.

2.1.4 Hartree Fock Theory

The Schrödinger equation cannot be solved exactly for any system with more than one electron. We can solve the equation exactly for one electron systems, (H, He^+, Li^{2+},…), but

as soon as a second electron is involved, we run into the three-body problem and the solution to the Schrödinger equation is not tractable. Another complication that must be kept in mind is that the spin of the electron must be accounted for. So far, we have only been discussing orbitals with 3 spatial (x, y, z) coordinates. We know that each orbital can contain two electrons that are spin paired. These antiparallel spins allow us to separate the wavefunctions to describe two electrons occupying the same spatial orbital, with different spins, which we define as α and b. We say that these two electrons are occupying different spin orbitals, χ_i, as described below in Eq. 2.10.

$$\psi_i \longrightarrow \begin{matrix} \psi_i(x)\alpha \\ \psi_i(x)\beta \end{matrix} \rightarrow \begin{matrix} \chi_a \\ \chi_b \end{matrix} \tag{2.10}$$

As solving the polyelectronic wavefunction is impossible, an important simplification is made. We devise a one electron Hamiltonian operator, $h(i)$, for which electron-electron interactions are neglected.

$$H = \sum_{i}^{N} h(i) \tag{2.11}$$

Where the one electron Hamiltonian, $h(i)$, is defined as

$$h(i) = -\frac{1}{2}\nabla_i^2 - \sum_{A}^{M} \frac{Z_A}{r_{iA}} \tag{2.12}$$

This operator is dependent upon the kinetic energy of one electron as well as the nuclear attraction term. This is a solvable expression and satisfies the following relation.

$$h(i)\chi_j(x_i) = \varepsilon_j \chi_j(x_i) \tag{2.13}$$

Where an electron, x_i, occupies a spin orbital, χ_j, with an energy, ε_j. As the Hamiltonian expressed in Eq. 2.11 is separable, we can express its many electron eigenfunctions as products of one electron wavefunctions, known as the Hartree product, which is given by,

$$\Psi^{HP} = \chi_i(x_1)\chi_j(x_2)\chi_k(x_3) \ldots \chi_n(x_N) \tag{2.14}$$

Subsequently, the energy of the Hartree product can be calculated as the sum of eigenvalues, or orbital energies, obtained in Eq 2.13.

$$\langle \Psi | H | \Psi \rangle = \varepsilon_i + \varepsilon_j + \varepsilon_k + \cdots + \varepsilon_n = E \tag{2.15}$$

This however does not take into account any electron-electron interactions. As such, Hartree employed the Born interpretation of the wavefunction, introducing an electronic potential to the one electron operator, $h(i)$.

$$\left(-\frac{1}{2}\nabla_i^2 - \sum_A^M \frac{Z}{r_{iA}} + \sum_{i\neq j}^N \int \left[\frac{|\chi_j(x_j)|^2}{r_{ij}}\right] \partial x\right)\chi_i(x_i) = \varepsilon_i \chi_i(x_i) \qquad (2.16)$$

Essentially, the electron occupying spin orbital i, interacts with the point charges of the nuclei, and the charge density of the electron occupying spin orbital j. To solve Eq. 2.16, one must supply trial functions for χ_i and χ_j, calculate the charge density and energy, yielding a new set of spin orbitals. This process is repeated until there is little difference between the input and output spin orbitals. This method is referred to as the Self-Consistent Field (SCF) method.

This wavefunction however, fails to satisfy the antisymmetry principle, which states that for a fermionic wavefunction (a wavefunction describing electrons) exchanging the coordinates of two electrons must result in the wavefunction changing sign, *i.e.*, the wavefunction must be antisymmetric. This was remedied by the work of John C. Slater, who opted to write the wavefunction as a linear combination of spin orbitals in the form of a determinant.

$$\Psi = \frac{1}{\sqrt{2}}\left[\chi_i(x_1)\chi_j(x_2) - \chi_i(x_2)\chi_j(x_i)\right] = \frac{1}{\sqrt{2}}\begin{vmatrix}\chi_i x_1 & \chi_j x_1 \\ \chi_i x_2 & \chi_j x_2\end{vmatrix} \qquad (2.17)$$

This is a simple Slater determinant for a 2-electron system. By virtue of being a determinant, exchanging electronic coordinates results in the appropriate changing of the sign of the wavefunction. Additionally, doubly occupying an orbital with two electrons results in the determinant being equal to zero. In short, the antisymmetry principle is satisfied. For a polyelectronic system of N electrons the Slater determinant is written as,

$$\Psi = \frac{1}{\sqrt{N!}}\left|\chi_i(x_1)\chi_j(x_2)\ldots\chi_n(x_N)\right| = \frac{1}{\sqrt{N!}}\begin{vmatrix}\chi_i(x_1) & \chi_j(x_1) & \cdots & \chi_N(x_1) \\ \chi_i(x_2) & \chi_j(x_2) & \cdots & \chi_N(x_2) \\ \vdots & \vdots & \ddots & \vdots \\ \chi_i(x_N) & \chi_j(x_N) & \cdots & \chi_N(x_N)\end{vmatrix} \qquad (2.18)$$

The Slater determinant is a determinant containing all N electrons in all N spin orbitals, with a normalisation factor ensuring that the probability density is 1 in all space. The

extension of the Hartree method to incorporate the Slater determinant was done by Fock and allows for the calculation of the energy to be done using three terms.

The first term is the core Hamiltonian and represents the kinetic energy of an electron, x_1, in a spin orbital, χ_i, as well as its interaction with M nuclei. This term is expanded below in Eq. 2.19.

$$H_{ii}^{core} = \int \chi_i(x_1)\left(-\frac{1}{2}\nabla_i^2 - \sum_{A=1}^{M}\frac{Z_A}{r_{iA}}\right)\chi_i(x_1)dr_1 \tag{2.19}$$

The Coulombic interaction between electron pairs is written as J_{ij}, the Coulomb integral.

$$J_{ij} = \int\int \chi_i^*(x_1)\chi_j^*(x_2)\frac{1}{r_{ij}}\chi_i(x_1)\chi_j(x_2)\partial r_1 \partial r_2 \tag{2.20}$$

We also have the exchange interaction, written as K_{ij}, the exchange integral.

$$K_{ij} = \int\int \chi_i^*(x_1)\chi_j^*(x_2)\frac{1}{r_{ij}}\chi_i(x_2)\chi_j(x_1)\,\partial r_1 \partial r_2 \tag{2.21}$$

The H_{ii}^{core} term provides a favourable energy contribution, whilst the repulsive Coulomb integral provides an unfavourable energy to the system. The exchange integral can be thought of as a correction to the Coulomb integral and is considered a manifestation of the Pauli exclusion principle. Two electrons of the same spin cannot occupy the same space and will avoid each other, consequently lowering their Coulombic interaction. Summing these forces for a polyelectronic system yields the total energy of a system (for the set of trial spin orbitals used). For simplicity, we consider a polyelectronic, closed shell system defined by all orbitals containing two electrons of the opposite spin. Consequently, we can separate the spin orbitals into spin and spatial components, allowing us to sum over the $N/2$ spatial orbitals, ψ_i, making computation much simpler.

$$E = 2\sum_{i=1}^{\frac{N}{2}} H_{ii}^{core} + \sum_{i=1}^{\frac{N}{2}}\sum_{j=1}^{\frac{N}{2}}\left(4J_{ij} - 2K_{ij}\right) + \sum_{i=1}^{\frac{N}{2}} J_{ii} \tag{2.22}$$

The first term, the core Hamiltonian, encapsulates the kinetic energy and the electron-nuclear interaction, and will have to be doubled to represent the electrons of different spins. The electron-electron terms are between the electrons occupying the two spatial orbitals,

ψ_i and ψ_j, meaning there is a total of four electrons, two α and two β electrons. Consequently, there are four Coulombic interactions between the two different spatial orbitals. However, an additional Coulombic term is warranted, representing the interaction between electrons in the same spatial orbital. The exchange term, K_{ij}, in this instance, corrects the Coulombic interactions between orbitals. As electrons of the same spin cannot occupy the same space, they tend to avoid each other, which leads to a reduction of the Coulombic repulsion terms. As such, for spatial orbitals ψ_i and ψ_j, there are only two exchange interactions between electrons of the same spin.

Unfortunately, Hartree-Fock (HF) is not without problems, namely the lack of correlation between electrons. This is a consequence of treating the electron-electron interactions in an averaged way. Instantaneous correlations should show us that the negatively charged electrons avoid each other, and therefore be further away than the electron density suggests. This is the issue of electron correlation, and many quantum chemical methods have been developed to account for correlation.

2.2 Density Functional Theory

The myriad wavefunction based quantum mechanical methods that are extensions of Hartree-Fock are dependent upon $3N$ variables, where N is the number of electrons in the system. Modelling a system that scales as such, can get very expensive, very quickly. Additionally, the wavefunction itself has no physical meaning, unlike the square of the wavefunction, the electron density. The electron density is independent of the number of electrons in the system, and as such, only requires 3 variables and is the probability of finding an electron in a certain volume. For a system of N electrons, the density is written as,

$$\rho(r) = \sum_{i=1}^{N} \psi_i^*(r)\,\psi_i(r) \tag{2.23}$$

Integrating the electron density provides us with the total number of electrons. The electron density should also have maxima at the positions of the nuclei. At these points the gradient of the electron density has a discontinuity, a cusp, as r_{iA} becomes zero. Additionally, the cusp is able to reveal information about the charge of the nuclei.[101] To summarize, the

electron density provides the total number of electrons, the nuclear positions, and the nuclear charge, all the ingredients necessary for the calculation of molecular properties. It is this idea that has motivated the field of density functional theory (DFT).

2.2.1 Precursor to DFT, Thomas, Fermi and Dirac

Attempts to use the electron density are almost as old as quantum chemistry itself, dating back to 1927, with the work of Thomas and Fermi. The Thomas-Fermi model takes into account only the kinetic energy, while treating the nuclear-electron and electron-electron contributions classically. The expression for the kinetic energy in the Thomas-Fermi model is based on a uniform electron gas, a fictitious model of constant electron density.

$$T_{TF}[\rho(r)] = \frac{3}{10}(3\pi^2)^{2/3}\int \rho^{5/3}(r)dr \tag{2.24}$$

This kinetic energy can be combined with classical expressions for the nuclear-electron and electron-electron interactions to give the total energy for an atom.

$$E_{TF}[\rho(r)] = \frac{3}{10}(3\pi^2)^{2/3}\int \rho^{5/3}(r)dr - \sum_{A}^{M}\frac{Z_A}{r_A} + \frac{1}{2}\int\int \frac{\rho(r)\rho(r')}{|r-r'|}drdr' \tag{2.25}$$

While this expression for the energy of an atom is unfeasible due to the kinetic energy approximation as well as the fact that exchange and correlation is neglected, it is noteworthy because it describes the energy only in terms of electron density $\rho(r)$. There is no reference to the wavefunction at all.

This work was built upon by Dirac, who developed an expression for the exchange energy based on the Thomas-Fermi model.

$$E_X[\rho(r)] = -\frac{3}{4}\left(\frac{3}{\pi}\right)^{1/3}\int \rho(r)^{4/3}\,dr \tag{2.26}$$

The addition of this term led to the creation of the Thomas-Fermi-Dirac model (TFD-DFT). While it includes kinetic and classical contributions, and also accounts for the exchange, it is still not very accurate.

2.2.2 Modern DFT

Modern DFT as we know it is built upon two theorems developed by Hohenberg and Kohn. The first theorem, proven by *reductio ad absurdum*, states that the ground state energy is

determined by the ground state electron density. This electron density dictates the external potential, the nuclei charges and positions, which informs the Hamiltonian, which in turn is used to calculate the energy.[102] In other words, the ground state is a unique functional, a function of a function, of the ground state electron density. The second theorem provides a means to predict the electron density of a system by showing, as with purely wavefunction based methods, a variational principle applies to the electron density. Whatever energy we calculate must be greater than or equal to the ground state energy. These two theorems allow us to construct electronic structure calculations based on the electron density as opposed to the wavefunction. The total energy is written as a functional of the electron density and can be written as follows.

$$E[p(r)] = F[\rho(r)] + \int \rho(r) V_{ext}(r) dr \tag{2.27}$$

The latter term is the external potential due to the interaction of the nuclei with the electron density. The first term, however, is the Hohenberg-Kohn *universal functional*, $F[\rho(r)]$. This functional contains the contributions to the kinetic energy and electron-electron interactions. The total energy can also be written explicitly to better represent this.

$$E[\rho(r)] = T[\rho(r)] + E_{ee}[\rho(r)] + E_{Ne}[\rho(r)] \tag{2.28}$$

Where T is the kinetic energy, E_{ee} is the electron-electron interactions and E_{Ne} is the nuclear-electron interactions. If we knew the universal functional then we would be able to describe the system perfectly and get the exact ground state energy. We know this functional exists, but we do not know how to find it. This is one of the principal problems with DFT, there is no clear paradigm to its improvement. We can though, calculate approximate answers using approximate functionals.

Prior attempts at electronic structure calculations via the electron density, i.e., TFD-DFT, were sorely lacking, predicting the energies of molecules to be less stable than their atomic components. The main issue with TFD-DFT is the description of the kinetic energy (Eq. 2.24), based upon fermionic statistics. In 1965, nearly 40 years after TFD-DFT, Kohn and Sham (KS) developed the framework for modern DFT. They applied the Hohenberg and Kohn theorems to a system of non-interacting electrons, as in TFD-DFT, but stated that this system had the same ground state density as a fully interacting system of electrons.[103]

$$\rho_s(r) = \sum_i |\chi_{KS}(r)|^2 = \rho_{exact}(r) \tag{2.28}$$

Where $\rho_s(r)$ is the density of a system of non-interacting electrons, and $\rho_{exact}(r)$ is the density of the interacting system of electrons. The KS method involves splitting the kinetic energy into two terms, the energy associated with non-interacting electrons, T_s, and a correction, T_c, due to electron-electron interactions.

$$T[\rho(r)] \longrightarrow T_s[\rho(r)] + T_c[\rho(r)] \tag{2.29}$$

The kinetic energy of non-interacting electrons can be calculated the same way as in the Hartree-Fock method.

$$T_s[\rho(r)] = -\frac{1}{2}\sum_i \langle\chi|\nabla^2|\chi\rangle \tag{2.30}$$

It is commonly said that DFT is purely based on the electron density, but in fact Kohn Sham DFT (KS-DFT) relies upon a kinetic energy term calculated using the wavefunction.

The electron-electron interactions can also be written analogously to Hartree-Fock theory.

$$E_{ee}[\rho(r)] = \frac{1}{2}\int \frac{\rho(r)\rho(r')}{|r-r'|} dr dr' + E_{NC}[\rho(r)] \tag{2.31}$$

The first term in this equation is usually referred to as $J[\rho(r)]$, the classical Coulombic interaction between electrons. E_{NC} refers to the non-classical part of the electron-electron interaction, containing electron exchange and correlation. The Hohenberg-Kohn universal functional can thus be written as,

$$F[\rho(r)] = T_s[\rho(r)] + J[\rho(r)] + E_{XC}[\rho(r)] \tag{2.32}$$

The remaining non-classical electron-electron interaction is contained in the *exchange-correlation*, $E_{XC}[\rho(r)]$, term, defined below.

$$\begin{aligned} E_{XC}[\rho(r)] &= (T[\rho(r)] - T_s[\rho(r)]) + (E_{ee}[\rho(r)] - J[\rho(r)]) \\ &= T_c[\rho(r)] + E_{NC}[\rho(r)] \end{aligned} \tag{2.33}$$

Where T_c refers to the difference between the kinetic energy of a system of non-interacting electrons and the true kinetic energy. Both exchange and correlation are conveniently contained in one term, that is to say there is no separation between the two effects, unlike in wavefunction based methods. We can now write the total energy as,

$$E[\rho(r)] = T_S[\chi_i] + J[\rho(r)] + E_{XC}[\rho(r)] + E_{Ne}[\rho(r)] \tag{2.34}$$

Which, in terms of orbitals, can be expanded as,

$$= -\frac{1}{2}\sum_{i}^{N}\langle\chi_i|\nabla^2|\chi_i\rangle + \frac{1}{2}\sum_{i}^{N}\sum_{j}^{N}\int\int|\chi_i|^2\frac{1}{r_{ij}}|\chi_j|^2\,dr_i dr_j + E_{XC}[\rho(r)] - \sum_{i}^{N}\int\sum_{A}^{M}\frac{Z_A}{r_{iA}}|\chi_i|^2 dr_i \tag{2.35}$$

A variational principle can be applied to this equation, warranting an SCF approach, wherein we first apply a set of trial orbitals and then minimise the calculated energy under the constraint that the orbitals are orthonormal. We can reduce the previous expression to a set of single particle equations.

$$\left(-\frac{1}{2}\nabla^2 + \left[\int\frac{\rho(r)}{r_{ij}}dr_j + V_{XC}(r) - \sum_{A}^{M}\frac{Z_A}{r_{iA}}\right]\right)\chi_i = \varepsilon_i\chi_i$$

$$\left(-\frac{1}{2}\nabla^2 + V_{eff}(r)\right)\chi_i = \varepsilon_i\chi_i \tag{2.36}$$

In the one electron Kohn-Sham operator, an external potential acts upon the wavefunction, the eigenfunction, to produce an eigenvalue, the energy of the system. As in Hartree-Fock, this potential is determined by the orbitals, which we are aiming to calculate, warranting an iterative SCF procedure.

It is crucial to realise that, in DFT, both the exchange and correlation are captured in one term, as opposed to HF. DFT in principle, is exact. Should we know the exchange-correlation functional, we would be able to calculate the ground state energy of a system exactly. Unfortunately, this is not the case, and many efforts have been made to develop an expression for the exchange-correlation term. The goal of method development in modern DFT is to find better and better approximations to this functional.

2.2.3 Local Density Approximation (LDA)

The goal of method development in modern DFT is to find better and better approximations to the exchange-correlation functional, E_{XC}. As we do not know this quantity, we need to approximate it with a feasible expression. A very common approach is to separate the exchange and correlation terms.

$$E_{XC} = E_X[\rho] + E_C[\rho] = \int \varepsilon_x[\rho(r)]\rho(r)dr + \int \varepsilon_c[\rho(r)]\rho(r)dr \tag{2.37}$$

Where ε is the energy density. The potential used previously in Eq. 2.36 is written as the differential with respect to the density.

$$V_{XC} = \frac{\partial E_{XC}[\rho]}{\partial \rho(r)} = \varepsilon_{xc}[\rho(r)] + \rho(r)\frac{\partial \varepsilon_{xc}[\rho(r)]}{\partial \rho} \tag{2.38}$$

At this stage we must address the matter of *spin polarisation*, where the electron density is written as a sum of α and β spin densities.

$$\rho(r) = \rho_\alpha(r) + \rho_\beta(r) \tag{2.39}$$

The degree of spin polarisation is given as,

$$\zeta = \frac{\rho_\alpha(r) - \rho_\beta(r)}{\rho(r)} \tag{2.40}$$

Where $\zeta = 0$ defines a diamagnetic system with equal α and β spin densities. Also important at this stage is to define the radius of the effective volume containing one electron, r_s, also known as the Wigner-Seitz radius.

$$r_s^3 = \frac{3}{4\pi\big(\rho(r)\big)} \tag{2.41}$$

With all this defined, we are ready to tackle the simplest approximation, the Local Density Approximation (LDA). For closed-shell systems, we refer to the LDA and for open-shell (spin polarised) systems, we refer to the local spin density approach (LSDA). In both schemes, the exchange, ε_X, depends only on the local density, $\rho(r)$. For LDA, the exchange of a uniform electron gas is given by the following expression,

$$\varepsilon_X^{LDA} = -\frac{3}{4}\left(\frac{3}{\pi}\right)^{1/3}\big(\rho(r)\big)^{4/3} \tag{2.42}$$

For LSDA, the spin polarised exchange energy can be written as,

$$\varepsilon_X^{LSDA}\big[\rho_\alpha(r), \rho_\beta(r)\big] = -\frac{1}{2}\left(\frac{3}{4}\left(\frac{3}{\pi}\right)^{1/3}\left(\big(\rho(r)\big)^{1/3}\left[(1+\zeta)^{4/3} + (1-\zeta)^{4/3}\right]\right)\right) \tag{2.43}$$

Regarding the correlation energy, there is no analytic derivation of this functional for even the uniform electron gas. Numerical solutions have been developed however, firstly by Ceperley and Alder, who used quantum Monte Carlo simulations to compute the total energy of several uniform electron gases of different density.[104] Subtracting the analytical exchange energy led to determining the correlation energy. These results were then fitted to local density functionals by Vosko, Wilk and Nusair.[105]

2.2.4 Generalised Gradient Approximation (GGA)

How does one improve upon the LDA approach? In a real system the electron density is not homogeneous. Consequently, LDA, which assumes a spatially uniform electron density, would contain some limitations. The obvious step is to expand the exchange-correlation. Cramer expands on this in a very concise manner, saying that the exchange-correlation functional should "*depend not only on the local value of the density, but on the extent to which the density is locally changing*".[106] In other words, the gradient of the density. These methods are extensions to the LDA approach, and so functionals that include the gradient of the density are 'gradient corrected'. The inclusion of this correction defines the generalised gradient approximation (GGA).

Two branches of GGA functionals exist. The first group can almost be considered semi-empirical, as the exchange-correlation term contains several parameters that have been fitted to experimental thermochemical data or energetics obtained from more accurate, post Hartree-Fock methods. For example, one of the first GGA functionals, B88, developed by Becke, is essentially a correction to the LDA energy that is dependent upon a parameter, which is itself determined by fitting to known data for the noble gases using a dimensionless variable.[106] The latter branch of GGA functional are purely physics based and have no adjustable parameters. One of the leaders in this area is undoubtedly Perdew, who has developed the PW91 functional, which was the *de facto* functional used in solid state studies, until its replacement by the PBE (Perdew-Burke-Ernzerhof) exchange-correlation functional in 1996.[107]

The exchange part of the functional is simply written as an extension to LDA, whereby the LDA exchange contribution is multiplied by a factor dependent on a dimensionless gradient variable, x, as seen in Eq. 2.44

$$\varepsilon_x^{PBE} = \varepsilon_x^{LDA} F(x)$$

$$F(x) = 1 + a - \frac{a}{1 + bx^2} \tag{2.44}$$

The correlation part is similarly an extension onto LDA, although t is used to represent the dimensionless gradient variable.

$$\varepsilon_c^{PBE} = \varepsilon_c^{LDA} + H(t)$$

$$H(t) = c f_3^3 ln\left[1 + dt^2\left(\frac{1 + At^2}{1 + At^2 + A^2 t^4}\right)\right]$$

$$A = d\left[exp\left(-\frac{\varepsilon_c^{LDA}}{c f_3^3}\right) - 1\right]^{-1} \tag{2.45}$$

$$f_3(\zeta) = \frac{1}{2}\left[(1 + \zeta)^{2/3} + (1 - \zeta)^{2/3}\right]$$

$$t = \left[2(3\pi^3)^{1/3} f_3\right]^{-1} x$$

The parameters, *a*, *b*, *c*, and *d* in the exchange and correlation terms have not been fitted to experimental data, rather they are derived constants.[106] Consequently, this functional remains very popular and sees frequent use in solid state calculations nearly 30 years later, and also near the end of this thesis.[108]

2.2.5 Bayesian Error Estimation Functional

A much more recent functional sees extensive use in this thesis, and so I must explore it in detail. This is the Bayesian error estimation functional with van der Waals correlation (BEEF-vdW), developed in 2012.[109] The development of BEEF-vdW was motivated in part by the risk of overfitting the exchange-correlation functional to experimental or high level theoretical data. However, to discuss BEEF-vdW in detail, the matter of dispersion forces in DFT must be examined.

Dispersion interactions, also known as London dispersion forces or van der Waals interactions, are long range attractive forces. These interactions are brought about by electronic motion in one atom or molecule, instantaneously inducing responsive electronic motion in another atom or molecule. This correlated movement of electrons has led to an induced dipole, meaning there is a charge polarisation in both species. Subsequently, there

is an attractive force between the two systems. This induced dipole attraction decays with the inverse sixth power of the distance.[110] However, in a more complex system, there would also exist higher order polarised moments, such as, induced quadrupole-dipole, and quadrupole-quadrupole interactions.[111] The interplay between noble gas atoms is dictated solely by these forces.

These forces are entirely due to electronic correlation, and consequently the exact density functional must describe it perfectly. The current implementation of DFT considers the local density in its calculation of the exchange-correlation potential, V_{XC}, ignoring the density at other points, unless there is an overlap of densities. Essentially, the regions of electron density in our system, provided they do not directly perturb each other, are not 'aware' of each other so to speak. To account for dispersion forces, the local density approximation would have to be abandoned in favour of a truly nonlocal functional.

Throughout the literature, there seems to be two main approaches to including and calculating dispersion forces in DFT. The first approach aims to develop functionals that have been parameterised to systems that are dominated by dispersion forces. One such group of functionals are those from the Minnesota family of functionals. These functionals have received some criticism however, for their description of dispersion forces.[112,113] The second approach is to account for dispersion forces by adding an empirical correction to the DFT functional.

BEEF-vdW is a machine learned functional that accounts for dispersion forces via the inclusion of the van der Waals density functional (vdW-DF2).[109] The vdW-DF2 functional avails of the inclusion of a long-range correlation energy term, $E^{nl-c}[\rho(r)]$, which is a nonlocal functional of the density, and has the form:[114]

$$E^{nl-c}[\rho(r)] = \int\int \rho(r_1)\phi(r_1, r_2)\rho(r_2)\, dr_1 dr_2 \tag{2.46}$$

Where the kernel, ϕ, is a function of a function that is proportional to the exchange-correlation energy density at a point r. The BEEF-vdW functional incorporates this functional along with LDA and PBE to model account for exchange and correlation.

$$E_{xc} = \sum_{m=0}^{29} a_m E_m^{GGA-x} + a_c E^{LDA-c} + (1 - a_c)E^{PBE-c} + E^{nl-c} \tag{2.47}$$

The first term of this equation describes the contribution to exchange being calculated as the expansion of a GGA enhancement term, dependent on the reduced density gradient, in a power series using Legendre polynomials. Correlation is described as a linear combination of LDA correlation, E^{LDA-c}, semi-local PBE correlation, E^{PBE-c}, and a nonlocal vdW-DF2 type correlation, E^{nl-c}. Values for the parameters present in Eq. 2.46, were optimised using datasets of solid-state properties, non-covalent interactions, transition state energy barriers, and reaction and molecular formation energies, leading to the parameter $a_c = 0.60016648$ and a series of a_m values as seen in Table 2.1 below. In principle, this approach should construct a functional that is flexible and applicable to a large variety of different systems. Additionally, BEEF-vdW provides information regarding the uncertainty of the result obtained using an approximate exchange-correlation functional. Motivated by Bayesian statistics, an ensemble of over 20,000 other GGA functionals is constructed by varying the 31 parameters used in Eq. 2.47, which in turn is then used to define an estimation of the uncertainty for a result.

Table 2.1. Expansion coefficients a_m for the calculation of the Legendre polynomial for the exchange term in Eq. 2.47.

m	a_m	m	a_m	m	a_m
0	$1.516501714 \times 10^{0}$	10	$-1.573330824 \times 10^{-3}$	20	$5.761607992 \times 10^{-4}$
1	$4.413532099 \times 10^{-1}$	11	$5.036146253 \times 10^{-3}$	21	$-8.346503735 \times 10^{-4}$
2	$-9.182135241 \times 10^{-2}$	12	$-2.569472453 \times 10^{-3}$	22	$-4.458447585 \times 10^{-4}$
3	$-2.352754331 \times 10^{-2}$	13	$-9.874953976 \times 10^{-4}$	23	$4.601290092 \times 10^{-4}$
4	$3.418828455 \times 10^{-2}$	14	$2.033722895 \times 10^{-3}$	24	$-5.231775398 \times 10^{-6}$
5	$2.411870076 \times 10^{-3}$	15	$-8.018718848 \times 10^{-4}$	25	$-4.239570471 \times 10^{-4}$
6	$-1.416381352 \times 10^{-2}$	16	$-6.688078723 \times 10^{-4}$	26	$3.750190679 \times 10^{-4}$
7	$6.737855051 \times 10^{-4}$	17	$1.030936331 \times 10^{-3}$	27	$2.114938125 \times 10^{-5}$
8	$9.859205137 \times 10^{-3}$	18	$-3.673838660 \times 10^{-4}$	28	$-1.904911565 \times 10^{-4}$
9	$-6.737855051 \times 10^{-3}$	19	$-4.213635394 \times 10^{-4}$	29	$7.384362421 \times 10^{-5}$

2.2.6 DFT+U

We now turn from dispersion forces to the self-interaction error, (SIE), another weakness of modern DFT. We will discuss this problem in the context of a one electron system. For this system, we would expect Eq. 2.31 to be equal to zero, i.e., the classical Coulomb repulsion, $J[\rho(r)]$, should be equal to the negative of the non-classical electron-electron interaction contribution, $-E_{NC}[\rho(r)]$ and these two terms should cancel. However, E_{NC} is contained in the E_{XC} term, which is approximated independently of $J[\rho(r)]$ meaning that they do not cancel each other, and so an electron, even in a one electron system, will see and be repelled by its own electron density. This phenomenon favours an artificial delocalisation of the electron in question. Currently, there is no way to exactly account for the SIE, as we do not know the exact exchange-correlation functional. On-site corrections can be used to minimise the effects of the SIE and have been employed in this thesis via the DFT + U approach. This approach involves the addition of a Hubbard type parameter, U, and is one of the more popular on-site corrective methods in solid state DFT, effectively acting as a penalty to delocalisation. The method of Dudarev is applied in this thesis and is summarised below, although other methods do exist.[115]

$$E_{DFT+U}^{Dudarev} = E_{DFT} + \frac{U_{eff}}{2}\sum_{I,\sigma}\sum_{i}\lambda_i^{I\sigma}(1-\lambda_i^{I\sigma}) \tag{2.48}$$

$\lambda_i^{I\sigma}$ refers to the occupation number for an orthogonal set of localised orbitals i on atom I, with angular momentum σ, and should give values between 0 and 1, i.e., a fractional occupation. The correction itself disappears for values of 0 and 1. U_{eff} is the effective Hubbard parameter, defined as the difference between the on-site Coulomb parameter U and the on-site exchange parameter, J. The choice of the U_{eff} parameter is not trivial, as it is system dependent, meaning there is no systematic way to calculate the effective Hubbard parameter. Empirical approaches have been used in the literature, involving fitting to band gap or reaction energies. There do exist purely theoretical, *ab initio* approaches to the choice of U_{eff}, namely that of linear response DFT, or the approach developed by Lany and Zunger, wherein the addition of an electron should return a linear change to the energy of the system.[116,117] Care must be taken regarding DFT + U, as an applied correction may disfavour delocalised states that may be expected in certain chemical systems.

We have applied the Dudarev approach to DFT + U near the end of this thesis, in Chapter 6, for the modelling of iron oxides. Regarding the modelling of metal oxides, correcting for the SIE is of the utmost importance due to the strongly correlated nature of the d and f electrons, and the artificial delocalisation which may drastically affect the properties of the material. There also exists, in the field of DFT + U, an occupational control methodology, wherein the user can define a specific orbital occupation, the term $\lambda_i^{I\sigma}$ in Eq. 2.48, at the beginning of the calculation. This occupation is initially fixed to encourage optimisation towards the specified orbital configuration, avoiding undesired occupations and allowing for a much greater degree of control in the calculation of these strongly correlated materials.[118] This method has been employed near the end of the thesis for the modelling of iron oxides, namely magnetite, Fe_3O_4.

2.3 Periodic Density Functional Theory

DFT has been applied across various areas of chemistry with great success. However, the transition from modelling molecular species to the solid state warrants extra consideration. We can define a molecule as a cluster of individual atoms, with unique spatial coordinates, held together by attractive forces. This thesis, being focused on heterogeneous catalysis, involves the modelling of crystalline solids, macroscopic objects defined by the massive number of atoms that constitute them, of the order of Avogadro's number. These systems are effectively treated as infinitely large. Modelling such a system is in one simulation cell is impossible. The modelling of these surfaces with "standard" DFT in a cubic simulation cell, is incorrect, as our solid system would have surface atoms on all sides, which would experience different forces than those of the bulk atoms, which would invariably lead to difficulties in the optimisation of bulk systems.

2.3.1 Boundary Conditions and Bloch's Theorem

The application of periodic boundary conditions (PBC) fixes this issue and allows for the calculation of crystalline solid-state systems. We define a simulation cell via the lattice vectors and lattice points. An atom that leaves the simulation cell immediately enters the cell on the opposite side, as depicted in Figure 2.1, thus imposing periodicity into the system.

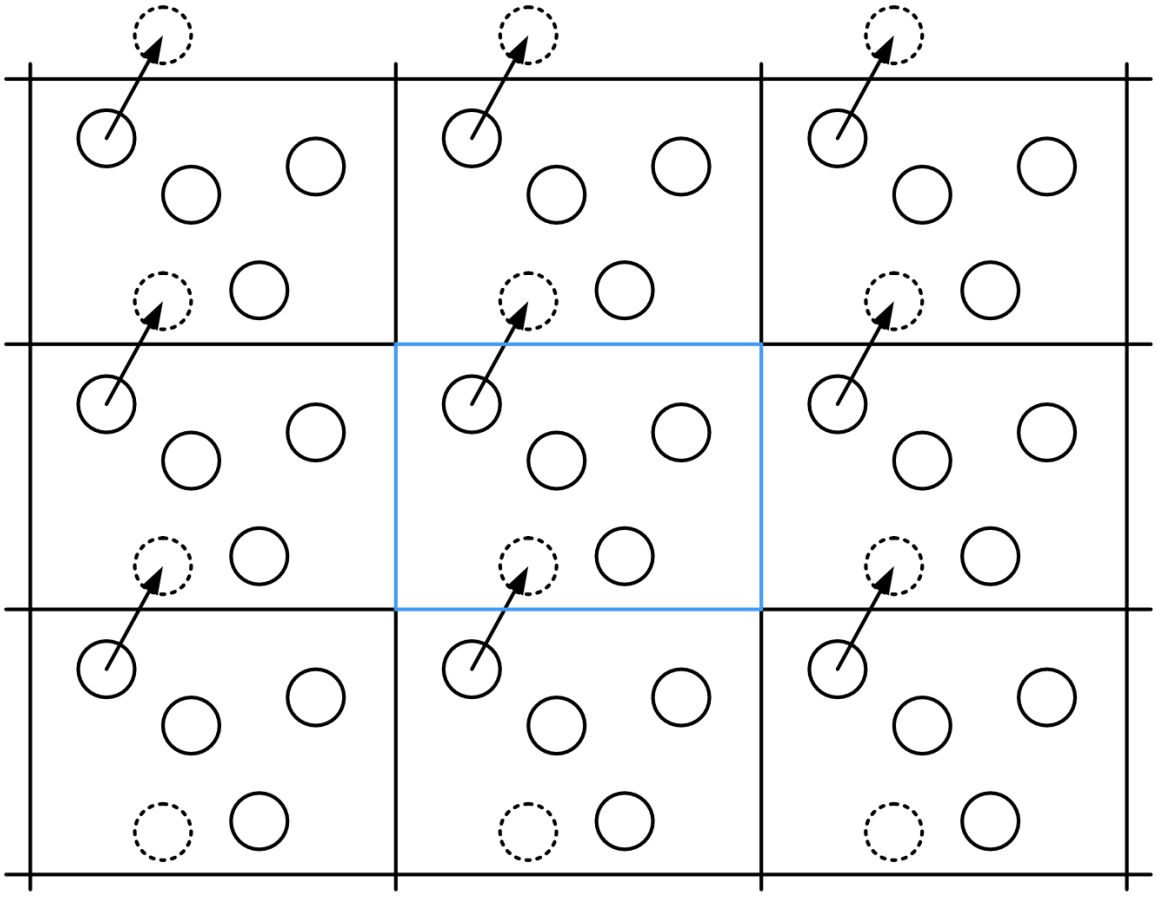

Figure 2.1. Graphical depiction of periodic boundary conditions being employed. The simulation cell being explicitly modelled in question is outlined in blue. An atom is shown moving to a neighbouring cell.

If we are to solve the Schrödinger equation for a wavefunction in a periodic system, then that wavefunction must obey Bloch's theorem, shown below.

$$\psi_{j,k}(r) = e^{ik\cdot r} u_{j,k}(r) \tag{2.49}$$

Bloch's theorem states that, for an electron in a lattice, the solutions to its wavefunction can be found in the form of a plane wave multiplied by a periodic function, $u_k(r)$. As crystalline solids are made up of many bands, wavefunctions of this type are typically written in the form, $\psi_{j,k}(r)$, where j is the index describing individual bands and k is a factor describing the phase dependence of these bands, analogous to in-phase and out-of-phase orbital interactions in a molecule. To summarise, Bloch's theorem splits the wavefunction into a cell-periodic component and a wave-like component.

2.3.2 Reciprocal Space

For mathematical convenience, reciprocal space is used in favour of real space. The concept of reciprocal space is central to periodic DFT calculations and as such, warrants discussion. Points in real space can be defined in terms of the lattice vectors, a_1, a_2, and a_3, *i.e.*,

$$r = (n_1 a_1, n_2 a_2, n_3 a_3) \tag{2.50}$$

We can also define reciprocal space vectors, G, in terms of reciprocal lattice vectors, b_1, b_2, and b_3.

$$G = b_1, b_2, b_3 \tag{2.51}$$

$$b_1 = 2\pi \frac{a_2 \times a_3}{a_1 \cdot a_2 \times a_3}, b_2 = 2\pi \frac{a_1 \times a_3}{a_2 \cdot a_1 \times a_3}, b_3 = 2\pi \frac{a_1 \times a_2}{a_3 \cdot a_1 \times a_2} \tag{2.52}$$

Considering a simple cubic lattice, each of the real lattice vectors, a_i, has a value of a. Consequently, the corresponding reciprocal space lattice vectors, b_i, will have a value of $2\pi/a$. This also brings to light an important concept, that larger real space lattice vectors correspond to shorter lattice vectors in reciprocal space.

The primitive cell can be defined as the unit cell that contains the minimum number of atoms needed to fully define a crystalline solid over an infinite space. In simpler terms, it is the smallest crystallographic cell that still contains all the necessary information to describe that material. The primitive cell can also be defined in reciprocal space, and due to its useful properties, is referred to as the first Brillouin zone (BZ), after Léon Brillouin, who was a founding figure of many concepts in solid state physics.

2.3.3 The Brillouin Zone and Plane Wave Basis Sets

The BZ describes unique values of k, meaning any point outside of the BZ does not provide a new wavefunction, rather it is a repetition of a point in the BZ. The centre of the BZ is denoted by k = 0 and is referred to as the gamma (Γ) point. Previously, k was defined as a phase factor, but it is also wavevector in reciprocal space. These wavevectors are referred to as k-points. By virtue of the gamma point being central, k-points are sampled between $k = -\pi/a$ and π/a. It should be noted that the phase interactions from 0 to π/a are equivalent to those from 0 to $-\pi/a$, and so the calculation of both is redundant. In principle, an infinite number of k-points in the BZ exists. However, the energy varies smoothly across

k-points that are similar, so the calculation of only a sampling of k-points is necessary to acquire a good description of the periodic solid.

The periodic function, $u_{j,k}(r)$, in Eq. 2.49 is expressed in terms of reciprocal lattice vectors.

$$u_{j,k}(r) = \sum_{G} C_{j,G} e^{iG \cdot r} \tag{2.53}$$

Where we sum over all reciprocal space vectors, G. The term $C_{j,G}$ is a coefficient for a particular plane wave for each band j. Subsequently, the entire Bloch wavefunction can be written as follows.

$$\psi_{j,k}(r) = \sum_{G} C_{j,k+G} e^{i(k+G) \cdot r} \tag{2.54}$$

The plane wave term now includes the summation of phase factor and the reciprocal space vectors, $(k + G)$. The coefficients are now obtained for each plane wave, at every k-point, for every band. This expression implies that determining a solution to the wavefunction at a single k-point requires a summation over all possible values of G, of which there is an infinite number, the calculation of which is not practical. More high energy plane waves, *i.e.*, larger G, provides a more accurate description of the periodic solid, but also increases the computational cost. Coupling this with the fact that plane waves with smaller kinetic energies are typically more important than those with larger kinetic energy allows us to truncate the plane wave basis set.[119] As such we only calculate plane waves that have a kinetic energy lower than a user defined plane wave cutoff energy, E_{cut}, written below.

$$E_{cut} = \frac{1}{2} |k + G|^2 \tag{2.55}$$

The simulation cell is then filled with plane waves of energy up to this value of E_{cut}. This parameter is defined by the user and is dependent on the material being investigated. It should also be kept in mind that when comparing energy differences for different systems the same value of E_{cut} must be used in all calculations.

2.4 Modelling Reaction Mechanisms

2.4.1 Potential Energy Surface

The concept of the potential energy surface (PES) is one of the cornerstones of theoretical chemistry, providing us with a useful depiction of the relationship between the energy of a chemical system and the geometry of its components. In simpler terms, the PES is named so because the energy of the system being studied is dependent upon its position, i.e., potential energy. A simple example for the illustration of the PES can is illustrated in Figure 2.2 below.

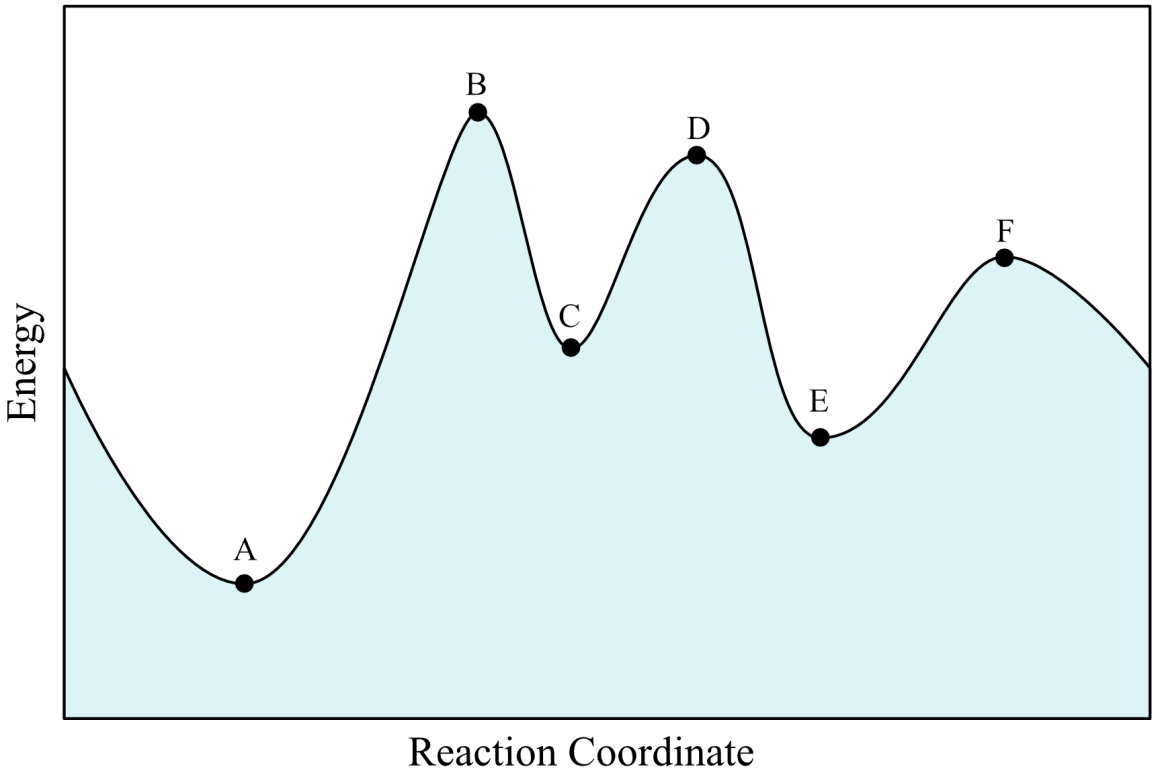

Figure 2.2. A simplified representation of the PES, wherein the energy is plotted as a function of an arbitrary reaction coordinate. Extrema of the function are labelled from A – F. For most systems, the PES is multidimensional and impossible to visualise.

The PES is not only a powerful tool for visualising the pathway from reactants to products, but it is also essential for understanding how computational chemistry programs find and characterise chemically relevant geometries. The points that we are interested in on the PES are *stationary points*, points that are flat with respect to a geometric parameter or reaction

coordinate, *i.e.,* the gradient of the point is zero. However, as can be seen in Figure 2.2, stationary points are not uniform and must be characterised. For example, points A, C and E are all referred to as *minima* on the PES. Minima are points on the PES that describe stable states of the system and are characterised in Figure 2.2 by a positive second derivative. We must also distinguish between the *global minimum*, point A, which describes the most stable arrangement of atoms, and the *local minima*, points C and E, which refer to minima that are not as stable as the global minimum.

The points B, D and F are *maxima* on the PES, and represent points of chemical instability. A point that is a maximum along one direction of the PES is characterised as a transition state (TS). For example, point D in Figure 2.2 could be viewed as a transition state between the stable configurations represented by points C and E. It should be stated that Figure 2.2. representing only a subset of variables along the PES cannot represent a *true maximum*, which a point on the PES from which all directions lead to a decrease in energy.

It should be kept in mind that this is a very simple example and does not capture the complexity of a much larger system. The PES describes the energy as a function of all the variables present in the system. For the vast majority of cases this would be a set of bond lengths and angles, which can grow increasingly complex with larger systems.

2.4.2 Geometry Optimisation

When examining systems of interest, we tend to look at the configuration that correspond to minima on the PES, as normally these configurations would be observed in experiment. However, given that the PES is multidimensional and impossible to visualise, it is all too possible that multiple minima are present. As stated before, a minimum is a turning point on the PES, and consequently the gradient, g, of the potential energy at a minimum is by definition, zero. It should also be kept in mind that the forces, F, acting upon the atoms is the negative of the gradient, so we also define a minimum as a configuration of zero force. This information is summarised in Eq. 2.56 below for a reaction coordinate r.

$$-F = g = \frac{dE}{dr} \tag{2.56}$$

As stated before, the PES is incredibly complex, so how does one find the configuration of atoms that corresponds to a minimum? Chemical intuition can only bring us so far when dealing with bond length differences that are less than an angstrom. As a result, we must apply iterative procedures to 'optimise' our chemical system as close to a minimum until certain convergence criteria are met. These methods all require an initial guess, x_0, supplied by the user, the calculation of a search direction, h_i, and a step length, λ, in that direction that may also be user defined. These methods generally follow the following procedure.

$$x_{i+1} = x_i + \lambda h_i \tag{2.57}$$

Frustratingly, the user defined initial guess means that our system optimises to a nearby minimum, as opposed to the global minimum. There is no way to determine whether a minimum is the global one or not, warranting systematic sampling of all possible minima. The simplest way to find a minimum is to use the method of steepest descent, wherein the search direction is set as the negative of the gradient.

$$h_i = -g_i \tag{2.58}$$

While this method guarantees optimisation towards a minimum, it gets quite slow, with the path taken being a '*zig-zag*' along the direct path to the minimum. As such, the steepest descent method tends to be incorporated into more complex methods, such as the conjugate gradient method. This method is built upon the premise of avoiding interference across search directions, by including the conjugate of the gradient in the evaluation of the next search direction, as described below. This allows for a more direct path to the minimum.

$$h_{i+1} = -g_{i+1} + h_i \frac{g_{i+1} \cdot g_{i+1}}{g_i \cdot g_i} \tag{2.59}$$

For this method, the initial search direction, h_o, is set to the negative of the gradient, i.e., we perform a steepest descent step first. Subsequent steps utilise Eq. 2.59 to optimise towards a minimum on the PES and have been used to optimise the geometries of intermediates throughout this thesis.

The methods described thus far are termed as first-order methods, that is to say, they only require the first derivative of the energy, the forces. Second derivative methods can be used to great effect to obtain information regarding the curvature of the PES, so as to better

inform our step direction. The Newton-Raphson method (Eq. 2.60) uses the inverse of the second derivative matrix, A_i^{-1}, the Hessian matrix, as a search direction.

$$x_{i+1} = x_i - A_i^{-1} g_i \tag{2.60}$$

This allows each variable to have a specific step direction that is dependent upon the force and curvature of the PES at that point. However, the calculation of the Hessian matrix takes a much longer time to calculate than the gradient. This issue is exasperated for larger systems and more complex energy surfaces. Additionally, as the step direction is informed by the Hessian, any negative value in the Hessian matrix will reverse the gradient, and optimise that specific variable away from a minimum, i.e., towards a maximum. While this can be infuriating when trying to optimise the system towards a minimum, it can be used to converge to a point where we have a maximum in one direction on the PES, a transition state (TS). A variation of the Newton-Raphson, the Quasi-Newton method, has been used throughout this thesis for locating TS's. The Quasi-Newton method avoids calculating the Hessian explicitly and instead updates the inverse of the Hessian, H_i, gradually from gradient information calculated at each step.

$$x_{i+1} = x_i - \alpha_i H_i g_i \tag{2.61}$$

This method avoids the costly calculation of the Hessian matrix while ensuring that it is positive via the updating procedure.

Of course, at some stage these calculations must end. Ideally, calculations should stop exactly at a minimum, when all the forces are zero. However, computational accuracy is only so finite, and the calculation of the forces can only be done to a certain precision. Therefore, we must set a convergence criterion, stating that the calculation is, for all intents and purposes, at a minimum once the forces are less than a certain threshold.

2.4.3 Transition States

Optimisation towards a minimum on the PES is a straightforward procedure. Should all conventional methods fail, the steepest descent is guaranteed to lower the potential energy, albeit not in an efficient manner. The location of a transition state (TS) on the PES is more challenging. As far as we are aware, there is no method that is infallible. Two types of methods exist for the determination of a TS, local and interpolation methods. Interpolation methods are straightforward to conceptualise, taking the geometries of a reactant and

product and assuming that a TS is between those two geometries. Local methods do not use any information about the reactants and products, rather they are led by first or second derivative information at a point on the PES. Both methods have been applied in this thesis and so will be discussed below.

The simplest interpolation approaches focus on certain reaction coordinates that describe the main difference between the reactant and product geometries. A simple example for this would be selecting bond distances for a bond breaking or forming process, or bond angles for a TS involved in a change in conformation, an example of which can be seen below in Figure 2.3.

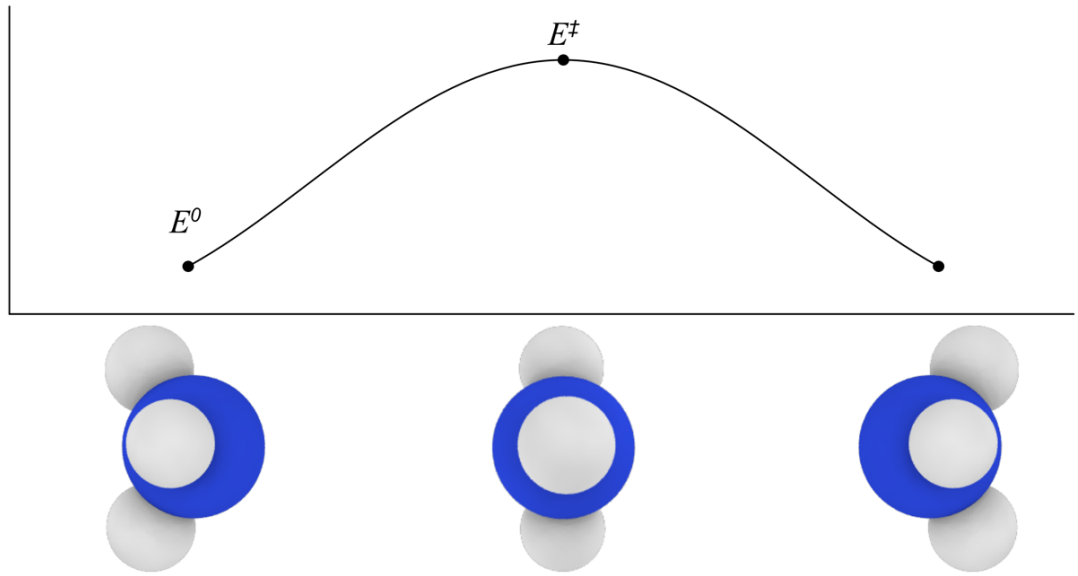

Figure 2.3. In the case of the inversion of ammonia, the reaction coordinate of interest would be the HNH bond angle. The bond angle can be fixed to 120° to construct the planar TS involved.

However, this approach assumes the TS to be a halfway point between a reaction coordinate and fails for more complex systems. Interpolation methods containing multiple geometries, or 'images', between the product and reactant structures have been developed. Such interpolation methods may be referred to as "chain-of-state" methods. The optimisation of several images between two minima not only provides a TS, but also approximates the minimum energy path (MEP) between the two states. A popular chain-of-state method is the nudged elastic band (NEB) method.[120] The NEB method defines a target function,

$$T_{NEB}(R, x_1, x_2, \dots, x_M, P) = \sum_{i=1}^{M} E(x_i) + \sum_{i=1}^{M-1} \frac{1}{2} k(x_{i+1} - x_i)^2 \qquad (2.62)$$

This function is composed of two terms. The first is the sum of the energies of each image along the MEP. The second term is a penalty term, defined by a spring constant k, the purpose of which is to distribute the images evenly along the MEP. Some common issues with this approach are related to this spring constant. Should it be too strong, then none of the images will be allowed to approach the TS and what is referred to as "corner-cutting" near the TS will occur. Additionally, if the spring constant is too weak, then the images will collapse back into the minima closest to them.

In light of these problems, we can "nudge" the elastic band calculation which is done in two ways. Only the component of the spring force that is parallel to the tangent of the MEP is used in the penalty term of Eq. 2.62, and only the perpendicular component of the optimising force is applied. Another issue often encountered with these calculations is that the spring constant may prevent images from finding the TS, especially when it is in a very narrow region of the NEB. The employment of the climbing image nudged elastic band (CI-NEB) method developed by Jónnson *et al*.[121] remedies this problem. When performing a CI-NEB calculation, a regular NEB calculation is performed for a few iterations first. The highest energy image along the MEP is identified and the spring forces are removed for that image. Additionally, this high energy image is optimised away from the minima, towards the saddle point. This optimisation towards a maximum is informed by the remaining images, which define the relevant degrees of freedom to be optimised.

While these NEB methods are useful in providing a good description of the MEP between two minima on the PES, it should be kept in mind that they can be computationally very expensive. DFT calculations are performed for M images, meaning we have $3M$ degrees of freedom to optimise for these calculations.

Local methods tend to be based upon the Newton-Raphson approach discussed previously. As said previously, this approach may be used to find a nearby TS as long as it is sufficiently close to one, that is to say, the Hessian matrix must have a negative eigenvector in one direction, which we essentially 'walk' up. However, the calculation of the Hessian is very costly, leading to the approach of approximating and updating it via quasi-Newton methods.

However, even this updating of the Hessian can be computationally demanding, as can its manipulation, i.e., storing and diagonalising.

The dimer method avoids the need for the Hessian matrix via the construction of two images, referred to as the 'dimer', which are separated by a point equidistant between them.[122] The forces and energies of these two images are calculated initially. The force acting on the midpoint is simply the average of the image forces, and its energy is the sum of both image energies. These two images, which are kept at a fixed distance from each other, are first displaced, and then rotated towards a configuration that minimises the energy of the dimer. Following this, the dimer is displaced along the minimum curvature mode which is the line connecting the two images of the dimer, and subsequently the forces and energies are recalculated. An improvement to the dimer method was implemented by Keil *et al*.[123] This method differs from the original dimer method as it employs a linear extrapolation using the forces at the first image and the midpoint to approximate the force at the second image. The calculation of the dimer midpoint, as opposed to its approximation, allows for an effective convergence of the midpoint to a saddle point, while reducing the number of conjugate gradient calculations for each dimer translation. This method also differs from the original dimer method as the user can read in the curvature towards a saddle point from a pre-calculated Hessian matrix.

While local methods are much less expensive than interpolation methods, they do suffer from the fact that they rely on an initial guess supplied by the user. If this guess is not close to a TS, then convergence will suffer. A common approach, that has been employed in this thesis, is to apply an interpolation method to provide a description of the MEP between a reactant and product for a small number of steps. The highest energy image, which is assumed to be close to the saddle point, can then be taken as the initial guess for a local method.

2.4.4 Optimisation of Bulk Crystals

Prior to the modelling of any adsorbate or TS structure, the atomic structure of the material itself must be optimised. Throughout this thesis I have only worked with materials that have cubic bulk systems, which drastically simplifies things. Bulk unit cells may be acquired from several different databases, such as the *Materials Project,* the *Crystallography Open Database*, and *The Open Quantum Materials Database*, to name a few.[124–135] However,

upon acquiring a bulk unit cell, it is always prudent to optimise it to the ground state, for a given level of theory. This would be step one in modelling a solid-state material. Step zero however, would be the determination of the number of *k*-points and the kinetic energy cutoff. For most calculations a kinetic energy cutoff of 500 eV is sufficient, although for certain cases higher cutoffs may be needed. The optimisation of the *k*-point density is done by gradually increasing the size of the *k*-point set until the change in the calculated energy is less than 1.0 meV per atom.

Returning to the optimisation of the bulk unit cell, we can employ the variational principle to great effect here, as the ground state of a system is the one with the lowest energy. Consequently, we can calculate the energy of the system as a function of the lattice parameter, to determine the lowest energy configuration. The lattice parameter is the main parameter to be optimised and may be optimised to different values depending on the choice of functional. We calculate the total energy of the bulk unit cell as a function of the lattice parameter, i.e., we change the volume of the unit cell. The resulting energies and volumes can be fitted to an equation of state, in the case of this thesis, the Birch-Murnaghan equation of state.

$$E(V) = E_0 + \frac{9V_0B_0}{16}\left\{\left[\left(\frac{V_0}{V}\right)^{\frac{2}{3}} - 1\right]^3 B_0' + \left[\left(\frac{V_0}{V}\right)^{\frac{2}{3}} - 1\right]^2 \left[6 - 4\left(\frac{V_0}{V}\right)^{\frac{2}{3}}\right]\right\} \qquad (2.63)$$

Where, E_0, V_0, and B_0 refer to the energy, the volume, and the bulk modulus at equilibrium, V is the volume of the bulk crystal, and B_0' the derivative of the bulk modulus (the resistance of a material to compressions) with pressure. In practice, we optimise the bulk cell using a guess of the lattice parameter or volume, using experimental data or values from theoretical databases such as the Materials Project.[124] We then increase/decrease the volume of the cell by *ca*. 5% around that initial guess, bracketing the equilibrium structure. The Birch-Murnaghan equation of state provides us with the equilibrium volume or lattice constant, which is then used to relax the structure in a final optimisation.

2.4.5 Solvation

The vast majority of chemistry is performed in the presence of a liquid phase environment, the modelling of which is much more complex than that of gas phase processes. The solvent tends to be modelled in three ways which, in order of increasing computational cost, are

referred to as implicit, hybrid, and explicit solvation models. Implicit solvation involves accounting for the solvent via the inclusion of a dielectric continuum. These continuum methods model thermodynamically averaged properties and neglect site-specific interactions, consequently neglecting important aspects of a catalytic system.[136–138] Throughout this thesis the bulk solvent environment is approximated via the implicit solvation software VASPsol developed by Hennig *et al.*[139,140] This software divides the system into the solute and solvent regions, describing the ground state energy of the entire solvated system, A, as follows,

$$A[n_{solute}(\vec{r}), \phi(\vec{r})] = A_{TXC}[n_{solute}(\vec{r})] + \int \phi(\vec{r})\big(N_{solute}(\vec{r}) - n_{solute}(\vec{r})\big)d^3r - \int \epsilon(\vec{r})\frac{|\nabla\phi|^2}{8\pi}d^3r + A_{cav} \quad (2.64)$$

Where the ground energy, A, is a functional of the electron density of the solute, $n_{solute}(\vec{r})$, and the total electrostatic potential, $\phi(\vec{r})$, due to the solute system in the polarisable medium. This energy is separated into four contributions, the first of which, A_{TXC}, is the kinetic and exchange-correlation energy of the solute in the absence of solvent effects. The second term accounts for the interaction of the electrostatic potential with the nuclear and electron charge densities, denoted as $N_{solute}(\vec{r})$ and $n_{solute}(\vec{r})$ respectively. The third term is the electrostatic energy contribution of the polarisable solvent, which is modulated by a relative permittivity term, $\varepsilon(\vec{r})$, which is dependent upon position. This energy contribution accounts for the polarisation effect of the solvent in response to the solute system. As this response is stabilising, this term is preceded by a negative sign. The final term, A_{cav}, is the cavitation energy, *i.e.*, the energy needed to displace the solvent and create a cavity for the solute.

The form of this latter value is an important consideration in the field of implicit solvation. A common approach is to surround the solute species with sphere and consider the cavity to be the union of said spheres. Within this cavity, the permittivity is that of the vacuum, whereas outside it has the value of the solvent. VASPsol utilises a diffuse dielectric cavity, ensuring a seamless transition between vacuum and solvent phases. A_{cav}, being the energy required to construct this cavity, has the following form.

$$A_{cav} = \tau \int |\nabla \mathrm{S}| d^3 r \tag{2.65}$$

Where τ is the effective surface tension parameter. A higher surface tension parameter implies strong solvent-solvent interactions, meaning it will be more costly to generate a cavity. The default value for this term 0.525 meV Å^2. The term S describes the shape of the cavity and has the form,

$$S\left(n_{solute}(\vec{r})\right) = \frac{1}{2} erfc\left\{\frac{\log\left(\frac{n_{solute}}{n_c}\right\}}{\sigma\sqrt{2}}\right\} \tag{2.66}$$

The cavity shape function, $S(n_{solute}(\vec{r}))$, is a function of the electron density of the solute. The parameters n_c and σ determine the value of the electron density at which the cavity begins to form and the thickness of the cavity, respectively. Figure 2.4 illustrates the smooth transition between the solvent and solute or vacuum phase.

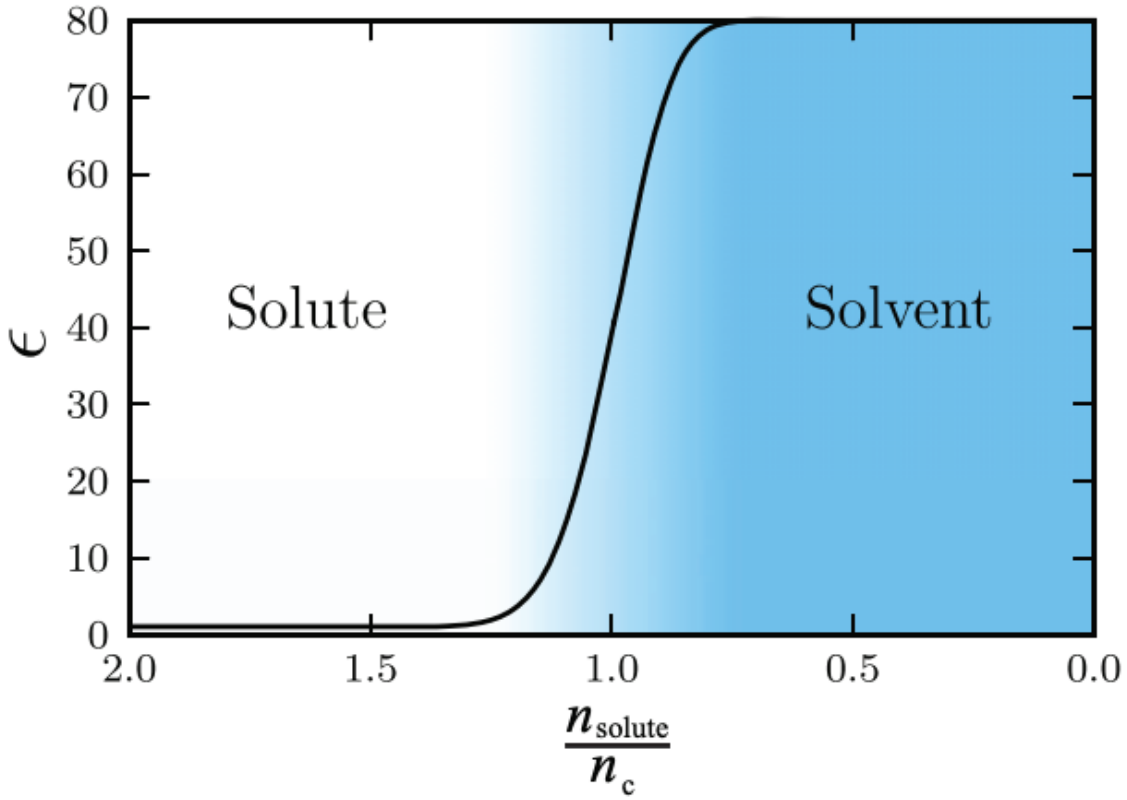

Figure 2.4. The relative permittivity varies smoothly from the vacuum value ($\epsilon = 1$) to that of the solvent, which in this case is water ($\epsilon = 80$). The default values of n_c and σ used in VASPsol are 0.0025 Å^{-3} and 0.6, respectively. All default values employed by VASPsol have been obtained from the work of Arias *et al.*[141]

who fitted their models to experimental solvation energies for molecular species in water. Figure reproduced from the work of Hennig *et al*.[139] with permission obtained from AIP Publishing.

Additionally, this cavity shape function is used to determine how the relative permittivity of the solvent varies with the solute electron density.

$$\varepsilon(\vec{r}) = 1 + (\varepsilon_b - 1)S\big(n_{solute}(\vec{r})\big) \tag{2.67}$$

Effectively, the shape of the cavity modulates, using the solute electron density, how the relative permittivity changes from the relative permittivity of the vacuum, *i.e.*, 1, to that of the solvent, ε_b.

In principle, implicit solvation models are coarse-grained models. They approximate the behaviour of a system by using a simplified representation of that system. In doing so, they are cost effective and therefore practical, however they neglect the inclusion of site-specific interactions such as hydrogen bonds between the solvent and solute.

On the other end of the spectrum, there exists explicit solvation models, where the simulation cell is filled with solvent molecules that are calculated explicitly, and at the same level of theory as the solute. Firstly, it becomes obvious that this is too expensive computationally and therefore not practical. Secondly, the calculation of these explicit solvation models is only as good as the method being used. DFT, the method of choice due to its ability to calculate larger supercells with computational efficiency, has been known to miscalculate such systems.[142,143] It is important to note that the solvent is dynamic, meaning a vast number of configurations may exist. This has engendered the use of *ab initio* molecular dynamics (AIMD) methods to simulate the liquid phase and capture this ensemble of configurations. However, timescales of nanoseconds or longer may be necessary to model the solid liquid phase depending on the systems and how fast diffusion may occur.[144] While the exact modelling of the solvent is currently not feasible, explicit solvent models have been constructed and utilised with specific aims.

Regarding the modelling of processes on surface slabs, the ice-like water layer (or water bilayer) has become a very popular model for the approximation of the aqueous electrolyte and its effect on the thermodynamics and kinetics of electrochemical processes.[145–150] The water bilayer, depicted below in Figure 2.5, has been observed on several transition metal surfaces and tends to form hexagonal rings of water.[151,152] Each water atom is bound to

three other water molecules via H-bonding and may or may not have a H atom pointing perpendicularly to the surface. The water bilayer model may be modelled with hydrogen atoms pointing to or away from the surface. The orientation of these H atoms has been shown to vary across transition metal surfaces. Schnur and Groß found, via AIMD simulations, that a H–down orientation is preferred for Au(111), Ag(111), Pt(111) and Pd/Au(111) surfaces, where the Pd/Au system refers to a monolayer of Pd atoms placed on a Au(111) slab.[153] H–up orientations do exist and have been calculated to be preferred on Ni and Cu surface slabs.[154,155]

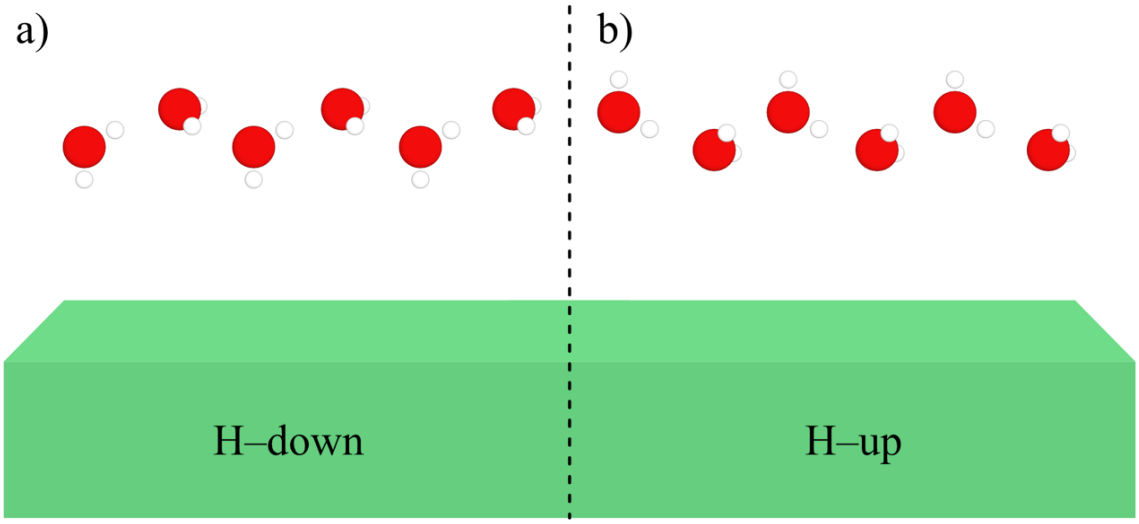

Figure 2.5. Depiction of the water bilayer where the H atoms of the ice-like water atoms are pointing (a) down at the surface and (b) away from the surface. These orientations are commonly referred to as H–down and H–up water bilayers, respectively.

This model has been used extensively in DFT simulations due to its inclusion of site-specific effects and relative cost effectiveness. Additionally, the water bilayer may include excess H atoms, which become solvated protons. The corresponding electrons becomes localised in the surface, which in an electrochemical context effectively simulates an electrochemical double layer.[145,156–159]

A middle ground between implicit and explicit has been extensively studied, dubbed hybrid solvation, or microsolvation.[160–162] This involves modelling a small amount of explicit solvent molecules to capture site-specific effects in the presence of a dielectric continuum,

which emulates the bulk solvent. However, there remains the question of how many solvent molecules to model and where to place them in the simulation cell.

2.4.6 Thermodynamic Corrections

Identification of a reaction step as spontaneous under realistic conditions is done by calculating the difference in Gibbs energies between the reactants and products. The Gibbs energy, G, can be defined as follows,

$$G = H - TS = U + PV - TS \tag{2.68}$$

Where H refers to the enthalpy of the system, defined as the sum of the systems' internal energy, U, and the product of the pressure and volume, pV. S is the entropy of the system, which can be, at a basic level, equated with the level of disorder. A perfect crystal with no defects would have a small entropy, whereas a gas would have a large entropy. This description is misleading and is quickly replaced when looking through the lens of statistical mechanics, where entropy describes the number of accessible microstates that may be occupied for a certain macrostate. A larger entropy means more microstates may be occupied, etc. Determining the difference in Gibbs energy between the products and reactants in a chemical process allows us to determine the spontaneity of the process.

$$\Delta G = \sum G_{products} - \sum G_{reactants} \begin{cases} < 0, exergonic \\ = 0, equilibrium \\ > 0, endergonic \end{cases} \tag{2.69}$$

Regarding the study of molecular systems, some of which are investigated during this thesis, the assumption is made that these systems behave as non-interacting particles, i.e., as an ideal gas. As such, contributions to the enthalpy and entropy terms may be separated into translational, rotational, vibrational, and electronic contributions.

$$H = E_{DFT} + E_{ZPE} + \int_0^T C_P dT \tag{2.70}$$

$$S_{tot} = S_{trans} + S_{rot} + S_{vib} + S_{elec} - k_B \ln\left(\frac{P}{P_0}\right) \tag{2.71}$$

The enthalpy, H, is calculated as the sum of the electronic energy calculated, in the case of this thesis, via DFT, the zero-point energy, E_{ZPE}, and the heat capacity at constant pressure, C_P, from 0 K to a temperature T.

When considering adsorbates bound to a surface, the Helmholtz free energy, F, is calculated, as the system is at a constant volume. Additionally, the translational and rotational terms are deemed as negligible.

$$F = U - TS \tag{2.72}$$

Considering the PV term as zero in Eq. 2.68 allows us to treat the Helmholtz energy as the Gibbs energy, meaning we can define the internal energy and the entropy terms as the following.

$$U = E_{DFT} + E_{ZPE} + \int_0^T C_{V,vib} dT \tag{2.73}$$

$$S = S_{vib} \tag{2.74}$$

Additionally, for heterogeneous catalytic systems, atoms comprising the surface tend to be fixed, and vibrational contributions for only the adsorbate species are calculated.

2.4.7 Bader Charge Analysis

A large portion of the field of descriptive chemistry is founded upon the observation that atoms, or a collection of atoms, in a molecule, or solid, exhibit characteristic properties that vary only slightly across systems. An example of this concept would be the existence of functional groups, the behaviour of which can be used to predict how a system will behave. As discussed previously, all properties of a system can be understood from the wavefunction ψ, however it must be kept in mind that any observable properties are indicative of the whole system. Richard Bader aimed to bridge the gap between quantum mechanics and chemistry with his theory of atoms in molecules (AIM).[163]

Quantum chemical theory does not directly define atomic charges in molecules or solids. DFT outputs the electron density and does not directly define atomic charges in molecules or solids. A commonly used charge partitioning scheme that is employed in theoretical chemistry is Mulliken analysis, however this approach utilises localised basis sets, and therefore is not applicable to periodic systems where plane wave basis sets are required. Instead, we take advantage of the Bader charge analysis method using the program developed by developed by Henkelman *et al.*[164] In this method of charge partitioning, an atomic volume is defined as the region in space that is bounded by all surrounding zero-flux surfaces. In simpler terms, we can imagine a maximum in the electron density, that is

the nucleus of an atom, as our starting point. As we move further from this maximum, we move opposite the density gradient until the gradient reaches zero and starts to rise again, presumably to another maximum (nucleus). At the point where the gradient is zero there is a bond between two atoms, which also denotes where the zero-flux surface is. When using Bader charge analysis, the partial atomic charge is calculated as the difference between the nuclear charge and number of electrons found within the region of atomic space,

$$q_i = Z_i - \int_{\mathrm{V}_i} \rho(r) dr \tag{2.75}$$

Where V_i refers to the volume of the atomic region bound by the zero–flux surface, and the number of electrons is calculated as the integral of the density over space.

2.4.8 Non-Covalent Interactions

Non-Covalent Interactions (NCIs) are generally weak interactions between atoms or molecules that are not covalently bound to each other. It is a term that encapsulates van der Waals interactions, hydrogen bonding, and electrostatic interactions. A popular program to characterise and visualise NCIs for both molecular and periodic systems is the Critic2 software,[165,166] which calculates the reduced density gradient $s(\rho)$, from the electron density ρ as follows:

$$s(\rho) = \frac{1}{2(3\pi)^{\frac{1}{3}}} \frac{|\nabla\rho|}{\rho^{\frac{4}{3}}} \tag{2.76}$$

The reduced density gradient between interacting atoms can change quite drastically due to weak intra- or intermolecular interactions, leading to density critical points between fragments defined by the user. Troughs can be seen in the reduced gradient density due to these bond critical points with both attractive and repulsive interactions appearing in the same reduced density gradient region. As such, the curvature of the density must be examined to determine the nature of these interactions. This is done by inspecting the eigenvalue contributions to the second derivative electron density matrix, also known as the Hessian matrix, λ_i, so that $\nabla^2\rho(r) = \lambda_1 + \lambda_2 + \lambda_3$. The sign of the second eigenvalue, λ_2, is used to determine whether an interaction is repulsive or attractive.[167,168]

Increased electron density perpendicular to a bond critical point denotes an attractive interaction and is characterised by $\lambda_2 < 0$. Conversely, repulsive interactions, where

density is depleted at these points, are observed with $\lambda_2 > 0$. By plotting the reduced density gradient against the sign of λ_2 multiplied by the electron density ρ one can observe the various NCIs between user defined fragments of a system. It should be stated that NCIs calculated via Critic2 are intended to provide qualitative results and have been interpreted as such.[168]

2.5 Computational Electrocatalysis

The ability of an electrode to precisely add or remove electrons from chemical species makes electrochemistry a field full of potential. Additionally, the underlying concept is deceptively simple. As opposed to using a chemical oxidant/reductant, redox processes can be performed by lowering or raising the energy of electrons in an electrode. For example, the electrochemical reduction of a species A^+, as shown below in Figure 2.6, occurs when the energy of the electrons in the electrode are at a higher energy than the lowest unoccupied or singly occupied molecular orbital (LUMO and SOMO, respectively) of A^+.

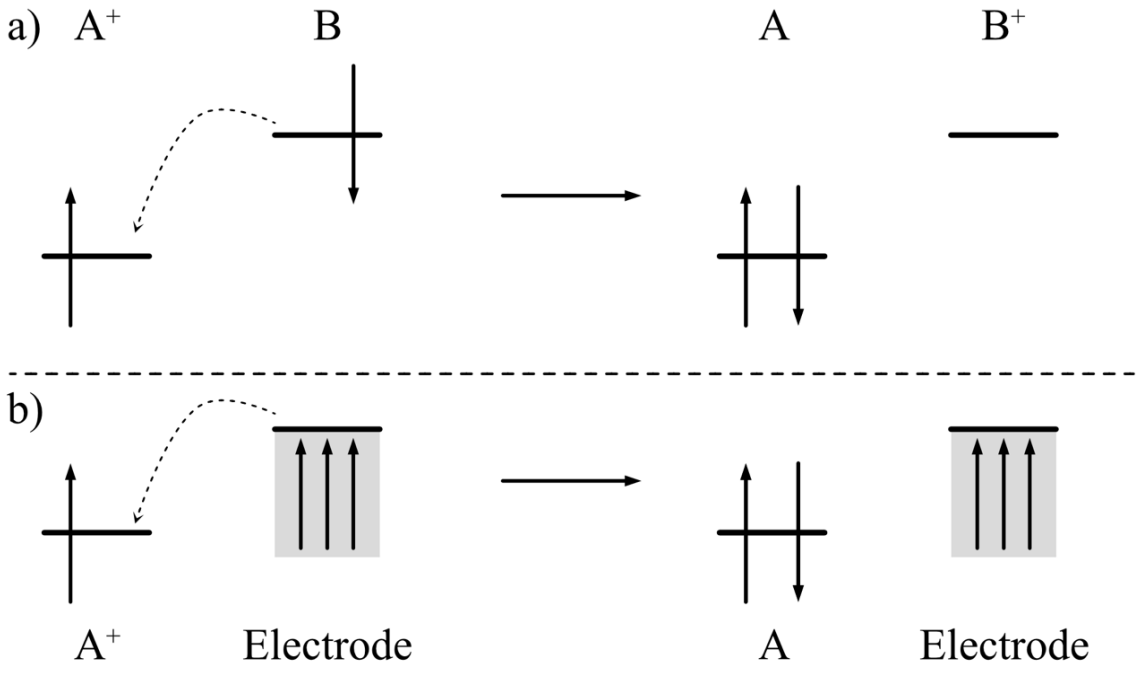

Figure 2.6. Reduction of species A^+ to A using (a) a chemical reductant, B, and (b) using an electrode. The transfer of an electron from an electrode is controlled varying the energy of the electrons via a potentiostat.

Electrochemical processes can be separated into outer-sphere or inner-sphere processes. In outer-sphere processes, reactants do not interact chemically with the electrode material and tend to occur in the solvent, away from the electrode. It should be stated that the choice of electrode is still a relevant factor in these systems. For example, when investigating the behaviour of the outer-sphere redox couple $[Fe(CN)_6]^{3-}/[Fe(CN)_6]^{4-}$ with Pt and Au electrodes, Gonzáles *et al*.[169] observed slight variations in the diffusion coefficients of the redox couple. It was also reported however, that the cyclic voltammograms and current density and potential (*j*–*E*) plots were almost identical regardless of electrode. The same study investigated another redox couple that is known to be an inner layer process, namely the Fe(III)/Fe(II) couple in sulfuric acid. The associated cyclic voltammograms and *j*–*E* plots displayed significant variation across both electrodes clearly displayed the great influence of the electrode material.[169] Paraphrasing from White *et al.*[170], inner-sphere reactions tend to involve the electrode as a chemical component of the reacting system, featuring the adsorption of reactants and intermediates. This can be the direct adsorption of reactants, *i.e.*, the adsorption of N_2 for the eN_2RR, or the adsorption of a ligand in a metal complex, as in the case of the oxidation of $Cr(H_2O)_5^{2+}$ on a Hg electrode and in the presence of halide. Should the electrode be able to accelerate the kinetics involved in an electrochemical process without being chemically altered itself, then that electrode is an electrocatalyst. Such systems are the purview of heterogeneous electrocatalysis and are not trivial to model. Throughout this thesis only systems in aqueous electrolyte solutions have been considered, and electrocatalytic systems will be discusses in this context.

2.5.1 Computational Hydrogen Electrode Model

The computational hydrogen electrode (CHE) model, developed by Jónsson *et al*. in 2004,[147] is a very simple model to apply and serves as a solid foundation for approximating the role of the applied bias. This method is built upon the definition of the standard hydrogen electrode (SHE), which is shown below,

$$H^+_{(aq)} + e^-_{el} \rightleftharpoons \frac{1}{2} H_{2(g)} \tag{2.77}$$

This states that a solvated proton and an electron are, at standard conditions (298.15 K and 1 atm) and a pH of 0, in equilibrium with half a hydrogen molecule in the gas phase at 0 V relative to the standard hydrogen electrode (0 V_{SHE}). This is a very useful relationship when

considering the binding of common adsorbates in aqueous electrolytes, such as protons, hydroxyls, and oxygen ions. In the case of the adsorption of a proton, which occurs thusly,

$$H^+_{(aq)} + e^-_{el} + {}^* \rightleftharpoons {}^*H \tag{2.78}$$

In this equation, a proton from solution and an electron from the cathode combine, resulting in a H atom bound in an adsorption site, denoted by *.

Considering Eq. 2.77, we can equate the Gibbs energy of half of the hydrogen molecule to that of the proton electron pair, allowing us to compute the binding energies of the aforementioned common adsorbates on an electrode.

$$\Delta G_{nH,0V_{SHE}} = G_{nH} - \left(G_* + \frac{n}{2}G_{H_2}\right) \tag{2.79}$$

$$\Delta G_{nOH,0V_{SHE}} = G_{nOH} - \left(G_* + nG_{H_2O} - \frac{n}{2}G_{H_2}\right) \tag{2.80}$$

$$\Delta G_{nO,0V_{SHE}} = G_{nO} - \left(G_* + nG_{H_2O} - nG_{H_2}\right) \tag{2.81}$$

Where G_* refers to the clean electrode surface, G_{nH} is the energy of n H atoms bound to the surface, and G_{H_2} is the energy of the hydrogen molecule, and G_{H_2O} is the energy of the water molecule. It should be noted that water is used as a reference for oxygen and hydroxyl binding as opposed to molecular oxygen. This is due to the errors inherent with DFT, which struggles to calculate oxygen in its triplet ground state.[171] Regarding $\Delta G_{nH,0\,V_{SHE}}$, this energy describes the energy of a H atom bound to an electrode at 0 V_{SHE}, and so a correction must be made when applying an external potential.

$$G_{H^+ + e^-} = \frac{1}{2}G_{H_2} - eU_{SHE} \tag{2.82}$$

Applying an external bias only affects the energy of the electrons in the system, leaving the protons and dihydrogen unaffected. As such, combining Eq. 2.82 and Eqs. 2.79 – 2.81 provides the following equations.

$$\Delta G_{nH,SHE} = \Delta G_{nH,0V_{SHE}} + neU_{SHE} \tag{2.83}$$

$$\Delta G_{nOH,SHE} = \Delta G_{nOH,0V_{SHE}} - neU_{SHE} \tag{2.84}$$

$$\Delta G_{nO,SHE} = \Delta G_{nO,0V_{SHE}} - 2neU_{SHE} \tag{2.85}$$

Many electrochemical studies are performed at nonzero pH's, resulting in a variation from the strict definition of the SHE (Eq. 2.77). We can subsequently look at the relationship between the reversible hydrogen electrode (RHE) and the SHE to account for the pH. The potential of the RHE can be written as,

$$U_{RHE} = U_{SHE} - \frac{RT}{F}\ln\left(\frac{p_{H_2}}{(a_{H^+}^2)}\right) \tag{2.86}$$

Where R is the ideal gas constant, T is the absolute temperature, F is the Faraday constant, p_{H_2} is the partial pressure of H_2, and a_{H^+} refers to proton activity. At standard conditions, and using the definition of $\text{pH} = -\log(a_{H^+})$, we can rewrite Eq. 2.86 as,

$$U_{RHE} = U_{SHE} - 0.059 \times pH \tag{2.87}$$

As such, we can write the potential relative to the RHE, where the pH dependence disappears, or on the SHE scale where pH must be accounted for explicitly.[172]

The CHE is a simple but very influential model, effectively dominating the field of theoretical heterogeneous electrocatalysis. There are several drawbacks however, namely the fact that the applied potential is accounted for by a correction applied *a posteriori*. This means that the number of the electrons remains constant throughout a reaction pathway, i.e., calculations are done at a constant charge rather than at a constant potential. Consequently, they may not be representative of a system with an increased/decreased number of electrons. Additionally, the value of this correction is determined by the number of proton coupled electron transfers (PCETs) to the system. As such, this model does not correctly represent processes wherein the number of electrons remains constant, i.e., reorganisations and evaluations of TS structures, assuming that the potential has a constant effect.

2.5.2 Pourbaix Diagrams

When modelling electrocatalytic reactions, it is important to consider the resting state of the catalyst prior to its introduction to the substrate. While it is possible that a bare surface can be present under aqueous electrochemical conditions, it is also likely that reducing or oxidising potentials may result in surface coverages comprised of H, O, or OH groups, which can change the electronic structure of the electrocatalyst, or potentially block active sites.[173] Pourbaix diagrams are electrochemical phase diagrams, plotting the stability of

various species as functions of applied potential and pH. The Gibbs energy of the surface terminations with different concentrations of hydrogen, oxygen and hydroxyl ions can be plotted as a function of the potential. Subsequently, using the relationship between RHE and SHE described in Eq. 2.86 in tandem with Eqs. 2.83 to 2.85, we can plot the most stable surface coverage at various potential and pH values.

2.5.3 Grand Canonical DFT for Electrocatalysis

As mentioned before, the electrochemical bias is applied *a posteriori* in the framework of the CHE. Additionally, DFT is typically performed with a fixed number of electrons, N_e, whereas real electrochemical systems may fluctuate N_e to maintain a constant electrochemical potential of electrons, $\tilde{\mu}_e$, which affects the electrode potential. An absolute electrode potential can be determined through the work functions of the surface slab.[174]

$$\Phi = \phi_{vac} - \varepsilon_F \tag{2.88}$$

The work function, Φ, is the difference between the electrostatic potential in the vacuum, ϕ_{vac}, in units of eV, and the Fermi level ε_F. The Fermi level refers to the energy the highest occupied band in the surface slab. The work function is defined as the energy required to move an electron from the top of the valence band to a point in the vacuum. In a real system, the electrochemical potential of an electron in a vacuum is equal to zero.[170] The plane wave DFT code used throughout this thesis, however, sets the average potential of the simulation cell to be zero. Consequently, the potential of the vacuum has a nonzero value.

The calculated work function can be referenced to the work function of the SHE, Φ_{SHE}, which, with respect to vacuum, is approximately equal to 4.44 ± 0.02 eV according to Trasatti, allowing us to obtain a potential relative to the SHE.[175]

$$U_{SHE} = \frac{\Phi - \Phi_{\mathrm{SHE}}}{e} \tag{2.89}$$

The challenge lies in tuning the calculated work function to reach a target potential. The Fermi level, or the electrochemical potential, can be altered by increasing or decreasing the numbers of electrons, N_e, in the system. Algorithms that adjust N_e to match a target chemical potential during the SCF loop exist, however this feature is not implemented in the Vienna *Ab Initio* Simulation Package (VASP) software, nor is it implemented in the VASPsol implicit solvation package. This engenders the adjustment of N_e between

successive SCF loops via the Atomic Simulation Environment (ASE) as done by Jónsson *et al*.[176]

$$N_e(i+1) = N_e(i) - a \cdot \left[\Phi(i) - \Phi_{target}\right] \tag{2.90}$$

Where $N_e(i)$ and $\Phi(i)$ refers to the number of electrons and the work function at step i. Additionally, a has a value of 1.0 V^{-1} and is used to keep units consistent. This method converges the system to a target work function which relates to a desired electrode potential as defined in Eq. 2.89. These methods warrant the use of an implicit solvation model, in this case VASPsol, for two principal reasons.[139,140] Firstly, the potential in the vacuum must be shifted to the value of the potential in the bulk electrolyte region. Secondly, VASPsol provides a counter charge present in the electrolyte via the linearized Poisson-Boltzmann distribution allowing for the simulation cell to be charge neutral.

The energy of intermediates calculated at the same potential cannot be compared due their different values of N_e. Instead, their energies must be corrected to the grand canonical free energy, Ω, to allow for a direct comparison. The grand canonical free energy of a reaction intermediate can be calculated as follows.

$$\Omega = G + \varepsilon_F(N_e^{FS} - N_e^{IS}) \tag{2.91}$$

Where ε_F refers to the Fermi level, N_e^{FS} is the number of electrons corresponding to a target potential, N_e^{IS} refers to the number of electrons in the respective charge neutral system, and G refers to the free energy of the system. Effectively, the free energy of the system is corrected by the cost or gain of removing or adding electrons.

Chapter 3 Objectives

The focus of this thesis is ammonia, studying sustainable processes for both its synthesis and decomposition via periodic DFT calculations. The synthesis of ammonia is investigated by modelling the reduction of non-conventional substrates, namely cyanide, by electrocatalytic means. Ammonia decomposition is explored in collaboration with the experimental group of Prof. Jorge Gascon in the King Abdullah University of Science and Technology (KAUST), through photothermal catalysis. Both processes are investigated with the circular economy in mind, of which, as I'm sure has been gathered, I am an avid supporter of. In the following subsections, I will discuss the aims of the following chapters while also providing a motivation for their studying.

3.1 The Electrochemical Reduction of Cyanide on a Ni Cathode for Ammonia Synthesis.

The electrochemical synthesis of ammonia from nitrogen occupies a large space in research, and rightly so. The eN_2RR promises to feed an ever-increasing global population in a sustainable way. However, this process suffers from the challenging activation of atmospheric nitrogen as well as competition with the HER. To address the first issue, we have proposed to reduce a different substrate to synthesise ammonia, cyanide. Taking the reduction of nitrates as a proof of concept, previously fixed nitrogen substrates should be utilised and recycled wherever is possible. However, the reduction of cyanide species is more or less, a new frontier in research, with a handful of associated studies. Therefore, the knowledge of this reaction mechanism had to be built from the ground up. We began our investigations taking inspiration from experimental works with the intent to:

- Elucidate the mechanism for the reduction of cyanide species.
- Establish why methylamine is the major product for the cyanide reduction reaction and how to favour the formation of methane and ammonia.
- Investigate and compare reduction reaction pathways where hydrogen is sourced from the electrolyte and the surface coverage.

3.2 Solvent Models for the Electrochemical Reduction of Cyanide

Based on the prior study of the reduction of cyanide, it was noted that several intermediates where physisorbed to the surface. Additionally, the TS associated with one of the investigated pathways was entirely unrealistic, involving the formation of a three-membered ring with a triple bond. Consequently, an investigation into the role of the aqueous environment was performed, with the aim to:

- Determine an alternative route for the reduction of cyanide by surface coverage sourced hydrogen via a water assisted transfer.
- Apply implicit solvation models and compare them to vacuum phase calculations.
- Apply explicit solvent models and investigate the kinetics associated with the reduction of cyanide.
- Investigate the effect of the electrochemical applied bias via GC-DFT on the electrochemical reduction of cyanide, comparing potentials of 0.0 V_{SHE} with more reducing potentials.

3.3 The Photothermal Decomposition of Ammonia on MOF derived Iron Materials

At this stage of the thesis, we turn away from ammonia synthesis and electrocatalysis, to ammonia decomposition and photothermal catalysis. Ammonia has been heralded as one of the more promising avenues of hydrogen storage, with cheap and effective decomposition catalysts being one of the limiting technologies. It is also envisioned as a short-term solution or action that can be implemented immediately to alleviate the climate crisis. As stated previously, this project was done in collaboration with Prof. Gascon in KAUST and is focused upon an iron MOF-derived material for which drastically different reaction rates as well as lower onset temperatures were found when the decomposition reaction was performed with and without light, although the exact role of light was unknown. We approached this project with the following goals in mind:

- Construct surface slab models that describe the MOF-derived active catalyst.
- Elucidate the ammonia decomposition reaction mechanism on these surfaces.

- Examine the role of light via the inclusion of either an electron or a hole.
- Investigate the kinetics of the rate determining steps for these systems.
- Rationalise the thermodynamic and kinetic data of the proposed ammonia decomposition mechanism with the experimental observations.

Chapter 4 The Electrochemical Reduction of Cyanide on a Ni Cathode for Ammonia Synthesis.

4.1 Introduction

The Haber-Bosch process is undoubtedly one of the most important and well-studied processes of the last 100 years. Yet, despite over a century of optimisation, little has changed regarding the intensive conditions required by industry. As the source of over 90% of the ammonia used today, the Haber-Bosch process contributes 400 Mt of CO_2 equivalents to greenhouse gas emissions and demands *ca.* 2% of the global annual energy supply.[177] This cost stems from the use of high temperatures and pressures (*ca.* 500 °C and 200 atm), as well as the dependence on hydrogen gas obtained via steam reforming of hydrocarbons.

The above factors have driven the need to produce ammonia sustainably, something that nature has achieved under ambient conditions via the enzyme nitrogenase, although with a high energy cost.[178,179] Hence, much effort has gone into attempting to mimic nature, leading to the eN_2RR. This reaction is accompanied by many obstacles,[180–182] one of which is the daunting task of activating the rather inert N_2 molecule, which has a BDE of *ca.* 941 kJ mol^{-1}.[11] Another major hurdle associated to eN_2RR is the competing HER, which typically requires applied potentials that are less negative[15] than those for the eN_2RR, leading to a low faradaic efficiency towards eN_2RR.

Circumventing some of the challenges associated with the eN_2RR may be done by exchanging N_2 for a similar substrate, such as cyanide. The electrochemical cyanide reduction reaction (eCNRR) offers several advantages over the eN_2RR. Firstly, in contrast to N_2, cyanide is a less inert species, being polar and having a dipole moment; the BDE of cyanide is also considerably smaller in comparison to nitrogen (BDE_{CN} = 842.7 kJ mol^{-1} vs BDE_{N2} = 941 kJ mol^{-1}).[183] Secondly, the eCNRR not only produces NH_3, but CH_4 as well, an important fuel and chemical feedstock. Finally, cyanide is produced naturally in many micro- and macroorganisms, for example, in the seeds of many types of fruit and roots.[184,185] Hence, the production of two essential chemical

feedstocks, easier activation, and natural and non-edible sources of reactants, renders the eCNRR as a very attractive prospect for the sustainable production of ammonia.

Despite all the advantages, there are only a handful of studies on the eCNRR reported in the literature. Most notable is the seminal work by Peters *et al.*[81] regarding the reduction of an iron complex bearing a tris(phosphine)silyl ligand, *i.e.* [SiP^{iPr}_3]Fe(CN), which was shown to stoichiometrically produce CH_4 and NH_3 in moderate overall yields of *ca.* 41%. However, this process required an excess of a very strong acid and sacrificial reductant, as well as very low temperatures of –78 °C. In addition to this process, the heterogeneous eCNRR was reported by Augustynski *et al.*[82] at several metal cathodes (*i.e.* Ni, Cu, Pd, Pt, Au and Fe) in a sodium perchlorate solution at pH = 6 and under an applied bias. Interestingly, Ni was found to outperform all the other metals, even precious metals like Pd and Pt, which displayed little to no activity. Moreover, in most cases, the $6e^-$ eCNRR (Eq. 4.1) was found to coexist with a dominant $4e^-$ process (Eq. 4.2) that produced methylamine, CH_3NH_2. In the case of Ni, a maximum faradaic efficiency of 71.7% towards eCNRR was measured at an applied potential of –1.4 V_{SHE}, of which 50.9% went towards the $4e^-$ process and 20.8% towards CH_4 and NH_3.

$$HCN + 6H^+ + 6e^- \rightarrow CH_4 + NH_3 \;\; E^0 = +0.331\ V_{SHE} \tag{4.1}$$

$$HCN + 4H^+ + 4e^- \rightarrow CH_3NH_2 \;\; E^O = +0.238\ V_{SHE} \tag{4.2}$$

Herein, we report a thorough computational study of the eCNRR reaction mechanism at a nickel cathode, present an account of the $4e^-$ and $6e^-$ processes reported in the literature, and provide a rationale for the prevalence of CH_3NH_2 in the products.[186] With this knowledge, we identify the key elementary steps which need to be tuned to increase the selectivity towards the $6e^-$ process, producing CH_4 and NH_3. Furthermore, we explore an alternative eCNRR pathway whereby intermediates are hydrogenated by the hydrogens from the surface, avoiding the formation of CH_3NH_2. The challenges associated with this pathway and the strategies to overcome these are also presented.

4.2 Computational Methods

Plane wave density functional theory (DFT) calculations reported in this work were performed using projector-augmented wave (PAW) pseudopotentials[187] and the Bayesian

error estimation functional with van der Waals correlation (BEEF-vdW),[109] as implemented in the Vienna *Ab Initio* Simulation Package (VASP) code, version 5.4.4.[188,189]

Optimisation of the equilibrium lattice constant for the Ni bulk was performed using the full face-centered cubic (*fcc*) unit cell and a planewave energy cutoff of 700 eV. Reciprocal space sampling was tested using several Γ-centered *k*-point grids of size 3×3×3, 5×5×5, 7×7×7, 9×9×9, 11×11×11, and 13×13×13 with convergence to 1 meV/atom achieved for an 11×11×11 grid. This resulted in an equilibrium lattice constant of 3.525 Å, which is within 0.04% of the experimental value.[190] The computed magnetic moment for Ni was 0.69 μ_B, in very good agreement with previous theoretical and experimental findings.[191,192]

A four-layer Ni(111) slab with a *p*(2×2) periodicity and a Γ-centered *k*-point grid of 5×5×1 was modelled to assess the resting state of the Ni catalyst under the experimental conditions reported by Augustynski *et al*.[82] For reactivity studies, this slab was extended to a *p*(3×3) periodicity to avoid interactions between the reaction intermediates in periodic cells. All surface calculations were performed with a vacuum spacing of at least 15 Å in the direction perpendicular to the surface. For both the *p*(2×2) and *p*(3×3) slabs, the two bottom layers were fixed to their bulk positions, whereas the remaining two layers were allowed to relax. Dipole corrections in the direction perpendicular to the surface were included in all calculations.

Geometry optimisations were carried out with an energy convergence criterion for the electronic steps of 10^{-6} eV and a force criterion of 0.01 eV/Å^2 for the ionic steps. The first order Methfessel-Paxton method with a value of 0.2 eV was used as the width of smearing. The adsorption energies, ΔE_{ads}, of the eCNRR intermediates were determined as:

$$\Delta E_{ads} = E_{surf+ads} - E_{surf} - E_{ads} \tag{4.3}$$

Where $E_{surf+ads}$ is the energy of the slab with the adsorbate species, E_{surf} is the energy of the clean slab, and E_{ads} is the energy of the adsorbate in the gas phase.

Gibbs energy corrections were then computed at the ambient conditions, *i.e.* 298 K and 1 atm, by means of the Thermochemistry module in the Atomic Simulation Environment (ASE) package.[193] These corrections include the zero point energy, entropy and heat capacity contributions. Vibrational contributions for the adsorbates comprising the surface

coverage prior to mechanistic studies, were calculated via the harmonic approximation and by fixing all metal atoms while allowing the adsorbates to vibrate. For the calculation of Gibbs energy corrections regarding the eCNRR, all metal atoms and hydrogens comprising the surface coverage established prior to cyanide adsorption were fixed, whereas the cyanide intermediate was vibrated. The computational hydrogen electrode was applied to describe the proton-coupled electron transfer (PCET) steps involved in the eCNRR. The calculated theoretical overpotential is defined as the minimum applied bias needed to make every step downhill in energy.[147] The reported Gibbs adsorption energies, ΔG_{ads}, were calculated taking into account the applied potential by means of the following equation:

$$\Delta G_{ads} = \Delta E_{ads} + \Delta G_{corr} + neU \tag{4.4}$$

Where n is the number of electrons involved in the elementary step, ΔG_{corr} is the Gibbs energy corrections for the adsorbate species, U is the applied potential, and e is the charge of the electron. All potentials reported in this work are referenced to the reversible hydrogen electrode (RHE), unless otherwise stated.

Transition states were located with the nudged elastic band (NEB) and the climbing image nudged elastic band (CI-NEB) methods, using at least five images along the reaction coordinate. Vibrational frequency calculations were conducted to confirm the nature of the stationary points, obtaining only one imaginary frequency in the optimised transition state structures and none for the reaction intermediates.

4.3 Results and Discussion

4.3.2 Determining the Resting State of the Catalyst

Before conducting any mechanistic studies for electrocatalytic processes, it is important to ascertain the resting state of the catalyst under reaction conditions to ensure we model a system that is representative of experiments. With this aim, a coverage analysis on a Ni(111) surface with a $p(2\times2)$ periodicity was performed to assess the state of the Ni cathode used by Augustynski *et al.*[82] The first step of this process consisted of modelling the adsorption of species present in an aqueous electrolyte (*i.e.* H, O, and OH) in all possible sites to establish their preferred adsorption.

Table 4.1. Evaluation of the most stable adsorption site on a Ni(111) surface for each species present in aqueous solution.

	ΔE_H (eV)	ΔE_O (eV)	ΔE_{OH} (eV)
top	0.20	1.91	–0.04
bridge	–0.36	0.07	–0.17
hcp	–0.34	0.16	–0.06
fcc	–0.36	0.07	–0.17

The adsorption trend obtained, from most stable to least stable, was *fcc* > *hcp* > *top*. In all cases, adsorption on the *bridge* sites resulted in the adsorbate relaxing to the *fcc* site.

Surfaces containing different concentrations of adsorbates in their most stable positions were then modelled, and their Gibbs energies computed. As the bound H and O atoms were observed to not interact with each other, the assumption was made that the thermodynamics corrections of an adsorbate in a specific active site could be scaled to account for all similar active sites for that atom. In this case, for the *p*(2×2) surface with a surface coverage comprised of 4 H atoms in the *fcc* sites and 4 H atoms in the *hcp* sites, the thermodynamic corrections, $G_{corr,sys}$, were calculated via the following equation:

$$G_{corr,sys} = \left(G_{corr,H_{fcc}} \times 4\right) + \left(G_{corr,H_{hcp}} \times 4\right) \quad (4.5)$$

Where $G_{corr,H}$ refers to the thermodynamic corrections of a single H atom in a specific active site. In this way, the coverage analysis for non-interacting adsorbates was done. The corrections for adsorbates that did interact with each other (*i.e.,* the OH groups), however, were not scaled and calculated explicitly. In hindsight, this assumption should not have been taken without rigorous testing, especially when we consider that the H_{fcc} and H_{hcp} distance is only equal to 1.44 Å.

Table 4.2. Relative energies of coverages with and without thermodynamic corrections (ΔE and ΔG, respectively) for H, O, and OH groups on a Ni (111) $p(2\times2)$ surface slab. All energies are supplied in eV. θ refers to the fraction of active sites on the surface that are occupied by an adsorbate, for example, $\theta = 0.5$ refers to a surface wherein two of four active sites are occupied.

θ	ΔE_H	ΔG_H	ΔE_O	ΔG_O	ΔE_{OH}	ΔG_{OH}
0.25	–0.36	–0.17	0.07	0.00	–0.17	0.03
0.5	–0.71	–0.32	1.22	1.09	0.06	0.55
0.75	–1.03	–0.45	3.25	3.07	0.71	1.36
1.0	–1.37	–0.60	6.57	6.32	–	–
1.25	–0.11	0.85	–	–		
1.5	0.14	1.29				
1.75	1.55	2.89				
2.0	3.15	4.68				

Referring to the above table, the coverage analysis was continued for H, O, and OH groups until either, the binding of adsorbates became unstable as in the case of the H and O atoms, or if the formation and desorption of products occurs. This latter case is observed for the OH groups, as the formation of water is observed. The calculation of these surface coverages allowed for the construction of the below Pourbaix diagram (Figure 4.1) as described in Section 2.5.2 and employing Eqs. 2.83 – 2.85 and Eq. 2.87.

Referring to the experimental work of Augustynski *et al.*,[82] the equilibrium potential of the $6e^-$ CNRR pathway (Eq. 4.1) is +0.331 V_{SHE}, which under the slightly acidic experimental conditions of pH 6 is shifted to –0.02 V_{SHE}. However, the authors note that the cathodic current begins not at this potential, but rather at more negative potentials of –0.8 V_{SHE}. Consequently, these conditions were chosen as the operating conditions of the electrochemical reaction. As shown in the Pourbaix diagram (Figure 4.1, inset), this corresponds to a Ni(111) surface where all the *fcc* sites are occupied by H atoms.

The Pourbaix diagram shown in Figure 4.1 prompts a tentative rationalization of the faradaic efficiencies reported for a Ni cathode at three different potentials, *i.e.*, 70.7% (–1.4 V_{SHE}), 17.7% (–1.2 V_{SHE}), and 44.1% (–1.7 V_{SHE}).[82] From these values, we first note that the peak efficiency observed at –1.4 V_{SHE} refers to a point in the middle of the Pourbaix

region that represents a coverage of 6 H atoms. The potential of –1.7 V_{SHE}, where an intermediate faradaic efficiency of 44.1% is observed, describes a region on the Pourbaix diagram that is closer to the border between two regions on the Pourbaix. At these border regions the adsorption and desorption of hydrogen is in equilibrium ($\Delta G_H = 0$ eV), making them optimal for HER.

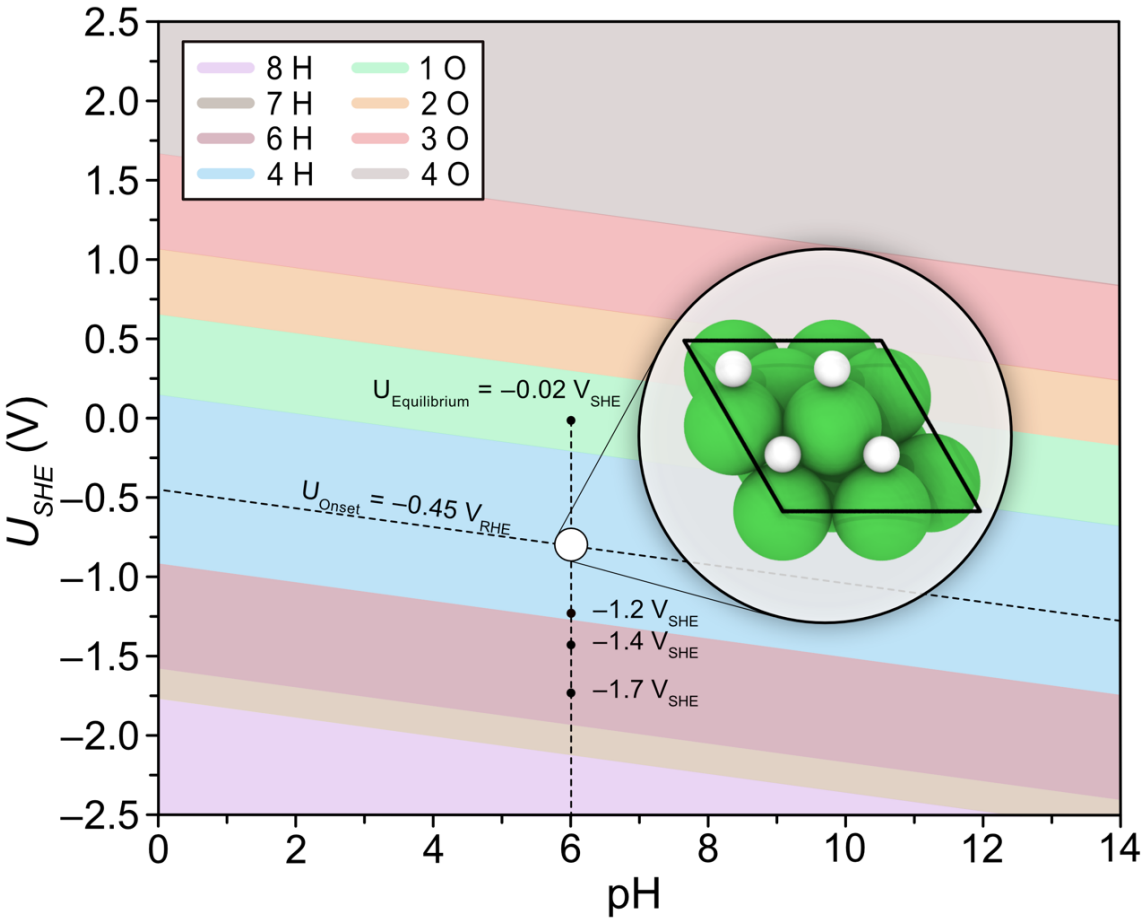

Figure 4.1. Pourbaix diagram obtained for a p(2×2)-Ni(111) surface at 298 K and 1 atm. The small circle highlights the experimental onset potential of –0.45 V_{RHE} (–0.8 V_{SHE} at pH 6),[82] while the inset illustrates the resting state of the catalyst under these conditions. The equilibrium potential of –0.02 V_{SHE} at pH 6 is also labelled, as are the experimentally investigated potentials of –1.2 V_{SHE}, –1.4 V_{SHE}, and –1.7 V_{SHE}. Reproduced from Ref. 186 with permission from the Royal Society of Chemistry.

Consequently, the faradaic efficiency towards the eCNRR drops at these potentials due to the severe competition with the HER. The third potential sampled on Ni, –1.2 V_{SHE} results in a poor faradaic efficiency of 17.7%. However, referring to Figure 4.1 reveals that this potential results in a coverage of 4 H atoms on the *p*(2×2)-Ni(111) surface. It should be

noted that this area of the Pourbaix diagram is close to the border between two regions and thus, within the framework of this model, competes with the HER. At –1.4 V_{SHE}, where the faradaic efficiency is recorded to be 70.7 %, the surface coverage is one where there are 6 H atoms on the Ni surface. However, at –1.7 V_{SHE} the surface coverage is found to be the same, yet the faradaic efficiency drops by 26.6%, implying that some energetic barrier for a competing process is surmounted. This discussion should be taken with caution as several approximations have been made. In addition to the approximation made in the calculation of the thermodynamic corrections, we have also assumed only a *p*(2×2) slab. Choosing a larger slab would allow for a larger range of surface coverages to be sampled and would potentially reveal more regions on the Pourbaix diagram. As well as that, we have only considered 'pure' surface coverages, *i.e.*, only those coverages with a single type of adsorbate.

4.3.3 Modelling the Electrochemical Reduction of Cyanide

After assessing the resting state of the Ni(111) surface under eCNRR conditions, we set out to explore the underlying reaction mechanism. With this aim, we extended the 4H-covered surface predicted in Figure 4.1 to a *p*(3x3) slab to avoid or minimise the interaction between periodic intermediates. On this surface, we subsequently introduced the NaCN species used in experiments by adsorbing the CN^- moiety onto the remaining surface sites, through both the N and C atoms. Our calculations found that binding through the C atom on to the *top* site was preferred. The Na^+ cation was also adsorbed onto the top of the slab and placed as far from the bound cyanide as possible so as to minimise any interactions between them. The purpose of the Na^+ cation is to provide a charge separation in the system so that we are modelling the reduction of the cyanide ion, and not the radical form. This charge separation was confirmed via Bader charge analysis, with the Na^+ having a charge of q = +0.86 and the *CN^- group having a net charge of q = –0.65. Subsequently, the full reduction reaction pathway was modelled.

Similarly to the eN_2RR, the adsorbed *CN can be hydrogenated through a distal or alternating pathway,[194] although hybrid pathways have also been reported.[42] The former pathway involves one end of the *CN being hydrogenated completely to NH_3, before C is hydrogenated to CH_4, whereas in the latter both C and N atoms are hydrogenated in turns.[195] In order to elucidate the lowest energy pathway, the first hydrogenation of *CN via a PCET

step was modelled with the H binding to either C or N atoms. Out of the two subsequent intermediates, the one with the lowest energy was then selected for further hydrogenation. In this manner, the lowest energy pathway, depicted in Figure 4.2, was mapped out.

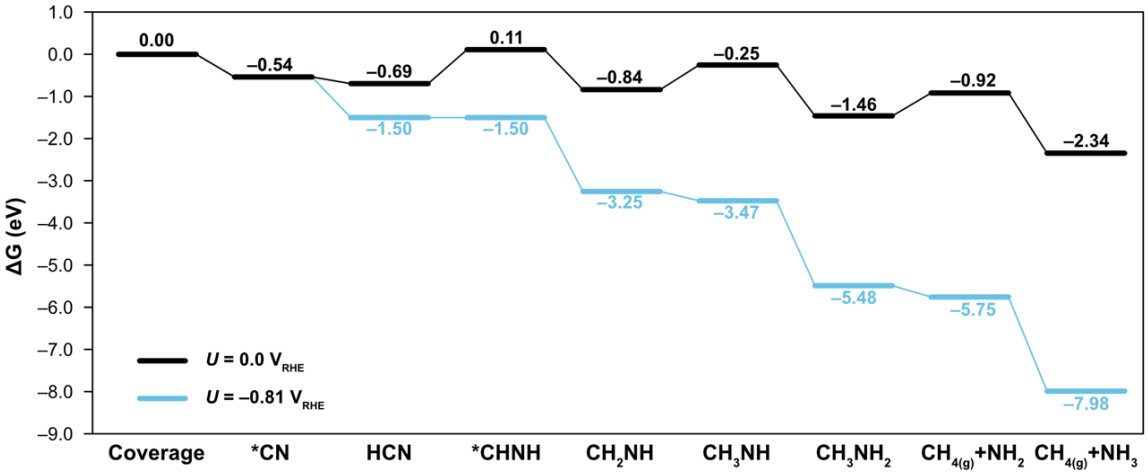

Figure 4.2. Gibbs energy pathway for the reduction of NaCN with the Na cation on top of the slab. The black trace refers to the energies calculated in the absence of an applied electrochemical potential, and the blue trace refers to the black trace, shifted by –0.81 V_{RHE} according to the CHE model, so as to render the entire pathway (thermodynamically) downhill. The prefix (*) refers to intermediates that are bound to the surface.

The reduction of NaCN on the Ni cathode begins, from the binding of cyanide on a *top* site, with the formation of HCN, which is physisorbed onto the surface. This intermediate is hydrogenated to give *CHNH, the formation of which is endergonic by 0.81 eV relative to HCN. Subsequently, this intermediate is reduced to formaldimine, CH_2NH, which could be expected to hydrolyse to ammonia, however the corresponding aldehyde, formaldehyde, is found to be absent in experiment.[82] Further hydrogenation leads to the formation of methylamine, and eventually methane and ammonia. The briefness of this discussion should provide a clue into the fact that this mechanism was not deemed to be feasible. Examination of the geometries revealed the interference of Na^+ with the cyanide intermediates. An example is given in Figure 4.3 depicting CH_3NH, wherein the N atom is coordinated to the cation via its lone pair. Not only does this "tether" the adsorbate,

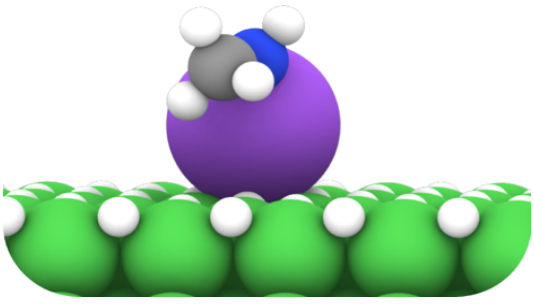

Figure 4.3. CH_3NH intermediate bound to the Na cation on the Ni(111) surface.

preventing desorption, but it also inhibits further hydrogenation of the nitrogen atom. As such, it was deemed that Na^+ interfered with the reduction of cyanide, and so this pathway was disregarded. However, the inclusion of Na provides a charge separation that allows for cyanide to be treated as an anion, as opposed to a radical species and is therefore essential. Consequently, the Na^+ cation was bound to the underside of the slab as shown below in Figure 4.4.

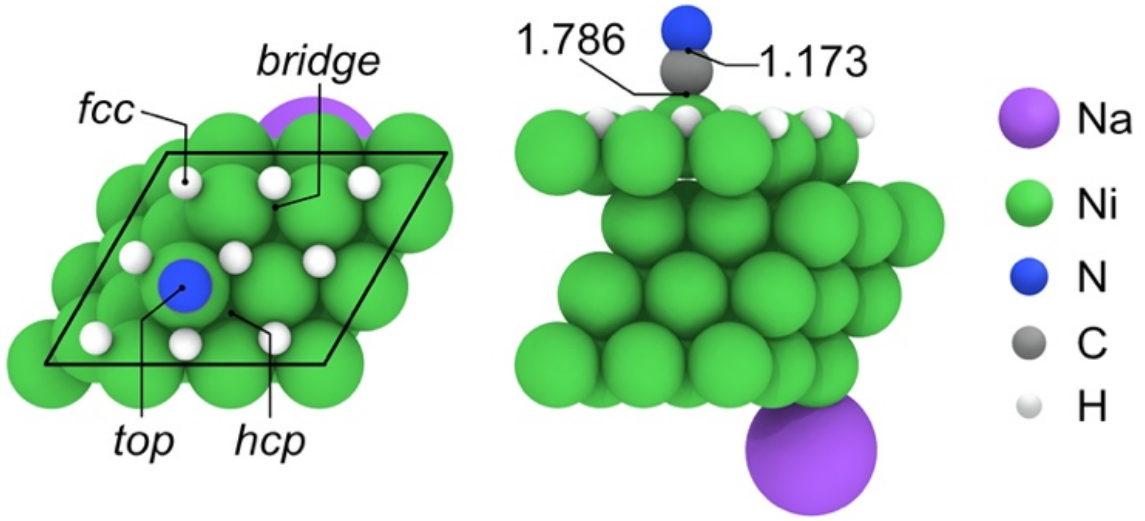

Figure 4.4. Top (left) and side (right) view representations of the p(3x3)-Ni(111) surface slab with the CN– adsorbed on top of the surface and the Na+ cation adsorbed underneath. Reproduced from Ref. 186 with permission from the Royal Society of Chemistry.

Dipole corrections were applied to the system to deal with the resulting dipole as CN^- was bound to the top of the slab. Again, we sampled the remaining surface sites finding a preferential binding for the *top* site via the C atom with a relative energy of +0.59 eV as well as Ni – C and C – N bond lengths of 1.876 and 1.173 Å, respectively. The charge separation and ionic character of the adsorbates was confirmed via Bader charge analysis, with values of q = +0.70 and –0.39 associated with the Na^+ and the CN^- groups accordingly.

The lowest energy eCNRR mechanism shown in Figure 4.5 follows an alternating pathway, wherein the first PCET step leads to the hydrogenation of the C atom to form a stable HCN species with an energy of –0.44 eV. In this intermediate, the C≡N bond is reduced by 0.015 Å and is oriented parallel to the surface at a distance of 3.926 Å. From this point, the subsequent hydrogenation results in the formation of the *CHNH species in an endergonic process by 0.79 eV. This intermediate remains chemisorbed onto the Ni surface (Ni–C:

1.973 Å) and features an increase in the C–N bond length to 1.245 Å, characteristic of a C=N double bond.

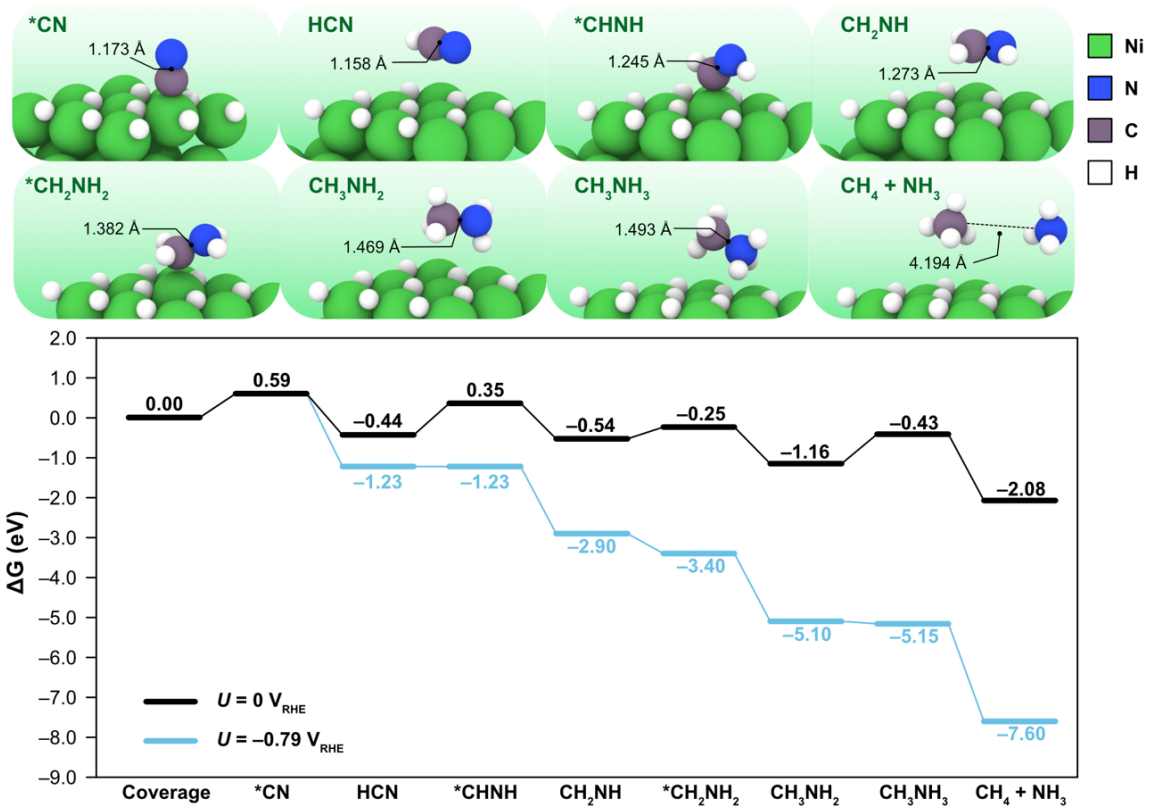

Figure 4.5. Lowest Gibbs energy diagram for the eCNRR on Ni(111) to produce CH_4 and NH_3, calculated at 0 V_{RHE} (black trace) and at –0.79 V_{RHE}, the applied potential required to make every intermediate thermodynamically downhill (blue trace). Optimised structures of the eCNRR intermediates along with the relevant bond distances (in Å) are also shown. Reproduced from Ref. 186 with permission from the Royal Society of Chemistry.

Further hydrogenation of the *CHNH intermediate reduces the surface back to its initial state with the cleavage of the Ni–C bond. In this step, the hydrogenation of the C atom is favored yielding $*CH_2NH$, which lies –0.54 eV below the starting reactants. This imine displays a typical C=N bond distance of 1.273 Å and is aligned parallel to the slab allowing for van der Waals interaction with the surface as for the HCN intermediate. In the following PCET step, the H atom binds preferentially to nitrogen, causing the reduction of the C=N bond to afford $*CH_2NH_2$. Interestingly, the distance between the C and Ni atoms (*i.e.* 2.164 Å) in this intermediate is somewhat too large to be considered a single bond, although there is a definite interaction between the C and the surface, as confirmed by the charge density difference analysis depicted in Figure 4.6. The C–N bond distance of 1.382 Å is also

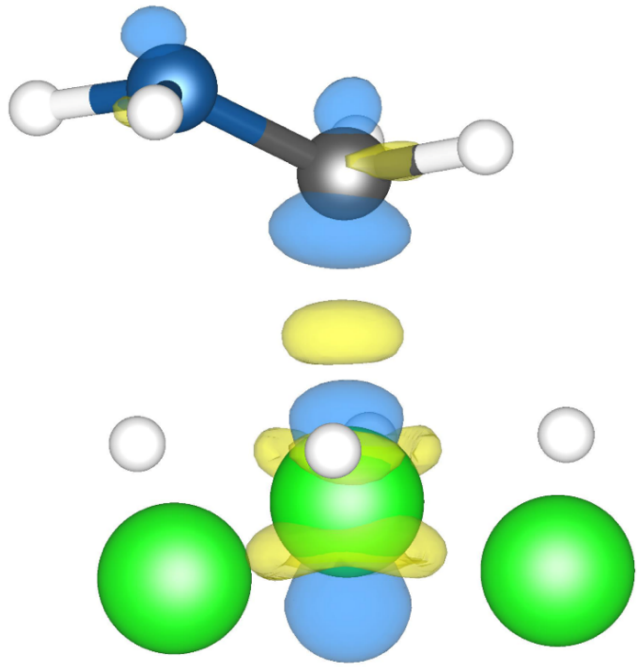

Figure 4.6 Charge density difference analysis for the *CH_2NH_2 intermediate with an isosurface level of 0.008 a.u. Yellow (blue) isosurfaces indicate areas of electron accumulation (depletion). Reproduced from Ref. 186 with permission from the Royal Society of Chemistry.

noteworthy, being too large for a double bond, yet too short to represent a single bond. In fact, this value is reminiscent of the partial double bonds found in pyridine, which would explain the interaction between the C atom and the surface.

This pattern of intermediates changing from chemisorbed to physisorbed states repeats throughout the entire mechanism in conjunction with the alternating binding of hydrogen to carbon and nitrogen. This occurred up until the hydrogenation of *CH_2NH_2 to methylamine, CH_3NH_2, which features a C–N bond length of 1.469 Å, characteristic of a single bond. Notably, the formation of this intermediate is overall exergonic by *ca.* 1.15 eV, and results in the desorption of CH_3NH_2 at a distance of 4.199 Å from the surface. This observation, the end result of the 4e$^-$ eCNRR process, is in line with CH_3NH_2 being the major product (50.9%) in experiments.[82,196]

However, the 6e$^-$ products CH_4 and NH_3 were also detected experimentally in appreciable yields (20.8%), suggesting that CH_3NH_2 can be further hydrogenated when in close proximity to the electrode to form CH_3NH_3. The next intermediate has a relative Gibbs energy of –0.42 eV and is physisorbed at 3.024 Å from the surface. From this species, the ensuing and final PCET step affords a new C–H bond and the cleavage of the C–N bond. This results in CH_4 and NH_3 being desorbed from the surface as the products of the 6e$^-$ eCNRR process, in an overall exergonic reaction by 2.08 eV.

Examination of the Gibbs energies of this pathway with no applied potential reveals that the most energy demanding step is the formation of the *CHNH intermediate, *i.e.* the reduction of the C≡N triple bond, requiring an energy of 0.79 eV. As such, this step dictates

the theoretical overpotential required to make every step downhill in energy and is referred to as the potential determining step (PDS). Application of this overpotential leads to the blue energy pathway in Figure 4.5. We note that this theoretical potential of –0.79 V_{RHE} is in poor agreement with experiments, wherein the formation of CH_4 was observed to begin at *ca.* –0.8 V_{SHE} at pH 6, which is equivalent to –0.45 V_{RHE}.[82] Additionally, it must be stated that in the experimental work, NaCN was added to the electrolyte at a potential of *ca.* –0.7 V_{SHE} to avoid corrosion of the cathode.

One could also envision an alternative reduction pathway with the eCNRR intermediates being directly hydrogenated using the surface adsorbed H atoms as another hydrogen source. Subsequently, after every hydrogenation step by the surface coverage, we model the regeneration of the initial coverage by the electrolyte. The rationale for this is that H_2 dissociative chemisorption on Ni(111) is highly exergonic and kinetically very fast,[197] and therefore, this is expected to occur before hydrogenation.

To explore this possibility, the same modelling strategy presented above was applied using H atoms from the surface as well as the electrolyte. The lowest energy eCNRR pathway obtained in this manner is depicted in Figure 4.7 below, along with the optimised structures of the eCNRR intermediates involved.

Surprisingly, the initial hydrogenation of *CN via surface hydrogen is very different to that by the electrolyte, as taking a H from the surface creates a vacant *fcc* site. This allows for the C atom to move and occupy this very stable *fcc* position, favoring the hydrogenation of the N atom. The resulting intermediate, *CNH, has a *C–N bond length characteristic of an imine (*i.e.* 1.231 Å), whereas the corresponding structure in the electrolyte pathway, HCN, is clearly a nitrile (*i.e.* 1.158 Å). In addition, the bonds formed between C and the Ni surface atoms in the intermediate *CNH ranged from 1.941 to 1.984 Å, while HCN was physisorbed at 3.926 Å from the surface.

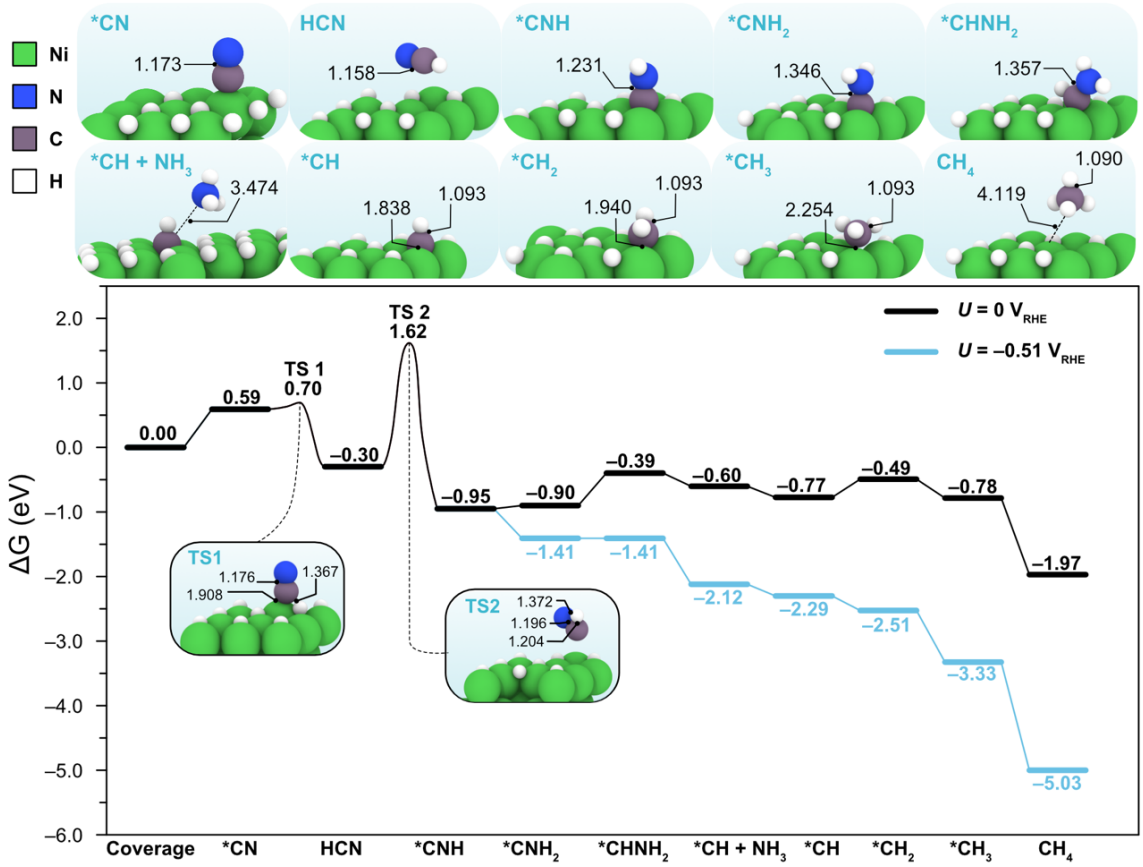

Figure 4.7. Lowest Gibbs energy diagram for the eCNRR on Ni(111) to produce CH_4 and NH_3 using both the surface coverage and the electrolyte as the source of hydrogen atoms, calculated at 0 V_{SHE} (black trace) and at the potential, –0.51 V_{RHE}, required to render every intermediate downhill in energy (blue trace). Optimised structures of the eCNRR intermediates along with the relevant bond distances (in Å) are also shown. Reproduced from Ref. 186 with permission from the Royal Society of Chemistry.

It is also very important to note that the formation of *CNH involves a chemical step and not electrochemical. As such, in the framework of the CHE, this hydrogenation is not affected by the applied potential and the energy of this species is fixed to –0.95 eV. NEB calculations aimed to elucidate the energy barrier associated with this chemical step, revealed that this process occurs in two separate steps. The first one corresponds to the hydrogenation of *CN to HCN via the transition state **TS1** with a relative energy barrier of only 0.11 eV (Figure 4.7). Due to the relative exergonicity of this process (*i.e.* by 0.89 eV), the C–N bond length in **TS1** is very similar to that of *CN (1.176 vs 1.173 Å). From HCN, the second chemical step involves the migration of the H atom from C to N at the same time that C shifts towards the vacant *fcc* site. This migration occurs via **TS2**, which requires an energy barrier of 1.62 eV, yet has an effective barrier of 1.92 eV. Notably, this value is

much higher than the barrier associated with TS1 and the typical barriers reported for PCET steps (*i.e.* 0.2-0.3 eV).[198] Hence, we conclude that HCN may form via hydrogenation of *CN by either the electrolyte or the surface coverage, while *CNH is unlikely to form at room temperature. This value of 1.92 eV is similar to values reported for the HCN-HNC isomerization reported in the absence of a catalyst, implying that the Ni surface is not actively participating in the current model.[199] Despite this, the formation of this intermediate is very desirable for several reasons which we outline below.

This *CNH intermediate is 0.65 and 1.30 eV more stable than HCN and the subsequent *CHNH intermediate respectively. Should **TS2** be overcome, calculations predict that further hydrogenation of *CNH occurs again at the N atom as C is coordinatively saturated due to occupying the *fcc* site, as well as being bound to nitrogen (Figure 4.7). The formation of $*CNH_2$ is accompanied by an increase in the C–N bond length by 0.115 Å, resembling a partial double bond. This is also associated with a decrease in Ni–C bond lengths to a range of 1.849–1.903 Å. It is important to emphasize that this pathway is obtained by modelling the hydrogenation of cyanide by H atoms obtained from either the surface coverage or from the electrolyte. Should H atoms be sourced from the *fcc* sites of the Ni slab, the vacancies left behind will be occupied by H atoms acquired from the electrolyte by virtue of the applied reducing potential. Any intermediate in Figure 4.7 obtained by reduction via surface hydrogen is displayed with the hydrogen vacancy regenerated by this potential. As the vacancy is regenerated by the electrolyte, this PCET regeneration of the coverage allows the mechanism to be shifted by an applied potential. With this in mind, the formation of $*CNH_2$ from *CNH is predicted to be almost thermoneutral.

The addition of the third hydrogen to $*CNH_2$, this time from the electrolyte, favored the binding to C, which shifts slightly out of its *fcc* site and closer to a *bridge* site, resulting in an increase in the Ni–C bond lengths with distances ranging from 1.994 to 2.538 Å. In addition, due to the structural reorganization required in this step, the formation of $*CHNH_2$ is predicted to be energetically uphill by 0.51 eV. From this intermediate, the next step of the eCNRR saw the dissociation of the C–N bond with NH_3 being formed in an exergonic process by 0.21 eV. In particular, this structure converged with NH_3 completely desorbed from the surface slab, whereas the C atom returned to the *fcc* site with a Ni–C bond length of 1.841 Å. The implications of this step are hugely significant as the production of

CH_3NH_2, experimentally the major product, is avoided via this alternative eCNRR pathway. After evolving NH_3, the *CH group left on the surface can be further hydrogenated by the coverage in a relatively flat energy landscape until $*CH_3$ is formed. Hydrogenation of this last intermediate leads to CH_4, releasing to the gas phase the second product of the $6e^-$ process in an overall highly exergonic process by *ca.* 2.0 eV.

According to Figure 4.7, once *CNH is formed, the most energy demanding step is the formation of $*CHNH_2$, leading to a predicted theoretical overpotential of –0.51 V_{RHE}. Notably, this value is 280 mV smaller than the overpotential predicted for the eCNRR via the electrolyte hydrogenation pathway and in much better agreement with the experimentally observed onset potential of –0.45 V_{RHE}. This alternative pathway is also hugely significant, being one where the production of the $4e^-$ product CH_3NH_2 is inhibited and the exclusive synthesis of CH_4 and NH_3 is obtained. Hence, we posit that excellent faradaic efficiencies toward the $6e^-$ products can be achieved provided the barrier associated with TS2 is reduced or circumvented. Considering the fact that the surface is not involved in the formation of TS2 we believe that solvent effects may be crucial in circumventing this barrier.

There are several strategies which could be employed to lower this barrier, including doping and the functionalization of the surface. Future work will focus on exploring these catalyst engineering strategies to ultimately impel the design of low-cost eCNRR electrocatalysts to enable the sustainable production of CH_4 and NH_3.

4.4 Conclusions

In this chapter, we have investigated for the first time the eCNRR mechanism on a Ni(111) surface for the ambient production of ammonia. Our computational studies establish the resting state of the Ni cathode under experimental conditions to be one where all surface *fcc* sites are occupied by H atoms. Using this resting state, we investigate the binding of NaCN on the cathode, finding that a *top* site is preferred. However, upon modelling the full reduction reaction pathway we find that the Na^+ biases the mechanism towards the hydrogenation of carbon. As such, to remove the effect of the cation, we model the eCNRR with the Na^+ bound underneath the slab, so as to maintain the ionic character of cyanide via charge separation. We find that the eCNRR, performed in this fashion and when the

electrolyte is the only source of hydrogen, follows an alternating pathway. This mechanism has an associated theoretical overpotential of –0.79 V_{RHE}, that is in poor agreement with experiments, yet offers an account of why the $4e^-$ process dominates experimentally. This is due to the desorption of CH_3NH_2 from the surface preventing further hydrogenation to the desired $6e^-$ products, CH_4 and NH_3. This finding is relevant as it provides a clear target for further research. Enhancement of the interaction between the surface and CH_3NH_2 would heavily tilt the ratio of products towards that of the $6e^-$ process.

We also report a new alternative reaction mechanism which circumvents the formation of the $4e^-$ eCNRR product, favouring the production of CH_4 and NH_3. This pathway involves the hydrogenation of cyanide with hydrogen atoms sourced from both the electrolyte and the surface under eCNRR conditions. While it is true that there is a substantial energy barrier associated with this pathway, the presence of such an obstacle does not retract from the hugely significant result, a mechanism with an associated theoretical overpotential 280 mV lower than that of the electrolyte hydrogenation pathway, that is in good agreement with the experimental onset potential. This pathway paves the way for 100 % faradaic efficiency towards the synthesis of CH_4 and NH_3. As with any catalytic reaction, improvements can be made and the eCNRR is no exception. Substitutional doping, metal alloying, catalyst nanostructuring, and electrolyte engineering are some of the numerous strategies which could be applied to overcome this limitation. Additionally, the role of the cation should be investigated, particularly if it is able to potentially decouple the formation of methane and ammonia.

Overall, these findings provide important insights into the unexplored eCNRR, which offers the possibility to produce two high value chemical feedstocks from an inexpensive reactant with a natural source, using a cheap and abundant metal catalyst at ambient conditions. While the eCNRR might not be able to replace the Haber-Bosch process currently, due to the ever-increasing global demand for fertilizers and the limited abundancy of cyanide naturally sourced, it could greatly contribute to reduce the carbon footprint associated with the ammonia production industry. We strongly believe that the eCNRR warrants more attention regarding industry and research and that these findings will set the stage for more creative approaches to feasible ammonia synthesis.

Chapter 5 Solvent Models for the Electrochemical Reduction of Cyanide

5.1 Introduction

Catalysis has served as the bedrock of most, if not all, of the luxuries available in modern society. Yet most catalytic processes rely on fossil fuels, and therefore are not sustainable. In light of the current climate crisis, it is evident that a shift to more renewable technologies is demanded, which has urged many studies on the electrocatalytic conversion of abundant constituents in the Earth's atmosphere (*e.g.* H_2O, CO_2, N_2) into chemical fuels and feedstocks (*e.g.* H_2, C_xH_y, $C_xH_yO_z$, and NH_3).[200,201] Although great strides have been made in this field of research, there are still many hurdles which need to be overcome.[202]

One of the main obstacles to the fundamental understanding of electrocatalytic processes is the accurate description of the solid-liquid interface.[203] From a computational perspective, there are two main approaches to address this issue, namely via explicit and implicit solvation models. The former describes the electrolyte by the direct inclusion of solvent molecules in the calculation, although there are several variants within the umbrella term of explicit solvation. For example, there are reports of systems modelled with a discrete number of water molecules,[204–206] an ice-like water layer,[150,156] or with the simulation cell completely filled with water molecules.[207] Regardless of the method adopted, the description of the electrolyte via explicit models is further complicated by the fact that the solid-liquid interface is dynamic; in other words, a vast number of configurations of the interface can exist. The need to capture this dynamic behaviour and account for the ensemble of configurations has engendered the use of ab initio molecular dynamics (AIMD), which have shown the structure of water near the metal surface at room temperature to be quite disordered.[153,208] While this explicit description of the electrode-electrolyte interface would theoretically provide a more accurate description of the properties of and interactions between both phases, there is the added caveat of increased computational expense.[139] For this reason, the ice-like water layer (also referred as water bilayer) has become a very popular model in density functional theory (DFT) studies to

approximate the aqueous electrolyte and assess the thermodynamics and kinetics of electrochemical processes.[145–150,209]

On the other hand, implicit solvation models serve to describe the electrolyte by encapsulating the solute in a continuum medium characterized by the dielectric constant of the bulk solvent.[210] Within this approach, the solvation energy is determined by the position of the solute without any explicit solvent molecules, thus significantly reducing the computational cost. However, implicit models do have some shortcomings, the most glaring of which is the neglect of site-specific interactions between the solute and solvent, such as hydrogen bonding.[137] Furthermore, the approach whereby the solute cavity is defined can vary wildly between methods and software packages. For example, some methods mimic the solvent environment by placing Gaussian distributed plane charges within a short distance from the surface,[211] while others apply a homogeneous background charge over the entire system.[212] The Poisson-Boltzmann description of the solid-liquid interface has also become increasingly popular,[139,140,213] and it has been applied to the modelling of a number of electrochemical processes, including the HER and CO_2 electroreduction.[176,214–218] They have also been employed as a vehicle for the inclusion of the electrochemical applied bias in an approach termed as grand canonical density functional theory (GC-DFT). In this approach, the number of electrons, N_e, in the system are varied so as to tweak the Fermi level of the electrode and alter the work function, thus introducing an electrode potential. As N_e is varied, the implicit solvent continuum responds by varying the concentration of counterions in the electrolyte, thus maintaining the neutrality of the system.[176,219] Several studies employing GC-DFT have found changes in binding mode, geometry, and activation energy, highlighting their significance when compared to traditional constant charge calculations.[176,214,220,221]

Hybrid solvation, or microsolvation models, serve as a compromise between purely implicit and explicit approaches. These methods involve pairing a dielectric continuum with a much smaller amount of explicit water molecules with the intent to account for the bulk electrolyte, as well as site specific interactions, with a reduced computational cost. However, choosing the number of explicit solvent molecules that must be included to the system has always been a matter of contention with this approach. Calle-Vallejo et al.[161] developed a novel and systematic method for the determination of the number of explicit

molecules by comparing adsorbate-solvent and solvent-solvent interactions. Giordano and Di Liberto[160] found that the inclusion of three explicit water molecules reported solvation energies close to that of the water bilayer model. Nevertheless, it should be noted that the addition of a discrete number of solvent molecules around an adsorbate is expected to be accompanied by an entropy penalty, which is often neglected in microsolvation methods.[162]

The influence of the solvent has also been investigated in the electrochemical reduction of dinitrogen (eN_2RR),[145,146] a process that holds promise as a greener alternative to the Haber-Bosch process for ammonia production, which currently consumes *ca.* 3-5% of global natural gas production and is directly responsible for over 450 Mt of CO_2 emissions per year.[177,222] However, the eN_2RR is not without its challenges, specifically the activation of dinitrogen and the competition with the HER. One promising strategy to circumvent the arduous activation of N_2, while contributing to the equilibrium of the nitrogen cycle, could be the electroreduction of fixed nitrogen sources such as NO_x and cyanide species.

Besides serving as a source of fixed nitrogen, cyanide is found in both nature and industry.[223,224] Furthermore, the electrochemical reduction of cyanide (eHCNRR) offers a sustainable synthetic route towards the production of not only ammonia but methane as well.

$$HCN + 6H^+ + 6e^- \rightarrow CH_4 + NH_3 \quad E^O = +0.331\, V_{SHE} \tag{5.1}$$

Being a polar molecule, cyanide is also much more amenable to activation, rendering this fixed form of nitrogen particularly desirable. Notwithstanding these advantages, the literature is surprisingly devoid of studies with a focus on the eHCNRR. One of the few experimental reports on this process is that by Augustynski et al.[82] who revealed that Ni drastically outperforms expensive noble metals such as Pd or Pt, achieving a faradaic efficiency of 71.7%. This efficiency, however, was split towards methylamine (CH_3NH_2) as the major product and NH_3/CH_4 as minor products. In the previous chapter, we reported a computational mechanistic study wherein we rationalized the predominance of CH_3NH_2 with the desorption of this species from the nickel cathode and posited that solvent effects may aid in stabilizing CH_3NH_2 on the surface.[186] Additionally, an alternative pathway that results in the decoupling of the formation of CH_4 and NH_3 was discovered, although it is hindered by a large TS associated with the isomerisation of HCN to CNH, which may be circumvented by the inclusion of the aqueous environment. We are also interested in the

effect that solvent interactions may have on the several physisorbed intermediates that have been observed in the reduction of cyanide.

In this chapter, we investigate the water assisted formation of *CNH, as well as present a detailed comparison of the eHCNRR mechanism across vacuum, implicit solvent, and explicit solvent phases.[225] Additionally, we investigate the effect of dynamically accounting for the applied electrochemical bias via grand canonical DFT calculations with the intent to compare them to calculations performed at a constant charge. These findings reveal the benefits for reducing cyanide under basic conditions, potentially advantaging the formation of methane and ammonia. Our comparison of solvation models reveals key differences between implicit and explicit approaches, particularly with the introduction of an explicit aqueous environment, wherein drastic effects regarding the stabilisation of physisorbed intermediates are observed, implying that implicit models may not be sufficient for a good description of surface reactivity. The addition of the applied bias when considering the reduction of cyanide is also quite revealing, displaying the independence of some intermediates to the applied bias, as well as substantial changes in the geometries of adsorbates.

5.2 Computational Methods

Spin polarized DFT calculations were performed via the Vienna ab initio simulation package (VASP, version 5.4.4)[189,226] using the Bayesian error estimation functional with van der Waals corrections.[109] Core electrons were described by means of projector augmented wave pseudopotentials,[187] while plane waves with a kinetic cutoff of 700 eV were used to represent the valence electrons.

The Ni cathode was modelled as a 4-layer Ni(111) slab of p(3×3) periodicity with a vacuum spacing of at least 15 Å between periodic images in the direction perpendicular to the surface. Dipole corrections along this direction were also included in surface slab calculations. Atoms in the bottom two layers of the slab were fixed to simulate the bulk metal, while atoms in the remaining top two layers, as well as any adsorbates, were allowed to fully relax.

A surface coverage of H atoms occupying all the *fcc* sites was taken to be the catalyst resting state under the experimental eHCNRR conditions (*i.e.* pH 6), as we reported elsewhere.[186]

Geometry optimisations were performed with convergence criteria of 10^{-6} eV and 0.01 eV/Å for the electronic and ionic steps, respectively. A smearing width of 0.2 eV was used within the first order Methfessel-Paxton method, while the Brillouin zone was sampled with a Γ-centered 5×5×1 k-point grid.

Vibrational frequencies for the adsorbate species were computed within the harmonic approximation, fixing all the metals, coverage atoms, and explicit water molecules to reduce computational cost. With this information, Gibbs energy corrections were computed using the thermochemistry module in the Atomic Simulation Environment (ASE) package[193] at ambient conditions, *i.e.* 298 K and 1 atm. These corrections include zero-point vibrational energy, entropy, and heat capacity contributions.

Proton-coupled electron transfer (PCET) steps in the eHCNRR mechanisms were modelled via the computational hydrogen electrode model,[147] and the Gibbs adsorption energies, ΔG_{ads}, were calculated as:

$$\Delta G_{ads} = G_{surf+ads} - G_{surf} - G_{ads} \tag{5.2}$$

where $G_{surf+ads}$ denotes the Gibbs energy of the slab with the adsorbate species, G_{surf} the energy of the slab in the resting state (all *fcc* sites covered with H atoms), and G_{ads} the Gibbs energy of the isolated adsorbate.

The influence of the applied bias was accounted for as follows:

$$\Delta G_{ads,RHE} = \Delta G_{ads} + neU \tag{5.3}$$

Where U is the applied potential referenced to the reversible hydrogen electrode (V_{RHE}), e the elemental charge of an electron, and n is the number of electrons involved in a reaction step. The predicted limiting potentials predicted in this work are defined as the minimum applied bias required to make each elementary step thermoneutral or downhill in energy.

For relevant reaction steps, transition state (TS) structures were located through the nudged elastic band (NEB)[227] and climbing image nudged elastic band (CI-NEB)[121] methods, using a total of 8 images along the reaction coordinate. The nature of these stationary points was confirmed through vibrational frequency analysis, displaying only one imaginary frequency related to the reaction coordinate of interest. Non-covalent interactions (NCIs) were calculated using the Critic2 software.[165,166] Critical points in the reduced density gradient were established between three fragments, namely the Ni slab, the adsorbed HCN

intermediate, and the explicit water bilayer. These critical points can be either attractive or repulsive.

Implicit solvent calculations were performed with the VASPsol[139,140] software using a dielectric constant of 78.4 and a Debye length of 3.0 Å. Default parameters were used to construct the solute cavity. Explicit solvent calculations were carried out by inclusion of a H-down water bilayer composed of six H-bonded waters, wherein every second molecule had a H atom pointing down towards the surface (Figure 5.2.a). The ice-like neutral water layer was optimised, followed by the addition of a H atom which led to a H_3O^+ cation in the water layer and an electron localized in the surface slab (Figure 5.2.b). This H_3O^+ cation essentially 'caps' a lone pair of an O atom, preventing the formation of a H-bond and consequently leading to the distortion of the water bilayer. Additionally, we note that explicit water molecules were disrupted from their ice-like structure during geometry relaxations upon the introduction of the eHCNRR intermediates in the simulation cell, as we discuss below. This water bilayer was protonated via the addition of an extra H atom, *i.e.* a proton and an electron. Bader charge and charge density difference analyses (Table 5.4. and Figure 5.2.) confirmed the separation of the proton and electron into the solvent molecules and surface slab, respectively. The first PCET with explicit solvent was modelled with the protonated water bilayer to allow for kinetic studies. Subsequent steps were calculated by sourcing the H atom from the bulk electrolyte (not the water bilayer).

The implicit solvation model employs the linearised Poisson-Boltzmann equation, which accounts for ionic effects as well as solvent effects. The explicit solvent model that we employ neglects these ionic effects, however. For the purposes of comparison, we have investigated whether ionic effects have a significant impact on the energies of intermediates in implicit solvent, with the results summarised in Table 5.1 below.

Table 5.1. Energies of eHCNRR intermediates for the electrolytic pathway in implicit solvent with only solvent effects (E_{solv}), and with both ionic and solvent effects ($E_{ion+solv}$). We also include the difference between these energies for the same intermediate in the rightmost column.

Intermediate	*E (solv) (eV)*	*E (ion + solv) (eV)*	*ΔE (eV)*
HCN	–172.5812	–172.5822	0.0003
**CHNH*	–175.8335	–175.8339	0.0004
CH_2NH	–180.6782	–180.6782	0.0001
$*CH_2NH_2$	–184.5642	–184.5642	0.0000
CH_3NH_2	–189.3626	–189.3628	0.0002
$CH_3NH_3^+$	–193.1619	–193.1593	–0.0026
$CH_4 + NH_3$	–198.0602	–198.0606	0.0004

We find that these effects are negligible, being present at most, in the third decimal. As such, any difference between these two solvent models is not due to the lack of ionic effects in explicit solvent.

We have also introduced the applied electrochemical bias to the eHCNRR, following the method outlined by Jónsson *et al.*[176], wherein the number of electrons in a system is adjusted between SCF loops by via ASE. All target potentials, U_{SHE}, are referred to the work function of the SHE, which is approximately equal to 4.44 ± 0.02 eV, as described in Section 2.5.3[175]

5.3 Results and Discussion

5.3.1 Water Assisted Hydrogen Transfer

In the previous chapter we investigated the reduction of cyanide via hydrogen sourced from the surface coverage. The kinetics of this process were investigated revealing two associated transition states. The first, **TS1**, is negligible, being only 0.11 eV more endergonic than *CN. This **TS1** is associated with the tilting of *CN towards a hydrogen atom as it leaves the *fcc* site. Subsequently, HCN is formed and physisorbed to the surface. **TS2** then occurs and refers to the isomerisation of HCN to CNH far from the surface. This **TS2** is very high in energy, effectively 1.92 eV, and serves as a significant hindrance to the formation of the much desired *CNH intermediate. This energy is reminiscent of reports

wherein the same process is performed in the absence of a catalyst.[199] As such, we believe that this **TS2** is wholly unrealistic and must be circumvented via solvent interactions. With this in mind, we investigated the kinetics involved in the formation of *CNH from *CN via surface hydrogen using a water molecule as an assistor, as seen below in Figure 5.1.

The water assisted hydrogenation of *CN to *CNH occurs in a few steps. The first step involves the diffusion of H from the *fcc* site to a nearby *hcp* site via a *bridge* site. As this occurs, *CN, bound to a *top* site begins to diffuse to the newly vacated *fcc* site. **TS*bridge*** refers to *H in a *bridge* site prior to the diffusion of *CN. The energy associated with this TS, however, is only 0.20 eV higher than the initial state. This value is slightly higher than literature values of *ca.* 0.13 eV for H diffusion from *hcp* to *fcc* via *bridge* sites.[228,229] It should be kept in mind however, that these studies in the reported literature involved a H coverage of θ = 0.25 in the absence of both water and *CN. The following intermediate, as seen in Figure 5.1, refers to *H optimised in the *hcp* site and *CN occupying the *fcc* site, although the various C–Ni bond lengths vary considerably (1.913, 2.173, 2.269 Å). The relative energy of this intermediate is 0.02 eV, and practically thermoneutral with that of the initial state, wherein *CN is on a *top* site and *H is in an *fcc* site.

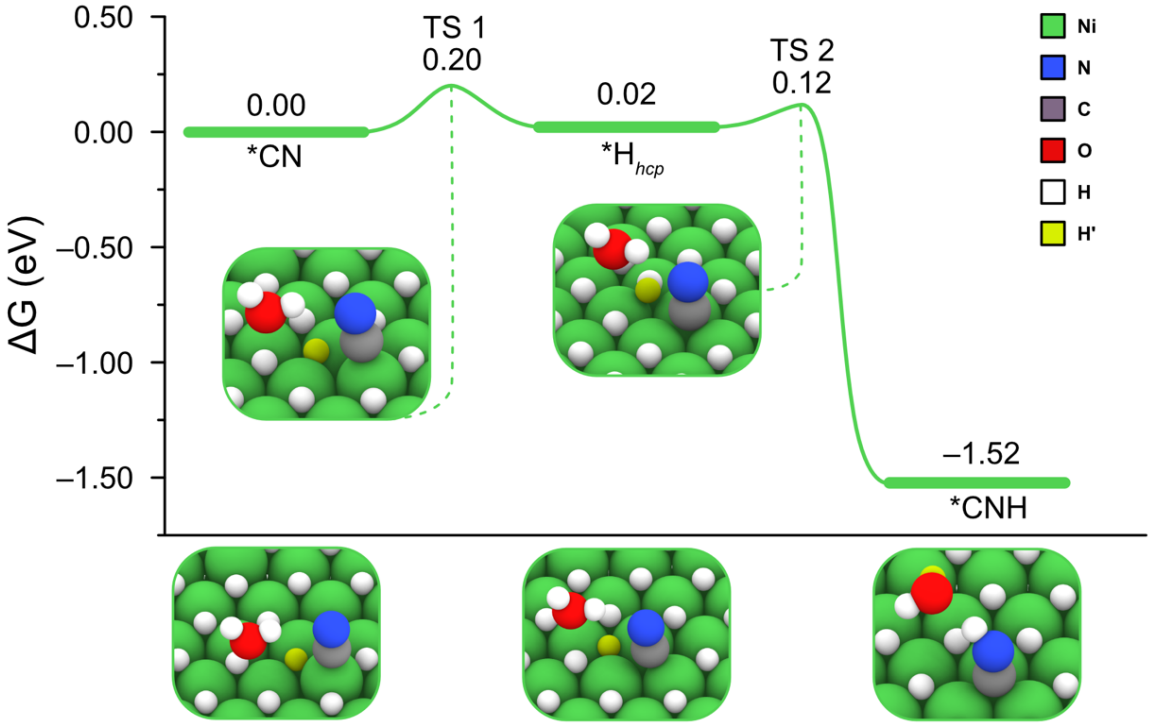

Figure 5.1. Kinetics involved with the formation of *CNH from *CN using hydrogen (labelled as H') sourced from the surface coverage and shuttled via a water molecule.

From this intermediate, labelled as $*H_{hcp}$, hydrogen is found to diffuse out of the *hcp* site, and towards a *bridge* site, which incidentally, is the TS. Subsequently, the incident H atom interacts with a nearby H atom in an *fcc* site, ($H_{hcp} - H_{fcc}$ = 0.841 Å), and moves to the *top* site. Once on the *top* site, H is taken up by the lone pair of water, as another H atom is shuttled to *CN via the OH···N hydrogen bond, forming *CNH. The associated TS, $\mathbf{TS}_{top}$ is very low in energy, only 0.12 eV less stable relative to the initial binding of *CN.

The energetic barrier for the hydrogenation of bound cyanide to adsorbed hydrogen isocyanide is greatly impacted by the assistance of water, from an effective barrier of 1.92 eV, to 0.2 eV. However, the pKa of HCN is *ca.* 9.2,[230] meaning that its deprotonated form, CN^-, exists only under basic conditions, where there is less water present in solution to facilitate the hydrogenation to chemisorbed hydrogen isocyanide. The inclusion of a protic solvent to the system at basic conditions could potentially favour the formation of methane and ammonia even further.

It should be kept in mind that while these results are in agreement with experiments performed by Augustynski *et al.*[82], who reported that increasing the pH of the system resulted in a decrease in the ratio between the $4e^-$ and $6e^-$ products, accounting for the solvent in this manner serves as only a proof of concept for this process. One water molecule cannot approximate the role of the aqueous environment, particularly one when there is an electrochemical double layer present. As such we were motivated to investigate and compare several solvation models for the reduction of cyanide.

5.3.2 Comparison of HCN Binding Modes

In the experimental CNRR study performed by Augustynski *et al.*,[82] cyanide was introduced into the system in the form of NaCN (0.036 M) at pH 6. Under these conditions, and given the pKa of cyanide in water (pKa = 9.2),[230] the predominant species in aqueous solution is expected to be HCN; as such, this was the substrate chosen for our computational investigations. However, to conduct such a comparison, the protonated water bilayer had to be constructed. This was done by first including six H-bonded water molecules. Both H-up and H-down configurations (as illustrated in Figure 2.5) were optimised, with the H-up configuration being more stable on the hydrogen covered nickel slab, albeit slightly (Table 5.2), which is in quantitative agreement with prior theoretical studies regarding clean transition metal surfaces.[154,155]

Table 5.2. Absolute energies for neutral and protonated water layer, as well as energy differences between H-up and H-down configurations.

Water layer H Configuration	*E (eV)*	$E_{Up-Down}$ *(eV)*
H-up	–193.85	0.01
H-down	–193.84	
H-up (Protonated)	–196.75	–1.15
H-down (Protonated)	–197.90	

Both the H-up and H-down water layers were protonated by the inclusion of an extra hydrogen atom, converting one H_2O molecule to a H_3O^+ cation and an electron localised in the slab. Referring to Table 5.2, it was found that the protonation of the H-down water layer was drastically more stable than that of the H-up layer, and as such this system was chosen to represent the explicit solvent. The charge separation of the extra hydrogen atom was confirmed via both Bader charge (Table 5.4.) as well as charge density difference analysis (Figure 5.2), which reveal the localisation of a proton in the solvent layer, and an electron in the surface slab.

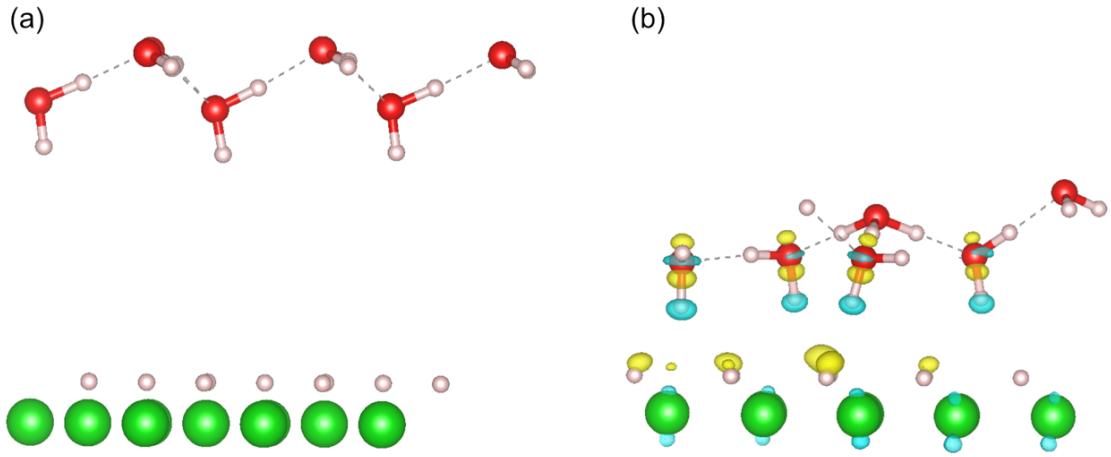

Figure 5.2. Charge density difference analysis, employing an isovalue of 0.0035 a.u., of the (a) neutral water bilayer composed of six H_2O molecules and (b) the protonated water bilayer, comprised of five H_2O molecules and one H_3O^+ above the cathode surface. Yellow (blue) isosurfaces represent an accumulation (depletion) of electron charge density. Reproduced from Ref. 225 with permission from the Royal Society of Chemistry.

Hence, we started by adsorbing the HCN molecule on a Ni(111) surface with H atoms occupying all the *fcc* sites, which is predicted to be the resting state under the experimental CNRR conditions.[186] In Figure 5.3, we compare the adsorption of HCN in vacuum and in the presence of implicit solvent, observing a negligible difference in the optimised geometries. In both cases, HCN remains physisorbed on the Ni(111) surface through its triple bond of 1.158 Å. The most notable difference between the two geometries is the distance of the HCN moiety from the surface, which in vacuum is 3.928 Å and in the presence of a dielectric continuum decreases to 3.904 Å. Both structures are also quite similar in terms of energetics, with HCN in vacuum being only 0.02 eV more stable than with implicit solvent.

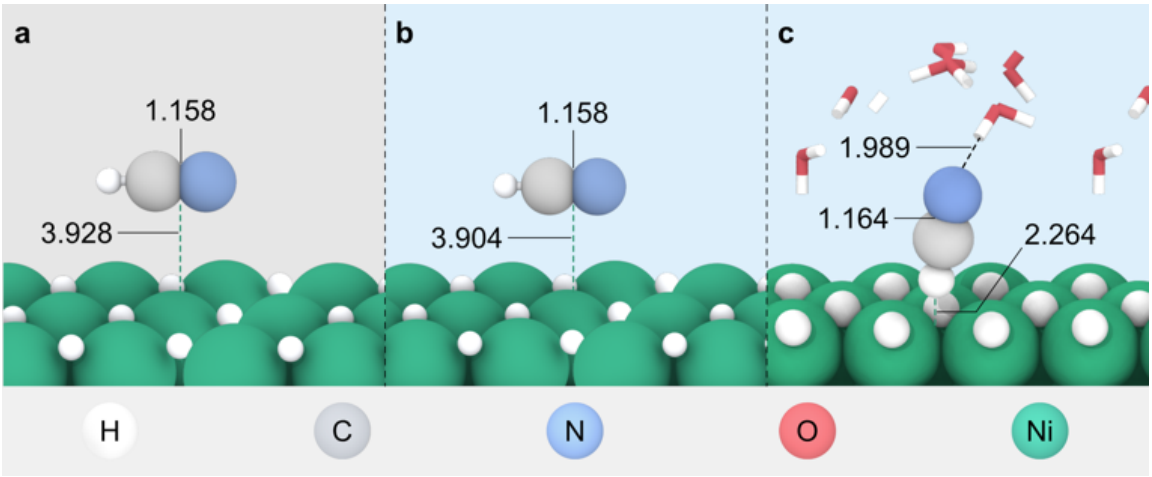

Figure 5.3. Optimised geometries of HCN adsorbed on the H-terminated Ni(111) slab in a) vacuum, b) implicit solvent, and c) the presence of an explicit water bilayer. Reproduced from Ref. 225 with permission from the Royal Society of Chemistry.

While the inclusion of implicit solvation does not seem to result in a radical change, treating the solvent explicitly has a much more dramatic effect on HCN adsorption. As seen in Figure 5.3c, the adsorption of HCN in the presence of explicit water molecules occurs almost perpendicular to the Ni(111) surface, instead of interacting via the C≡N triple bond. To rationalize this change in orientation, we carried out a detailed NCI analysis, the results of which are summarized below in Figure 5.4. This analysis reveals that the lone pair of the N atom establishes a trifurcated H-bond with three solvent water molecules (labelled as *a*) while simultaneously repelling a water directly above it due to the clashing with the O lone pair (labelled as *d*). The assembly of these H-bonds is the most obvious stabilizing effect;

however, it is worth noting that there are other relevant interactions, as we describe in detail below.

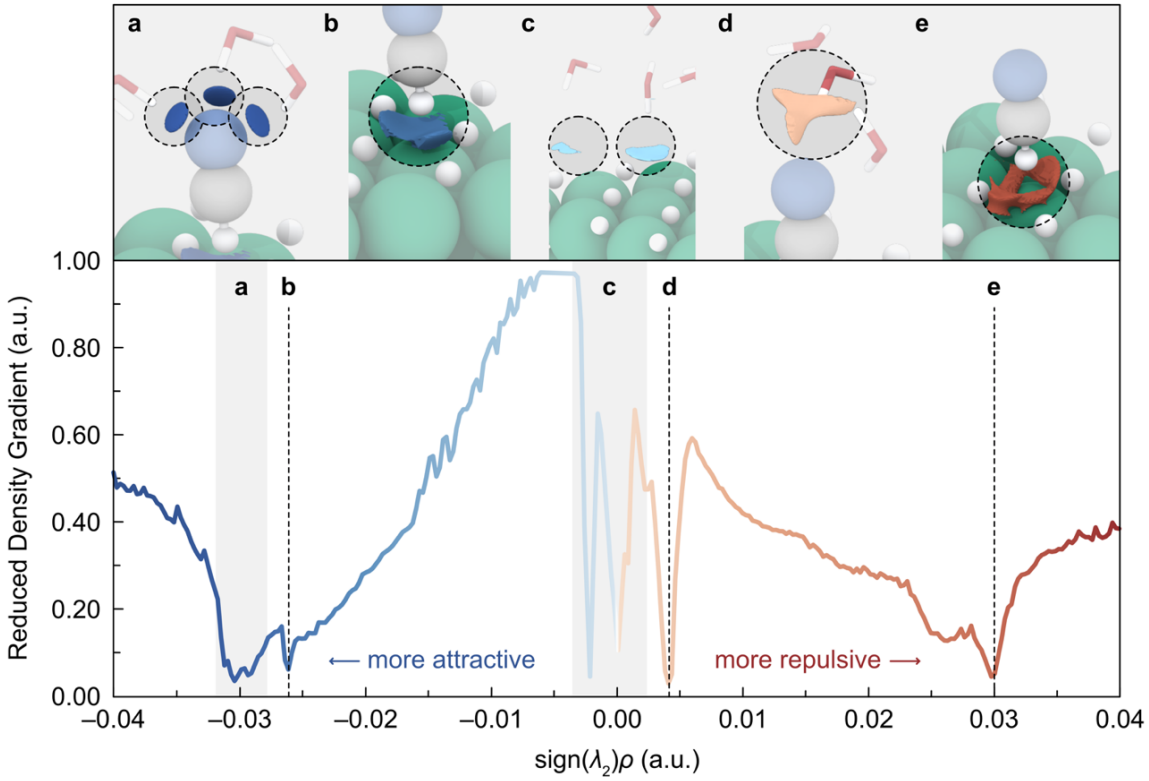

Figure 5.4. NCI analysis of the adsorbed HCN in the presence of an explicit aqueous environment. Top: Representation of the NCIs as isosurfaces (isovalue = 0.35 a.u.). Blue (red) isosurfaces denote attractive (repulsive) interactions. Colour code of atoms is the same used in Figure 5.3. Bottom: Semi-quantitative representation of the NCIs by plotting the reduced density gradient as a function of the electron density multiplied by the sign of the second eigenvalue of the Hessian matrix (sign(λ_2)ρ), which displays the NCIs as peaks. Colder (warmer) colours represent attractive (repulsive) interactions. Reproduced from Ref. 225 with permission from the Royal Society of Chemistry.

Figure 5.4 shows two additional interactions (labelled as *b* and *e*) involving the hydrogen coverage and the H atom of HCN. Bader charge analysis (Table 5.4) shed light on the nature of these interactions, revealing that hydrogens from the surface coverage exhibit a formal hydride character (q = –0.279), whereas the H atom of HCN has a positive charge (q = +0.313). Based on these findings, we attribute the attractive interaction (labelled as *b*) to the sigma bond donation from the surface Ni–H bonds to the H of the HCN, while the repulsive interaction (labelled as *e*) can be assigned to the electronic repulsion between the

surface H atoms and the H of HCN, as the H–H distances are in the range of 1.816–2.239 Å.

Upon discovering such a difference between the HCN binding modes, we modelled the full HCNRR pathway with implicit and explicit solvent and compared the energies and geometries obtained for the different reaction intermediates to those computed in vacuum.

5.3.3 Implicit Solvation Pathway

The HCNRR can occur via an alternating or distal mechanisms, wherein the C or N atom is reduced completely (*i.e.* forming CH_4 or NH_3) or in turns. Hence, to assess the lowest energy pathway in the presence of implicit water and in vacuum, we modelled the hydrogenation of either the N or C atoms in HCN and continued from the most stable intermediate. The results of this investigation are summarized in Figure 5.5, where we compare the lowest energy eHCNRR mechanisms in both phases, assuming that H atoms are sourced by the electrolyte via PCET steps. Both reaction pathways follow an alternating mechanism with the intermediates varying between physisorbed and chemisorbed binding modes. In particular, the first hydrogenation of HCN results in the formation of *CHNH (* denotes a chemisorbed species), which binds on a *top* site of the Ni(111) surface through the C atom. Furthermore, the calculated C–N bond lengths of *ca.* 1.245 Å in both vacuum and implicit solvent for the *CHNH intermediate are characteristic of a C=N double bond in imines, as expected. Yet, we observe a relative energy difference of +0.15 eV across both environments, which we attribute to the slight stabilization of HCN and the slightly larger destabilization of *CHNH with implicit solvent. Further hydrogenation of this intermediate results in the imine CH_2NH, which is found to be physisorbed through the C=N double bond. This CH_2NH species is also slightly more stable in vacuum by +0.10 eV and lies at 3.900 Å from the surface compared to 3.729 Å with implicit solvation.

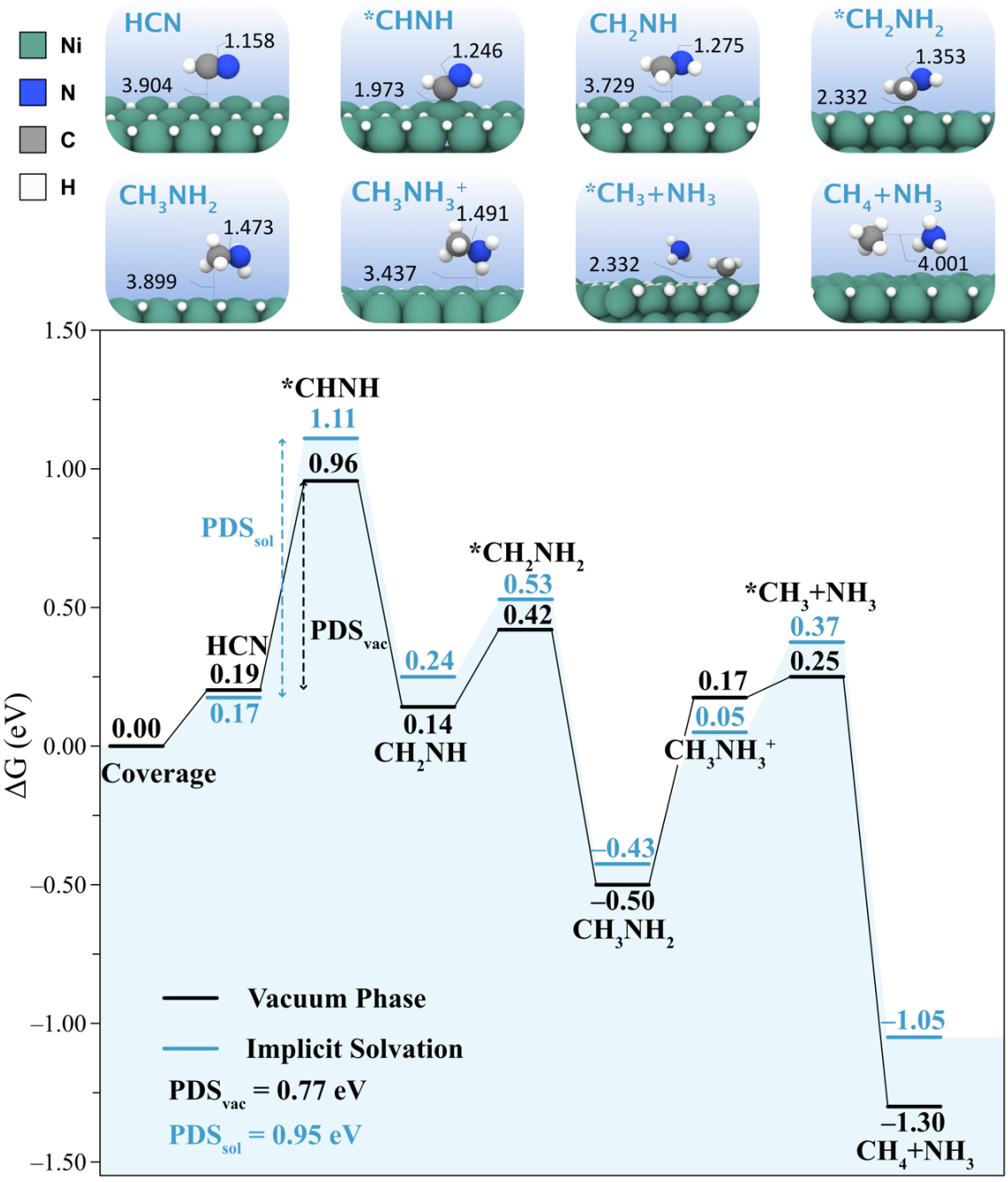

Figure 5.5. Gibbs energy profile for the eHCNRR on the resting state of Ni(111), modelled in vacuum (black) and implicit solvent (blue) at 0 V_{RHE}. H atoms are assumed to be sourced by the electrolyte via PCET steps. Labels of intermediates preceded by * denote chemisorbed species. The geometries of the reaction intermediates optimised with implicit solvent are shown as insets. The PDS for both the mechanism modelled in vacuum phase and implicit solvent are given as PDS_{vac} and PDS_{sol} respectively. Relevant bond lengths (in Å) are also provided.

From the CH_2NH intermediate, the next hydrogenation favours the reduction of the N atom to give $*CH_2NH_2$. As with *CHNH, this species is covalently bound to Ni with distances

of 2.174 and 2.332 Å in vacuum and implicit solvent, respectively. The formation of the Ni–C bond is further supported by charge density difference analysis shown below in Figure 5.6 and the elongated C–N distance from *ca.* 1.245 Å in *CHNH to 1.350 Å.

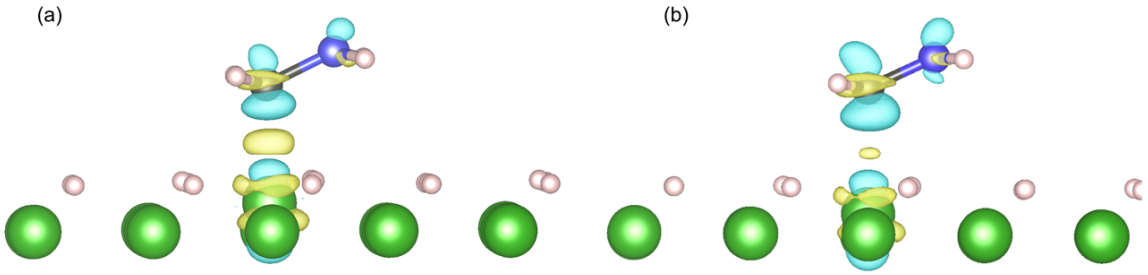

Figure 5.6. Representation of the charge density difference, using an isovalue of 0.006 a.u., calculated for the *CH_2NH_2 intermediate in the presence of (a) vacuum, and (b) a dielectric continuum. Yellow (blue) isosurfaces represent an accumulation (depletion) of electron charge density. Reproduced from Ref. 225 with permission from the Royal Society of Chemistry.

The accumulation of electron density between the C atom and the metal cathode implies, in the vacuum, the presence of a bonding interaction. The weaker interaction, represented by a lack of electron accumulation and the long C–Ni distance, between *CH_2NH_2 and the Ni surface in the implicit solvent could be rationalised by the formation of two distinct cavity systems.

Subsequent hydrogenation of *CH_2NH_2 favours the C atom to yield CH_3NH_2, wherein the C–N bond is reduced to a single bond with a distance of 1.473 Å. This bond undergoes a negligible elongation in the presence of the dielectric continuum, but the intermediate itself is brought closer to the surface by 0.141 Å. As we discussed in our previous study,[186] the desorption of CH_3NH_2 explains why this is the major product observed experimentally, which is unchanged by the presence of implicit solvent. Next, the reaction proceeds with the formation of $CH_3NH_3^+$, another interesting intermediate in that it is one of the two species reported in Figure 5.5 to be stabilized by the dielectric continuum. The Bader charge analysis of this species in implicit solvent reveals the separation of the transferred H atom into a proton and an electron found in the molecule and on the slab, respectively (q_{mol} = +0.845 and q_{slab} = –0.845). Hence, this intermediate is better described as methylammonium, $CH_3NH_3^+$. While we observe negligible differences across the C–N bond lengths and distances between this intermediate and the metal surface in both phases, the orientation of the H atoms around the C and N is markedly different. In particular, the

geometry of $CH_3NH_3^+$ with implicit solvation converges to a structure where one NH moiety points directly to a vacant *hcp* site on the surface, whereas the same intermediate in the vacuum phase does not.

The cleavage of the C–N bond in $CH_3NH_3^+$ gives rise to $*CH_3$ and physisorbed NH_3 in a process which is endergonic both in vacuum and implicit solvent. In particular, the reaction in vacuum is uphill by only +0.08 eV, whereas in a polarizable continuum is considerably higher, *i.e.* 0.32 eV. Once the methyl group is adsorbed on the surface, further hydrogenation results in CH_4 and NH_3, the experimentally observed minor products, in a process that is overall exergonic by –1.30 eV at 0 V_{RHE}. This energy exhibits a notable deviation from the overall gas phase reaction energy of –1.99 eV, which is derived from the standard redox potential of +0.331 V. The observed discrepancy arises because CH_4 and NH_3 are modelled in the 'solid state' rather than in their gaseous form. However, when calculating the reaction energy based on gas phase reactants and products, a value of –1.55 eV is obtained, reflecting inherent errors in DFT energies of gas phase species. To address these errors, we have applied gas phase corrections, summarised below in Table 5.3 following the method proposed by Calle-Vallejo *et al.*,[231] which bring the reaction energy to –2.06 eV, aligning closely with the experimental value. It is important to note that, for the sake of a fair comparison between phases, we have chosen not to correct these gas phase errors due to the absence of liquid phase error corrections.

Table 5.3. Overall rection energies calculated for the $4e^-$ and $6e^-$ eHCNRR, resulting in methylamine, and methane and ammonia, respectively. These energies are calculated as the difference in the gas phase energies of products and reactants, with the energy of a proton and electron pair being equated to half of the energy of gas phase H_2, according to the CHE, as described in Section 2.5.1. The columns labelled "*Org.*", "*Corr.*", and "*Exp.*", refer to the reaction energy calculated originally in the absence of gas phase corrections, the corrected reaction energy, and the experimental reaction energy respectively.

	Org. (eV)	*Corr. (eV)*	*Exp. (eV)*
$HCN + 4H^+ + 4e^- \rightarrow CH_3NH_2$	–0.62	–1.07	–0.95
$HCN + 6H^+ + 6e^- \rightarrow CH_4 + NH_3$	–1.55	–2.06	–1.99

Overall, we note there is only a slight change in the optimised geometries in vacuum and implicit solvent, with relatively small differences in terms of bond lengths, both within the

eHCNRR intermediates and between these and the Ni(111) surface. Yet, for most of the intermediates, the inclusion of implicit solvation results in an overall energy destabilization ranging between +0.02 and +0.25 eV, which is not surprising given the dipolar nature of HCN. The largest energetic difference between pathways, however, is seen in the final intermediate $CH_4 + NH_3$, which we attribute to the fact that this is the only step where three solute cavities are constructed, leading to a higher energy cost. While these differences in energy do not change the PDS's for both reaction environments, that is the formation of *CHNH, it does affect their absolute values, *i.e.* –0.77 and –0.94 V_{RHE} for the vacuum and implicit solvent phases, respectively. Based on all these findings, we conclude that there is a non-negligible effect of the implicit solvent, although it does not seem to provide a better description of the eHCNRR process or significantly affect the overall mechanism.

5.3.4 Explicit Solvation Pathway

We next investigated the influence of the solvent on the HCNRR from the perspective of an explicit solvation model. A summary of the lowest energy pathway obtained in these conditions is presented in Figure 5.7, along with the optimised structures of the intermediates involved and their relevant bond lengths. It should be noted that the energies of all intermediates calculated in the presence of explicit solvent molecules are referenced to the binding of HCN with explicit solvent, as opposed to the hydrogen covered Ni slab. This is due to the fact that, upon referencing the binding of HCN to the Ni surface and the protonated water layer, the Gibbs energy was calculated to be 5.17 eV. This unstable energy is due to the severe disruption of the water layer and the hydrogen bonding network by the HCN, which converges perpendicularly to the surface slab. However, as HCN is reduced by the Ni cathode in experiment, we assume that this unstable energy is an artifact of the solvation model chosen, and therefore we reference all energies calculated with explicit solvent to the binding of HCN, making direct comparison with energies calculated in the vacuum and implicit solvent phases uninformative.

We have also performed Bader charge analysis on the explicit solvent pathway due to the charge separation when constructing the protonated water bilayer.

Table 5.4. Summary of the Bader Charge analysis performed for the eHCNRR pathway calculated with explicit solvent molecules. The system has been broken down into three separate fragments, which are themselves all summations of charge. q_{mol} refers to the sum of charges of all atoms comprising the cyanide intermediate in question, q_{slab} contains the charges of the Ni atoms as we as the hydrogen coverage, and q_{water} comprises the charge of the explicit solvent molecules. It should be stated that while the magnitudes of the positive and negative charges may not equal 1 or –1 as expected, what is important is that these systems are charge neutral.

Intermediate	q_{mol}	q_{water}	q_{slab}
Water Bilayer	–	–0.002	+0.002
H^+ Water Bilayer	–	+0.726	–0.726
HCN	–0.112	+0.626	–0.514
CHNH	+0.195	+0.035	–0.230
CH_2N	–0.003	–0.070	+0.074
CH_2NH	+0.031	–0.040	–0.010
CH_2NH_2	+0.470	–0.142	–0.328
CH_3NH_2	+0.046	–0.090	+0.044
$CH_3NH_3^+$	+0.774	–0.125	–0.649
CH_4 + NH_3	+0.023	–0.040	+0.017

As previously mentioned, and shown in Figure 5.1, the adsorption of HCN converges to a geometry that is perpendicular to the surface. Hence, we expected that the solvent would transfer a proton to the N atom that is closer to and involved in several hydrogen bonds with the water bilayer. However, we found that the hydrogenation of the C atom to give CH_2N is instead favoured by –0.50 eV compared to the formation of CHNH. In light of this unforeseen result, we investigated the reaction kinetics for the direct formation of CH_2N from HCN, motivated by the large distance between the C and the H atoms in the water layer (C–HO = 2.742 Å), as well as the interaction and shorter distance between the N atom and the water bilayer (N–HO = 1.989 Å). This analysis revealed the presence of a TS structure (**TS1'**, Figure 5.7) with an energy barrier of +1.15 eV, wherein the proton that is transferred from the water bilayer to the C atom is located at 1.713 Å from its parent water molecule and 2.141 Å from the C. As such, this proton has a large distance to travel, which explains the high energy barrier associated with this step.

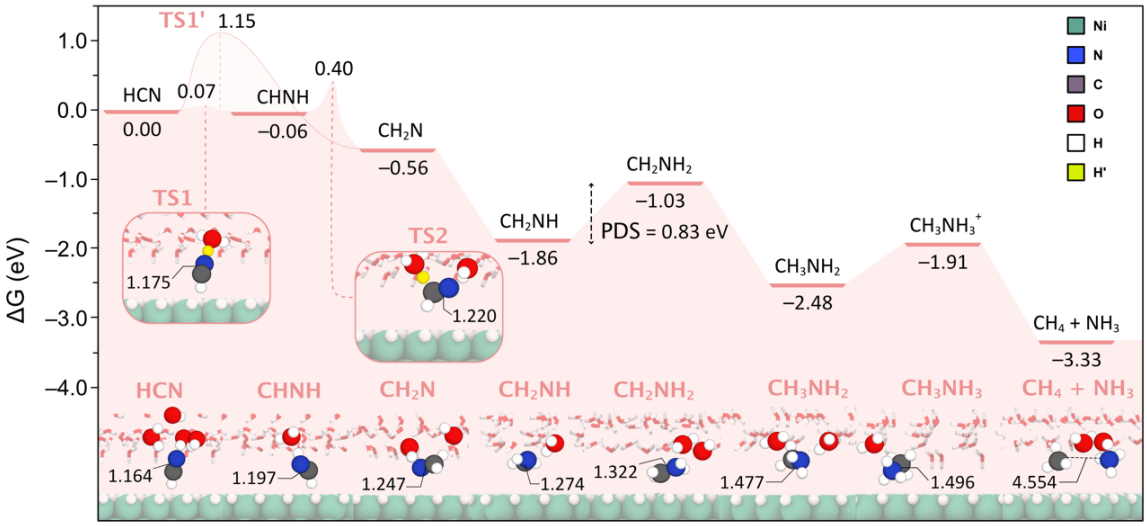

Figure 5.7. Gibbs energy profile for the eHCNRR on the resting state of Ni(111), modelled in explicit solvent at 0 V_{RHE}. Gibbs energies are calculated relative to the adsorbed HCN. In the first PCET step, the H atom is sourced by the protonated water bilayer to allow for kinetic studies. In subsequent steps, hydrogen is sourced by the bulk electrolyte (not the water bilayer). The geometries of the reaction intermediates and the two lowest energy TS structures optimised with explicit solvent are shown as insets. The hydrogen atoms of interest involved in these TS structures are denoted as H' in the legend. For the sake of clarity, the water molecules directly interacting with the eHCNRR intermediates are depicted with a ball-and-stick representation, while the rest of waters are shown as sticks. Relevant bond lengths (in Å) are also provided. Reproduced from Ref. 225 with permission from the Royal Society of Chemistry.

Alternatively, the hydrogenation of the N atom yields CHNH, an intermediate that is almost thermoneutral with HCN. In this case, given the proximity of the N atom to the water bilayer, the H transfer is kinetically favoured, as confirmed by the presence of a TS (**TS1**, Figure 5.7) with an energy barrier of only +0.07 eV. In this structure, we observe that the transferred proton is midway between the aqueous environment (O–H = 1.176 Å) and the N atom (N–H = 1.297 Å), and that the resulting CHNH tilts significantly towards the water bilayer with bond angles changing from 164.8° (N–C–Ni_{HCN}) to 119.1° (N–C–Ni_{CHNH}). We also note the appearance of a radical character on the C atom in CHNH with a magnetic moment of 0.206 μ_B. It should be noted that the excess proton appears to be shuttled to the CHNH completely as evident from the net charge of the water layer decreasing from +0.626 to +0.035. Additionally, the surface slab retains some of the extra electron (q_{slab} = –0.230), although not the electron in its entirety (see Table 5.4).

The subsequent formation of CH_2N from CHNH was found to occur via a Grotthuss-type mechanism,[232] whereby the proton on the N atom is returned to the water bilayer, via the NH···O hydrogen bond, and diffuses through the network of water molecules before it is shuttled to the C atom. This proton transfer to the C atom is facilitated by the tilting of CHNH towards the water layer, thereby reducing the distance that the proton must travel. Notably, the TS associated with this step (**TS2**, Figure 5.7) was found to have an energy barrier of +0.40 eV, which is significantly lower than the direct hydrogenation of the C atom to form CH_2N via **TS1'**. We also note that there is a radical character on the N atom in CH_2N as evident by a magnetic moment of 0.607 μ_B. Bader charge analysis on this intermediate (Table 5.4) indicates that both the surplus proton and the electron have been transferred to this species in this step. As such, we posit that the CHNH intermediate exists as a metastable state between the HCN and CH_2N intermediates.

Proceeding from the CH_2N structure, we found that the subsequent PCET step favours the hydrogenation of N to yield the imine CH_2NH. We also noted that the hydrogenation from this intermediate onwards follows the same alternating mechanism observed in vacuum and implicit solvent, depicted in Figure 5.3. However, of note is the highly exergonic hydrogenation of CH_2N to CH_2NH by –1.3 eV, presumably due to the quenching of the radical character on the N atom. It is also interesting to note that this appears to be the first intermediate that is oriented almost perfectly parallel to the surface (Ni–C = 4.176 Å), implying some weak interaction through the C=N double bond. This orientation is also reminiscent of its analogue structure in the vacuum and implicit solvent phases (Figure 5.3), although it also features a H-bond between the nitrogen atom and the explicit water molecules.

Further hydrogenation of the CH_2NH intermediate affords CH_2NH_2 in an endergonic process by +0.83 eV. Interestingly, this latter species acts as a H-bond donor to the solvent environment via its N–H bond, which contrasts with the H-bond acceptor interaction seen for CH_2NH. We also note that the distance between CH_2NH_2 and the surface is increased to 2.874 Å compared to 2.332 Å with implicit solvent. This illustrates the competing interactions of the CH_2NH_2 intermediate with the surface and the solvent. From this species, the formation of the 4-electron product, CH_3NH_2, occurs next. Methylamine is experimentally observed as the major product,[82] has a relative energy of –2.48 eV and is more stable than CH_2NH_2 by 1.45 eV. We also found that there exists a H-bond between

the lone pair of the N atom and the water network (N···HO = 1.852 Å). While the presence of this H-bond may initially appear to act as a hindrance to desorption, it is not difficult to imagine a sequence of reorganization events within the solvent whereby CH_3NH_2 is shuttled to the bulk solvent. However, should CH_3NH_2 linger near the cathode, it may be further hydrogenated to $CH_3NH_3^+$ in an endergonic process by +0.57 eV. As with implicit solvent, Bader charge analysis (Table S2) revealed that only a proton has been shuttled across the N···HO to form $CH_3NH_3^+$ (q_{mol} = +0.774), with the corresponding electron appearing to be delocalized between the water layer and the surface slab (q_{water} = –0.125 and q_{slab} = –0.649, respectively).

Further hydrogenation of $CH_3NH_3^+$ results in the generation of CH_4 and NH_3 as the final 6-electron eHCNRR products. This step is thermodynamically downhill with a relative energy of –3.33 eV, driving the overall reaction forward. As is the case with the major product, CH_3NH_2, a series of reorganization events can be imagined wherein both CH_4 and NH_3 are diffused through the solvent water molecules via hydrogen bonding.

The lack of chemisorbed intermediates observed throughout the eHCNRR with explicit solvent is thought to be due to the strong interaction of the cyanide intermediates with the explicit solvent, which is absent in the implicit solvent and vacuum phases. However, it should be noted that large variations in the Fermi levels across solvation phase may be responsible for changes in the binding of intermediates. This elicited an investigation into the Fermi levels of the intermediates, as well as the eigenvalues of the core levels. These calculations are performed using pseudopotentials, meaning that only valence electrons are calculated explicitly based on the assumption that core electrons do not participate in chemical processes. As such we can use the eigenvalues of the core electrons as a reference to align the energy levels, as seen in Table 5.5 below.

Table 5.5. Alignment of the energy levels of the HCN intermediate to the hydrogen covered Ni slab in vacuum. All core levels are calculated for the same Ni atom throughout the reduction reaction pathway, *i.e.*, the core energies of a Ni atom in the calculation with HCN is aligned with the core energies of the same Ni atom in the hydrogen covered slab. All energies are presented in eV.

	1s	*2s*	*2p*	*3s*	*3p*	E_{Fermi}
Vacuum						
Slab	–8207.33	–976.01	–838.95	–104.94	–65.23	–2.99
HCN	–8207.25	–975.93	–838.86	–104.86	–65.15	–2.91
HCN – Slab	0.08	0.08	0.08	0.08	0.08	0.08
Implicit Solvation						
HCN	–8211.07	–979.75	–842.69	–108.69	–68.97	–6.72
HCN – Slab	–3.74	–3.74	–3.74	–3.74	–3.74	–3.74
Explicit Solvation						
HCN	–8205.12	–973.80	–836.74	–102.74	–63.02	–0.78
HCN – Slab	2.20	2.20	2.20	2.20	2.20	2.20

In this manner, we are able to align the energy levels of each intermediate in each phase (vacuum, implicit and explicit solvent) to a common reference, allowing for comparison. We have only performed this for intermediates present across all three phases, *i.e.*, we have not considered transitions states as they only appear in the presence of the explicit solvent. We note that there is zero difference in the differences between energy levels, and this holds for each comparable intermediate. A comparison of the evolution of the (relative) Fermi levels throughout the eHCNRR is consequently possible and is presented in Figure 5.8.

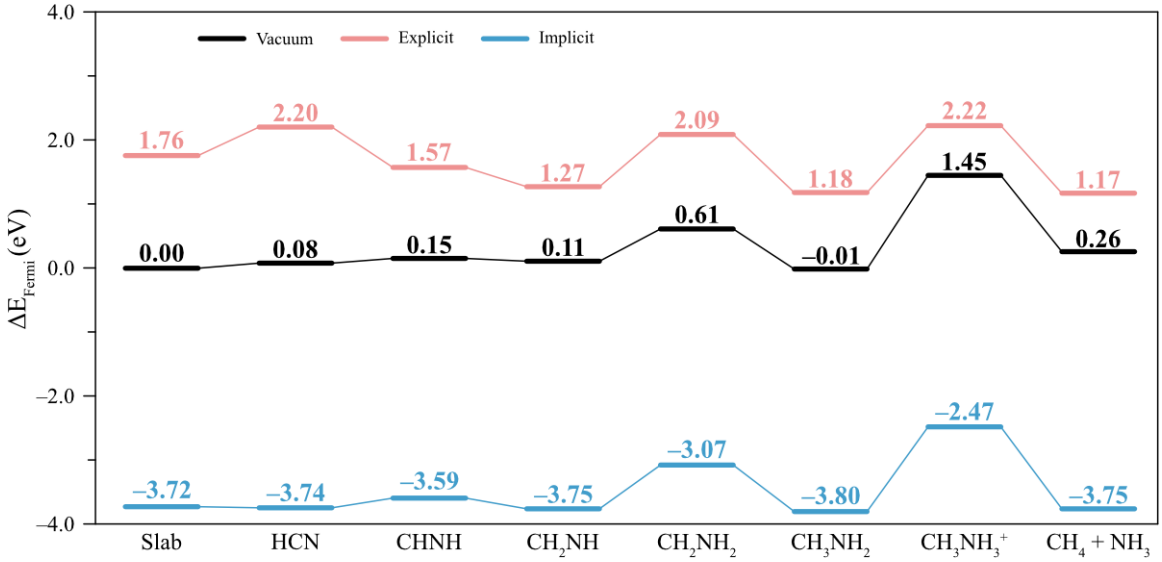

Figure 5.8. A comparison of Fermi levels across different solvent phases compared to the core levels of the hydrogen covered Ni surface in vacuum, specifically a subsurface Ni atom.

The relative Fermi levels appear to vary wildly across different phases; however, these differences can be easily rationalised. It is essential to note that the reference potential with implicit solvent is aligned with that of the bulk electrolyte, causing a shift in the Fermi level due to the zero average electrostatic potential in the simulation cell.[140] As such we investigate the variation in Fermi level across intermediates the same phase. For instance, the change in the relative Fermi levels from CH_3NH_2 to $CH_3NH_3^+$ is observed to be +1.46 eV, +1.32 eV, and +1.04 eV in vacuum, implicit solvent, and explicit solvent respectively. While there is a non-negligible difference between these values, it is unclear as to whether or not they are large enough to account for the changes in the relative Gibbs energies, which are attributed to site-specific effects such as H bonding with the water bilayer.

An overall examination of the eHCNRR mechanisms reveals the following key differences between the various solvation models investigated in this work. Firstly, in contrast to the reaction pathways modelled in vacuum and implicit solvent, the mechanism with explicit solvation features no chemisorbed intermediates. Secondly, only when we model the solvent explicitly, we observe the formation of the metastable CHNH intermediate which rapidly evolves to the more stable CH_2N species. Thirdly, the PDS predicted with explicit solvent (*i.e.* $CH_2NH \rightarrow CH_2NH_2$) differs from that found in vacuum and implicit environments (*i.e.* HCN→*CHNH). The limiting potentials calculated for both explicit

solvent and vacuum models are in close agreement with each other (*i.e.* –0.83 and –0.79 V_{RHE}, respectively) whereas the potential determined via implicit solvation results in a larger value (*i.e.* –0.94 V_{RHE}). Hence, we conclude that, despite the water bilayer not being able to fully capture the effect of the aqueous electrolyte, the presence of explicit water molecules is essential for the accurate description of the eHCNRR process. Future studies may focus on hybrid solvation models where a discrete number of explicit solvent molecules are paired with an implicit dielectric continuum to reduce computational cost, as well as the investigation of constant potential calculations. These insights may also be applicable to other electrochemical reactions which involve weakly bound intermediates.

5.3.5 Calculations under Constant Potential

Prior to this point, the role of the applied electrochemical bias has been contained in the CHE model, wherein a correction is applied *a posteriori* per modelled PCET.[147] The limitations of this model have been discussed previously. Calculations performed with the CHE have been performed at a constant charge. As such, we have endeavoured to include the applied potential to the eHCNRR via GC–DFT calculations, or constant potential calculations. Calculations performed in this fashion include another loop within the SCF loop, wherein N_e is optimised according to a target potential. The system then optimises the placement of said electrons and subsequently updates the ionic positions, with the intent to satisfy a force convergence criterion. The inclusion of this extra iterative cycle makes these calculations quite expensive, and as such we have refrained from modelling any explicit solvent calculations, with the intent to isolate and attribute any changes to the inclusion of the applied potential.

Initially, we modelled the eHCNRR intermediates at 0.0 V_{RHE} to establish a frame of reference for any further calculations, *i.e.*, as a benchmark, and the full reaction profile can be seen below in Figure 5.9. Immediately, when compared to the energies calculated at constant charge (Figure 5.5) it can be noted that the energies are more endergonic when fixed at 0.0 V_{RHE}. It is interesting to note that the difference across intermediates is not constant, that is to say that the application of an electrochemical bias does not incur a constant shift across all intermediates. The PDS is identified as the largest difference between intermediates, in this case the difference between *CHNH and HCN, which is equal to 0.989 eV. As such we have applied this difference as our target reducing potential,

perhaps naively, with the intent to make the reaction pathway thermodynamically downhill. We have also performed a Bader charge analysis on each intermediate at both potentials, the results of which is summarised in Table 5.6 below.

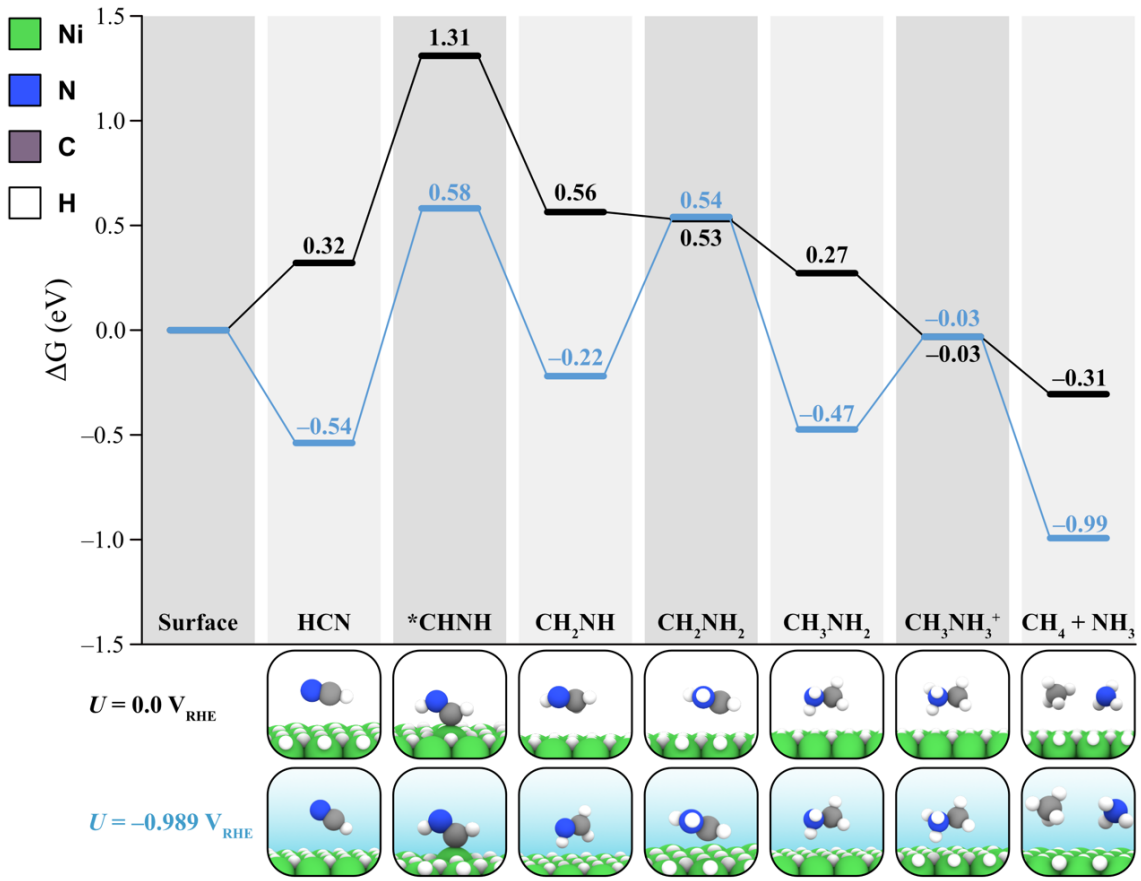

Figure 5.9. Gibbs energy profile for the reduction of HCN at 0.0 V_{RHE} (black trace) and –0.989 V_{RHE} (blue trace). Geometries of the eHCNRR intermediates are visible beneath the plot, with the top and bottom row of geometries referring to eHCNRR intermediates at 0.0 V_{RHE} and –0.989 V_{RHE}. Both traces are referred to the clean Ni(111) surface with the same hydrogen coverage calculated at either 0.0 V_{RHE} or –0.989 V_{RHE}. All GC–DFT calculations presented here are performed in the presence of an implicit solvent, with a dielectric constant of 78, as provided by VASPsol.

Several geometrical changes occur upon changing potential from 0.0 V_{RHE} to –0.989 V_{RHE}. For instance, the initial binding of HCN changes dramatically. At 0.0 V_{RHE}, HCN converges to a geometry where it is parallel to the surface, implying an interaction between the triple bond of the intermediate and the surface. However, at the very reducing potential of –0.989 V_{RHE}, there is an obvious tilting of the HCN molecule towards the surface. The distance between the H atom of HCN and the closest Ni atom is reduced from

3.882 Å to 3.403 Å. Referring to Table 5.6, this can be rationalised as an increase in the negative charge of the surface slab (localised in the hydrides) attracts the positive carbon and hydrogen atoms, which have charges of +0.920 and +0.297, respectively. We also note that this tilting is quite similar to the one observed in the presence of explicit solvent where charge separation resulted in the localisation of an electron is the Ni surface.

The *CHNH intermediate is quite interesting in that there is a large stabilisation of the chemisorbed intermediate, similar in magnitude to HCN, however there is a negligible change in the geometry of the system *i.e.*, differences in bond lengths that are in the second or third decimal. Referring to Table 5.6 allows us to observe a transfer of charge from the surface to the adsorbate (q_{mol} = –0.243). It can be assumed that this transfer of charge is from the hydride species, as their charge is reduced from –2.405 to –2.196. We also note that the ΔΔG between HCN and *CHNH increases from 0.99 eV to 1.12 eV at 0.0 V_{RHE} and –0.989 V_{RHE}. At first glance, one would assume that such a difference in the thermodynamics would bode poorly for any associated kinetics, however it must be kept in mind that there is an absence of explicit solvent molecules to potentially facilitate the hydrogenation of HCN under electrochemical conditions.

Table 5.6. Bader charge analysis of eHCNRR intermediates at 0.0 V_{RHE} and –0.989 V_{RHE}. We have grouped the charges into three fragments, the cyanide adsorbate (q_{mol}), the Ni atoms comprising the surface (q_{surf}), and the H atoms that make up the surface coverage ($q_{coverage}$). The net charge, in this case, should not equal zero, but rather equal the number of additional/subtracted electrons from the system.

	U = 0.0 V_{RHE}			*U = –0.989 V_{RHE}*		
	q_{mol}	q_{surf}	$q_{coverage}$	q_{mol}	q_{surf}	$q_{coverage}$
Surface	–	1.916	–2.275	–	1.436	–2.462
HCN	–0.012	1.820	–2.162	–0.034	1.397	–2.405
**CHNH*	–0.056	1.828	–2.074	–0.243	1.374	–2.196
CH_2NH	–0.019	1.847	–2.191	–0.048	1.319	–2.331
$CH_2NH_2^+$	0.927	1.780	–2.197	0.709	1.317	–2.335
CH_3NH_2	–0.025	1.787	–2.147	–0.043	1.330	–2.305
$CH_3NH_3^+$	0.957	1.779	–2.216	0.913	1.274	–2.365
CH_4 + NH_3	–0.026	1.802	–2.133	–0.042	1.330	–2.263

Methanimine, or methylene imine (CH_2NH), undergoes a process similar to HCN when applying negative potentials, however there is no tilting of the molecule, but rather a rotation around the CN bond axis. At 0.0 V_{RHE}, the imine is planar to the surface, with all C–H and N–H bonds parallel to the slab. Upon applying a negative potential, a rotation occurs so that the C–H and N–H bonds are perpendicular to the Ni surface. This rotation facilitates attractive interactions between the H atoms coordinated to the C and N atoms (q = +0.022 and +0.366, respectively) to point directly at the negatively charged surface. This rotation also prevents clashing between the nitrogen lone pair and the hydride covered surface. Again, the energy of the intermediate is strongly stabilised with the applied bias, with a relative energy of –0.22 eV being observed as opposed to 0.56 eV when compared to the hydrogen covered surface.

The next intermediate is one of two incredibly interesting intermediates. The CH_2NH_2 intermediate, revealed to be an iminium ion by Bader charge analysis (q_{mol} = +0.927 and +0.709 at 0.0 V_{RHE} and –0.989 V_{RHE}) is found to have energies that are seemingly unaffected by the applied bias. There is a slight change in geometry when applying a reducing potential. Initially, CH_2NH_2, or rather, $CH_2NH_2^+$ is 3.460 Å from the surface,

however when applying a negative potential this decreases to 3.046 Å. Irrespective of these two potentials, these values are too far apart to state that there is a bonding interaction between the surface and the iminium ion. These findings are substantially different from those found at constant charge, wherein a discrete bonding interaction is confirmed by charge density difference. Such analysis is difficult in this case as it is unclear how to partition the electrons across the surface and adsorbate fragments.

The major product, CH_3NH_2, is stabilised by the applied potential, however not to the same degree as the initial eHCNRR intermediates, but rather by 0.60 eV. The geometry of the intermediate is also unchanged by the electrochemical bias. CH_3NH_2, however, becomes more interesting when looked at in comparison to the following intermediate. The methylammonium ion, $CH_3NH_3^+$, is one of the more interesting intermediates to be examined at different applied potentials. Despite an applied bias of nearly –1.0 V_{RHE}, the relative energy of the intermediate remains at –0.03 eV. It appears to be largely independent of the applied bias. This can be reinforced by examining the results of the Bader charge analysis (Table 5.6.). The charge of $CH_3NH_3^+$ changes marginally from +0.957 to +0.913 at 0.0 V_{RHE} and –0.989 V_{RHE}, respectively. Indeed, the applied bias only affects the charge of the Ni surface and the H coverage. As such, the formation of $CH_3NH_3^+$ at a potential of 0.0 V_{RHE} is exergonic relative to CH_3NH_2, whereas at the reducing potential of –0.989 V_{RHE} it is endergonic by 0.44 eV.

The minor products, CH_4 and NH_3, in a similar fashion to CH_3NH_2, are also relatively unaffected by the potential in terms of geometry. The energy of the minor products, however, is shifted down by 0.68 eV upon applying a negative potential. Indeed, there is also no notable differences in the Bader charge analysis across potentials. It is noted that the overall reaction energy at constant charge is –1.05 eV (see Figure 5.5), a value more stable than both the energy calculated at 0.0 V_{RHE}, –0.31 V_{RHE}, and the energy calculated at –0.989 V_{RHE}, –0.99 eV. The reason for this is unclear as of yet, however it may be the case that intermediate potentials stabilise this final intermediate.

The introduction of and variation of the applied electrochemical bias to the intermediates present in the eHCNRR has proven to be very insightful, while also challenging preconceived notions regarding more traditional constant charge calculations. We have shown that the applied potential instigated several changes in the geometries of

intermediates, results in charge transfer to chemisorbed intermediates and additionally may not affect certain intermediates. These calculations were performed under the assumption that the low energy pathway at constant potential would follow the same scheme as the low energy pathway at constant charge; however, in light of these differences it may be apt to revise any such previous assumptions and model all possible intermediates of the eHCNRR with the electrochemical bias.

5.4 Conclusions

This chapter has focused on the role of the aqueous environment for the more effective modelling of the reduction of cyanide on a Ni(111) surface. This study was performed in an incremental fashion, beginning with the inclusion of a single water molecule with the purpose to circumvent the effective TS of 1.92 eV (labelled as **TS2** in Chapter 4) calculated for the isomerisation of HCN to *CNH. This was achieved, and the vacuum phase barrier was reduced from 1.92 eV to 0.2 eV. This process, however, is limited by the fact that our initial state is *CN, whereas experimental conditions imply that cyanide should be in the form of HCN. Nevertheless, the facilitation of *CNH formation by water allows for accessing a reduction reaction pathway that favours the formation of methane and ammonia. In qualitative agreement with this, experimental studies show that the reduction of cyanide under basic conditions shift the ratio of products towards methane and ammonia.

The inclusion of one solvent molecule does not account for the aqueous environment however and largely serves as a proof of concept. As such we have investigated and compared the effects of implicit and explicit solvation methods on the eHCNRR on a Ni(111) surface. We find that accounting for the solvent environment by means of an implicit dielectric continuum has a minimal effect overall on both the geometries of the reaction intermediates and their energies (*i.e.* 0.02-0.25 eV) compared to calculations in vacuum.

In contrast, the inclusion of a water bilayer to model the eHCNRR process culminates in several drastic changes regarding the geometries and energetics of intermediate species. For example, we observe a very different initial binding mode of HCN which can be attributed to explicit site-specific interactions. This binding mode facilitates the unveiling of a metastable intermediate, CHNH, which subsequently undergoes fast hydrogenation via

a rebound mechanism involving the water bilayer, leading to the more stable intermediate CH_2N. In addition, we report a different potential limiting step from the eHCNRR modelled in the presence of vacuum and implicit solvent phases. It should also be kept in mind that all previously chemisorbed intermediates were found to be physisorbed upon the inclusion of the explicit water bilayer. In the same vein, reaction intermediates which are physisorbed in the gas phase may be more liable to undergo some interaction with the solvent. We believe that this is due to explicit site-specific effects (hydrogen bonding) which are neglected in both the vacuum and implicit solvent phases.

Finally, we have endeavoured to account for the applied bias in our system, applying potentials of 0 V_{RHE} and –0.989 V_{RHE} comparing both and investigating the role of large reducing potentials on the eHCNRR. These calculations have revealed the presence of two intermediates that undergo charge separation, $CH_2NH_2^+$ and $CH_3NH_3^+$, the energies of which are unaffected by the applied potential. The geometries of some intermediates are observed to fluctuate with the negative potential, preferring to direct lone pairs away from the cathode. We also observe an overall stabilising shift in the thermodynamic profile, however the energetic differences between some intermediates only decrease slightly, or in the case of the PDS, increase from 0.99 eV at 0.0 V_{RHE}, to 1.12 eV at –0.989 V_{RHE}. Such changes, while stabilising the intermediates and potentially making them accessible at standard temperatures and pressures, may be detrimental to a reaction as the formation of thermodynamic sinks may occur. Ultimately, this study on the applied electrochemical bias serves to highlight the differences observed between GC-DFT and DFT calculations performed using the CHE, hopefully prompting some revision of theoretical electrocatalytic reaction mechanisms.

Chapter 6 Photothermal Decomposition of Ammonia

6.1 Introduction

Up until now, this thesis has been concerned with the synthesis of ammonia, from already fixed nitrogen sources, via electrochemical means. It seems fitting to conclude this thesis with a chapter concerned with the decomposition of ammonia. Ammonia while mainly used as fertiliser, or as a precursor to fertiliser, is garnering much interest, both academically and industrially, as a viable solution to the ongoing energy crisis.

As the world shifts to renewable energy sources (solar, wind, hydro), there needs to be security regarding their intermittent nature. Consequently, there has been much work investigating energy storage. The field of energy storage is wildly varied, and several unique and creative approaches of differing scales have been attempted and developed.

One such promising avenue of research is the chemical storage of the energy vector, H_2 is a promising field of study, with the chemi- or physisorption of hydrogen into or onto materials such as metal hydrides, metal-organic frameworks (MOFs), or carbon based materials such as fullerenes, zeolites, and grapheme.[233] Ammonia has received a great deal of interest as a candidate for the long term storage of hydrogen. There are several attractive prospects to using ammonia as a vehicle for hydrogen storage and transportation, not least of which is the fact that NH_3 is stable as a liquid at room temperature and at low pressures, *ca.* 8 atm, making storage a non-issue.[89] Additionally, NH_3 has a high hydrogen storage capacity (17.7 wt. %), a lower cost of storage and, due to our reliance on the Haber Bosch process, pre-existing infrastructure for transport and storage.[83,234] Ammonia can be decomposed catalytically to give carbon free hydrogen, or it can be directly used as a fuel, *i.e.*, in fuel cells or combustion engines.[84]

The catalytic decomposition of ammonia to nitrogen and hydrogen is an endothermic process, and, as such, is favoured at high temperatures, typically greater than 450 ºC.[235,236] Currently, the state of the art catalyst is one composed of Ru nanoparticles placed on a CNT support with a KOH promoter.[90] Ru is a precious metal however, costing as much as €14,700 kg^{-1}.[237] Hence, there is an onus to develop cost effective catalysts or

failing that, techniques that allow for earth abundant materials to be efficient catalysts at lower temperatures.

The use of light to facilitate heterogeneous catalytic processes was made famous by the work of Fujishima and Honda, who split water on a TiO_2 photoelectrode using clean and renewable solar energy, popularising the field of photocatalysis.[238] Photocatalysis typically involves, upon absorption of a photon of sufficient energy, the excitation of an electron, generating excited electron-hole pairs. These charge carriers are then employed in catalytic processes, facilitating the reduction or oxidation or adsorbed substrates. Researchers have taken the concepts of photocatalysis one step further by synergising the effects of light and heat via photothermal catalysis.

Traditional heterogeneous photocatalysts tend to be semiconductors, operating by the absorption of a photon that has an energy equal or higher than the band gap of the material. In metal nanoparticles, however, the incident light may be in phase with conducting electrons, effectively maximising the electric field on the surface of metallic nanoparticles. Non-radiative decay of the light induced excitation may result in the generation of electron-hole pairs, which may perform photochemical work, or through electron-electron collisions, producing local heating.[97]

In this chapter we investigate, alongside our experimental collaborators (the research group of Prof. Jorge Gascon, KAUST), a MOF-derived iron based photothermal catalyst for the decomposition of ammonia. We aim to separate and potentially study the effects and light and heat separately for two model surface systems, metallic Fe and Fe_3O_4.

6.2 Experimental Background

All experimental work was performed by the group of Prof. Gascon in KAUST, who developed the photothermal catalyst (Fe@C) in question via the pyrolysis of Basolite F300 (Fe-BTC) at 600 ºC for 6 hours under a nitrogen atmosphere. Powder X-ray diffraction (PXRD), seen below in Figure 6.1 (right), allowed for the identification of a mixture of magnetite (Fe_3O_4), iron carbide (θ-Fe_3C), and metallic iron (Fe). Transmission electron microscopy (TEM) revealed the formation of Fe nanoparticles (NPs) within graphitic carbon, with two discrete NP size distributions of 30 ± 10 nm and 4 ± 2 nm.

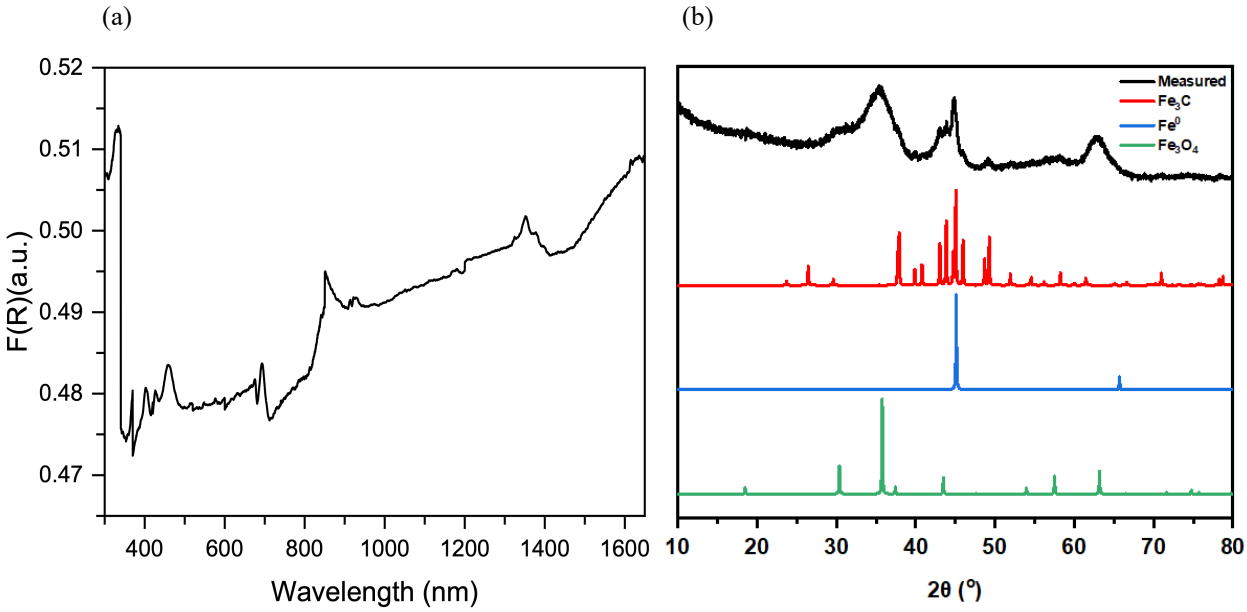

Figure 6.1. Absorption spectrum (a) of Fe@C across the UV, visible and NIR regions of light displaying broad light absorption, calculated using the Kubelka-Munk function, F(R). PXRD (b) of MOF derived Fe@C identifying the contributions of Fe_3C, metallic Fe, and Fe_3O_4.

The ability of Fe@C to absorb light across the ultraviolet (UV), visible and near infrared (NIR) regions was also investigated and is displayed in Figure 6.1 (a). Fe@C was found to display a strong absorption across all three regions, indicative of carbon-based materials, emphasising their potential as supports for photothermal catalysts.

X-ray photoelectron spectroscopy (XPS) analysis further revealed that the oxide component of Fe@C was made up of magnetite and haematite (Fe_2O_3), as opposed to only magnetite. It also revealed that Fe@C was mainly composed of Fe_3O_4, and metallic Fe, accounting for 74.71 % and 13.64 %, respectively.

The use of an alkali promoter has been reported as essential in enhancing the decomposition of ammonia due to electron donation from the promoter to the active site.[239,240] As such, a pool of alkali species (K, Ba, and Cs) and their concentrations were sampled and their role on the photothermal catalytic performance of Fe@C was investigated. It was found that a 2 wt. %K resulted in the best conversion of NH_3 to N_2 and H_2. As such, all further experiments were performed with this additional promoter. The variation of weight hourly space velocity (WHSV) of NH_3 was also investigated. This parameter is crucial for reactor design, and is defined as the mass flow rate (the amount of substrate that flows during a

certain time) divided over the mass of the catalyst.[241] It is an important quality to optimise, as a higher value means that the substrate spends less time in contact with the catalyst, which could result in poorer conversion rates and the underutilisation of the material. Lower rates imply that the substrate spends more time interacting with the catalyst and could potentially lead to undesired side reactions, or poisoning. Consequently, the selectivity of a process can be tuned by altering this parameter.

In the context of the photothermal decomposition of NH_3 on Fe@C, four different flow rates were sampled, 40,000, 20,000, 10,000, and 1,000 mL g^{-1} h^{-1} under light irradiation and are summarised in Figure 6.2a. These tests were performed until a steady state of conversion was reached. It should be stated that these tests were done in the absence of external heating, and as such, the resulting temperature associated with each WHSV is reported in Figure 6.2b. At the lowest WHSV of 1000 mL g^{-1} h^{-1}, the system achieves an incredibly high NH_3 conversion of *ca.* 80%, and reaches temperatures of roughly 300 °C. This demonstrates the ability of Fe@C to achieve and maintain high NH_3 conversion under a continuous flow of NH_3.

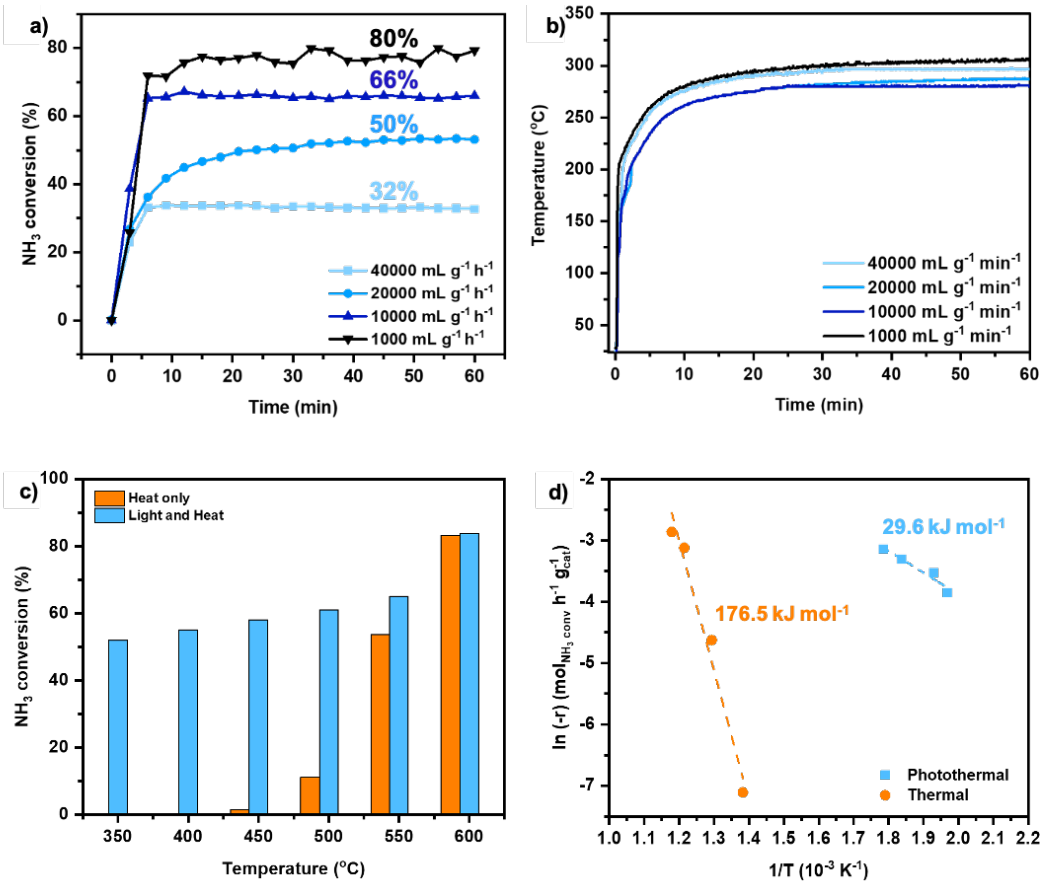

Figure 6.2. Investigations of the photothermal decomposition of NH_3 on the MOF-derived Fe@C catalyst. (a) NH_3 decomposition with light irradiation (with an intensity of 4.65 W cm^{-2}) and in the absence of external heating, performed at different WHSVs of 40,000, 20,000, 10,000, and 1,000 mL g^{-1} h^{-1}. (b) Temperature profiles corresponding to the different WHSVs tested in (a). (c) Catalytic performance of Fe@C under external heating in both the absence (orange) and presence of light (blue). These experiments were performed with a WHSV of 20,000 mL g^{-1} h^{-1} on 2 wt. %K promoted Fe@C. (d) Arrhenius plots illustrating the rates of conversion of NH_3 under dark (orange) and light (blue) conditions performed in (c).

NH_3 decomposition over Fe@C was then performed under both light and dark conditions at different temperatures as seen in Figure 6.2c. Regarding experiments performed in the presence of light, additional external heating was supplied to reach the desired temperature. In the absence of light, it was found that the conversion of ammonia to nitrogen and hydrogen was negligible below 450 °C. The inclusion of light, however, saw conversion values ranging from 50% to 60% at temperatures ranging from 350 °C to 500 °C. Higher temperatures saw the difference in the conversion values between the two systems diminish, which is believed to be caused by a takeover of thermal effects as well as faster electron-hole recombination at higher temperatures.

Subsequently, Arrhenius plots (Figure 6.2d) were constructed for both photothermal and purely thermal reactions. Activation energies derived from the plots were found to be 29.6 kJ mol^{-1} and 176.5 kJ mol^{-1} for the photothermal and thermal conditions, respectively. This decrease in activation energy suggests that hot carriers assist in the decomposition of NH_3.

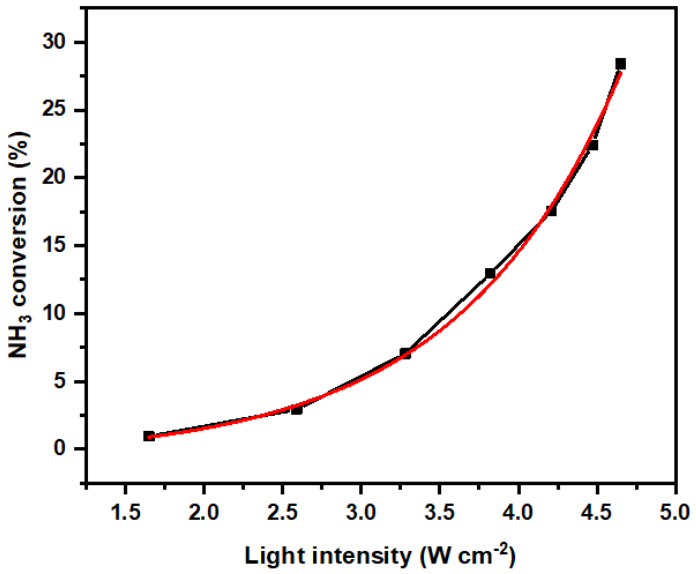

Figure 6.3. The effect of light intensity on the photothermal decomposition of NH_3 over the MOF derived Fe@C catalyst.

The light intensity was also varied at a constant temperature (Figure 6.3) to investigate the synergistic impact of light and heat, and whether or not one of these variables exerts a greater influence on the decomposition process. An exponential correlation between light intensity and conversion of NH_3 was reported. This is an indication of a process that is thermally driven, suggesting a light to heat mechanism, as opposed to one that is photothermal, *i.e.*, solar-powered thermochemistry as opposed to photochemical effects where photons induce electronic transitions.[242–244]

Efforts were made to exclude non-thermal effects from the system via the indirect illumination method developed and employed by Liu *et al.*[245,246] In this method, the Fe@C catalyst is covered by a 2 mm layer of Ti_2O_3. This material was chosen as it is an excellent photothermal material, capable of absorbing and converting the full solar spectrum into heat, and it is also virtually inactive for ammonia synthesis and decomposition.[246,247] The purpose of Ti_2O_3 is to absorb and convert light into heat, achieving an temperature profile identical to that obtained under direct illumination, albeit without non-thermal effects. It

was found that, with the addition of the Ti_2O_3 layer, hardly any conversion of NH_3 was achieved, implying the necessary non-thermal contribution of light.

In conclusion, the experimental results obtained by the group of Prof. Gascon display clear evidence that light irradiation plays an important role in the decomposition of NH_3 on Fe@C, achieving high conversions at low temperatures. However, there is also some evidence to suggest that a light to heat process occurs to some extent. To shed light into these experimental observations, we conducted a theoretical investigation of the NH_3 decomposition mechanism and an in-depth examination of the influence of heat and light.

6.3 Computational Methods

Plane wave density functional theory (DFT) calculations were conducted using projector augmented wave (PAW) pseudopotentials via the Vienna *ab initio* Simulation Package, (VASP).[187,189,226] Two distinct systems were modelled to represent the MOF-derived material Fe@C synthesized experimentally, based on characterization through powder X-ray diffraction, namely Fe metal and magnetite (Fe_3O_4). The calculations were performed using the Bayesian error estimation functional with van der Waals correlation (BEEF-vdW)[248] for Fe metal and PBE+U (U_{eff} = 3.7 eV) with D3 dispersion corrections, as developed by Grimme *et al.*,[249] for magnetite (see below for details).

Both materials were modelled with an energy cut-off of 500 eV for the kinetic energy of the plane waves. Geometry optimisations were carried out with an energy convergence criterion of 10^{-6} eV for the electronic steps and a force convergence criterion of 0.01 eV/Å for the ionic steps.

The bulk unit cell for body-centred cubic (bcc) Fe metal was obtained from the Materials Project database.[124] For all calculations involving Fe bulk, a Monkhorst-Pack k-point grid of 11×11×11 was utilized. The lattice parameter was optimised by relaxing the unit cell for a range of fixed volumes (97% to 104% of the original value reported in Materials Project, *i.e.* 2.840 Å). The Birch-Murnaghan equation of state was employed to fit the associated energies and volumes, resulting in an equilibrium lattice parameter of 2.849 Å. This value is in excellent agreement with previous theoretical works (a = 2.844 Å), corresponding to a relative error of 0.16%.[250] Additionally, the magnetic

moment for each Fe atom was calculated to be 2.279 μ_B, aligning closely with literature values (2.20 μ_B).[250]

Subsequently, a four-layer thick *p*(4x4) surface slab was cleaved along the (110) direction, identified as the most stable low-index surface facet.[251] To prevent interactions between periodic replicas, a vacuum of 15 Å was applied in the direction normal to the surface. For calculations involving the Fe(110) slab, a k-point mesh of 3×3×1 was implemented to maintain the same k-point density as in the bulk metal.

The surface energy (γ) was calculated using the following equation:

$$\gamma = \frac{E_{surf} - nE_{bulk}}{2A} \tag{6.1}$$

Where γ is the surface energy, E_{surf} and E_{bulk} are the fully relaxed ground state energies of the Fe(110) surface and bulk systems, A is the surface area, and n is a scaling factor to ensure E_{surf} and E_{bulk} describe the same number of atoms. The calculated surface energy of 2.37 J m^{-2} agreed well with experimental results (2.66 J m^{-2}), yielding a relative error of 4.59%.[252]

Additionally, the surface and subsurface magnetic moments were determined as 2.686 and 2.464 μ_B, respectively. These values are in good agreement with theoretical results from the literature (2.57 and 2.35 μ_B), with relative errors of 4.32 and 4.63%.[252]

Bulk Fe_3O_4, as a ferrimagnetic material, poses a complex modelling challenge. Its inverse spinel structure features Fe atoms at octahedral (Oh) and tetrahedral (Td) sites. The former are split between 2+ and 3+ oxidation states (Fe_{Oh}^{2+} and Fe_{Oh}^{3+}), while the latter are exclusively in the 3+ oxidation state (Fe_{Td}^{3+}). Antiferromagnetic coupling occurs between Fe_{Oh}^{3+} and Fe_{Td}^{3+} atoms, while spins of different octahedral Fe atoms align. Due to the self-interaction error (SIE), DFT-GGA fails to accurately localize the Fe 3*d* electrons, providing an imprecise description of Fe_3O_4. Hybrid DFT methods, wherein exchange is calculated as a linear combination of the (exact) HF and DFT exchanges, can be employed to counter the SIE. Liu and Di Valentin[253] used the hybrid functionals HSE06 and B3LYP to model the bulk structure of Fe_3O_4, reporting a distinct charge disproportionation amongst the octahedral Fe sites. For the purposes of modelling the NH_3 decomposition mechanism, however, the number of possible intermediates renders hybrid functionals as an unfeasible option due to their computational expense. An alternative method to correct for the SIE is

to apply the Hubbard parameter, in a method known as GGA+*U*, where a correction, *U*, applied to specific orbitals penalizes the delocalization of electrons. Herein, we employed Dudarev's method with an effective *U* parameter, described as the difference between on-site Coulombic and exchange parameters ($U_{eff} = U - J$).[254] The Fe *d* states were modelled with a U_{eff} = 3.7 eV, adapted from the work of Leeuw *et al*. who fitted the parameter to the band gap of magnetite.[255]

The bulk unit cell for Fe_3O_4, comprising 24 Fe and 32 O atoms, was sourced from the Open Quantum Materials database (ID 1283595).[135,256] Upon cooling to temperatures below 122 K, Fe_3O_4 undergoes a structural distortion and becomes insulating. This transition is referred to as the Verwey transition. Verwey postulated that at low temperatures a charge ordering occurs, inhibiting conductivity.[257] This idea was largely confirmed by Attfield *et al*.[258] who also observed through high energy X-ray diffraction electron localisation over three Fe units, a quasiparticle dubbed as a 'trimeron'.

To reflect the high temperatures employed in this work, we modelled Fe_3O_4 after the Verwey transition, namely as a cubic inverse spinel, with the space group $Fd\bar{3}m$. The lattice parameter was optimised following the same procedure described for the Fe metal, albeit using a Monkhorst-Pack k-point grid of 5×5×5. The calculated equilibrium lattice parameter of a = 8.511 Å aligned well with experiments (8.394 Å).[259] Fe_{Oh} and Fe_{Td} metal centers exhibited magnetic moments of +3.959 and –4.059 μ_B, respectively, resulting in an average oxidation state of +2.5 for the octahedral Fe atoms. These results were congruent with previous GGA+*U* studies, yet at odds with the aforementioned work by Liu and Di Valentin.[253,255,260–265] This engendered the use of the occupational matrix control method developed by Watson and Allen to improve the description of Fe_3O_4.[266] This method allowed us to define the occupancy of the d states for each Fe atom in the bulk Fe_3O_4. With this approach, the lattice parameter was reoptimised, yielding a slightly improved a = 8.476 Å, closer to the experimental value. Additionally, the Fe_{Oh}^{2+} and Fe_{Oh}^{3+} centers exhibited magnetic moments of 3.691 and 4.133 μ_B, respectively, consistent with Liu and Di Valentin's work using hybrid DFT functionals.[253]

Subsequently, a four-layer thick *p*(1x1) surface slab was cleaved along the (111) direction from the equilibrium bulk of Fe_3O_4, with a 15 Å vacuum perpendicular to the surface. The

(111) surface, chosen for its natural cleavage plane, proved more stable according to DFT+*U*, aligning with Schmid *et al.*'s experimental work.[267–274] However, being a Tasker type III surface, it is polar, requiring stabilization to eliminate the surface dipole. This was achieved through surface reconstruction by translating half a plane of atoms from the top surface to the opposite face and is discussed further on in Section 6.4.2. However, this resulted in the presence of undercoordinated Fe atoms. Upon sampling all available reconstructions, the lowest energy surface was found to contain, on one face, 8 Fe_{Td}^{3+} and 4 Fe_{Oh}^{2+}, and on the other face, 8 Fe_{Oh}^{3+} and 4 Fe_{Oh}^{2+}, as shown in Figure 6.4.

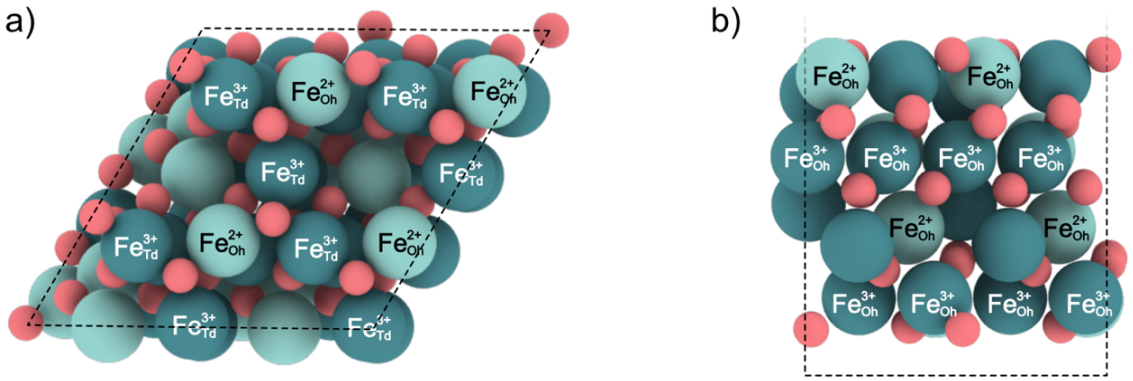

Figure 6.4. (a) Top and (b) side view representations of the lowest energy Fe_3O_4(111) surface after reconstruction.

The NH_3 decomposition mechanism was modelled on both Fe(110) and Fe_3O_4(111) surface slabs via sequential N–H bond cleavages. For the Fe_3O_4 system, reaction intermediates were initially optimised using the occupational matrix control to maintain the antiferromagnetic coupling of the Fe^{3+}atoms across both the tetrahedral and octahedral sites, as well as the parallel magnetic moments of the octahedral atoms. After optimisation, occupational control was turned off, allowing the system to relax while reading in the wavefunctions from the previous calculation. Due to the numerous spin configurations considered, calculations were initially performed at Γ-point, and the lowest energy intermediates were reoptimised with a denser k-point mesh of 5×5×1.

Relative energies, ΔE_{ads}, as presented in this chapter, were calculated as follows:

$$\Delta E_{ads} = E_{surf+ads} - E_{surf} - E_{ads} \tag{6.2}$$

Where $E_{surf+ads}$ is the energy of the slab with the bound adsorbate species, E_{surf} is the energy of the clean slab, and E_{ads} is the energy of the isolated adsorbate.

Vibrational frequencies were calculated within the harmonic approximation for each reaction intermediate, constraining the movement of all atoms comprising the surface slab except the adsorbate species. Gibbs energy corrections, G_{corr}, were computed using the thermochemistry module in the Atomic Simulation Environment (ASE) package at different temperatures and at the experimental pressure of 0.2864 atm.[275] For isolated gas species, the ideal gas approximation was adopted, wherein translational, rotational, and vibrational degrees of freedom are accounted for. These corrections included zero-point energies, entropy, and heat capacity contributions, added to the calculated potential energies.

Relative Gibbs energies were computed as:

$$G_{sys} = E_{sys} + G_{corr} \tag{6.3}$$

$$\Delta G_{ads} = G_{surf+ads} - E_{surf} - G_{ads} \tag{6.4}$$

Transition states (TS) were located using a combination of interpolation and local methods. More specifically, the climbing image nudged elastic band (CI-NEB) method was employed to initially construct a rough estimate of the minimum energy path (MEP) between the two minima of interest, utilizing 4 images in between them.[121] As the oxidation states of the metal atoms differ before and after the TS, the occupational matrix control method could not be applied to maintain the spin structure of the magnetite surface. To conserve the spin states of the interpolated images, the wavefunctions of the initial and final states were read into the images closest to their respective minima (*i.e.* the wavefunctions of the initial state was read by images 01 and 02, and the wavefunctions of the final state was read by images 03 and 04). The highest energy image calculated was subsequently used as an initial guess for the improved dimer method.[123] TS structures were confirmed by the presence of only one imaginary frequency along the reaction coordinate of interest.

The impact of light was considered by introducing a simulated photogenerated electron, operating under the assumption that light induces an electron-hole pair. It is important to note that introducing additional electrons to a supercell affects absolute energies, depending on the vacuum width. Nevertheless, the energies reported in this work are relative to the clean, charged surface slab with an equivalent vacuum width, effectively accommodating the electrostatic potential from the charged slab. It is also worth noting that all the results and discussion presented in this study pertain to trends in relative energies.

6.4 Results and Discussion

6.4.1 Modelling of NH_3 Decomposition on Fe(110) with and without Light

The modelling of NH_3 decomposition was initially done on a *p*(4x4) Fe(110) comprised of 4 layers. Firstly, we modelled the thermodynamics of the decomposition process, both with and without light, *i.e.*, for a surface slab with and without an extra electron. This entailed modelling the reaction intermediates outlined in the following steps:

$$NH_{3(g)} + {}^{*} \rightarrow {}^{*}NH_3 \tag{6.5}$$

$${}^{*}NH_3 \rightarrow {}^{*}NH_2 + {}^{*}H \tag{6.6}$$

$${}^{*}NH_2 + {}^{*}H \rightarrow {}^{*}NH + 2^{*}H \tag{6.7}$$

$${}^{*}NH + 2^{*}H \rightarrow {}^{*}N + 3^{*}H \tag{6.8}$$

$${}^{*}N + 3^{*}H + NH_{3(g)} + {}^{*} \rightarrow 2^{*}N + 6^{*}H \tag{6.9}$$

$$2^{*}N + 6^{*}H \rightarrow N_2 + 6^{*}H \tag{6.10}$$

Where * denotes an active site on the catalyst surface.

In Figure 6.5 below, we present the low energy pathway for NH_3 decomposition on a pure Fe(110) surface at a low temperature regime under dark (dark green trace) and light conditions (light blue trace). Under dark conditions, the initial binding of NH_3 occurs on a *top* site via the lone pair of ammonia in a nearly thermoneutral process with a relative energy of 0.04 eV. Subsequently, the first N–H bond cleavage occurs, producing the intermediate ${}^{*}NH_2$, which adsorbs on a *bridge* site, while the dissociated H atom occupies a three-fold hollow site. The following two N–H bond dissociation steps lead to intermediates ${}^{*}NH$ and ${}^{*}N$, converging to a four-fold hollow site, while the cleaved H atoms occupy the three-fold sites.

Simulating the influence of light by modelling the reaction in the presence of a photogenerated electron produced negligible changes in the overall energetics of the intermediates as well as their geometries. We attribute this negligible impact to the delocalisation and subsequent loss of the electron throughout the metal slab. This aligns with our expectations, considering the rapid recombination of photogenerated electrons and

holes in metals.[276] As such, regarding non-thermal effects, it is unlikely that Fe is the active surface.

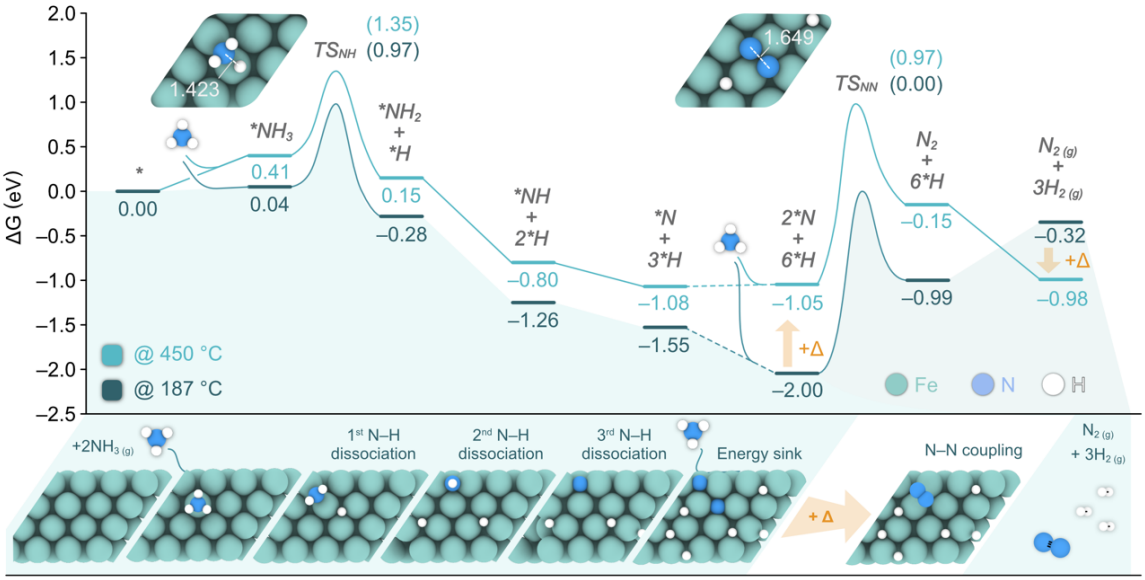

Figure 6.5. Gibbs energy profile for the decomposition of NH_3 on the Fe(110) surface illustrating the low-temperature regime under dark (dark green trace) and light (light blue trace) conditions. The geometries of optimised intermediates are displayed below the reaction profile.

We also note from Figure 6.5. the critical formation of a thermodynamic sink of –1.55 eV upon the complete dehydrogenation of a single ammonia molecule. This is only further deepened by the addition of a second, fully decomposed substrate molecule, and reaches an energy of –2.00 eV relative to the clean Fe surface. The overall reaction energy is calculated to be exergonic by –0.32 eV, implying that an energetic cost of at least 1.68 eV is required to desorb the formation and liberation of the end products, N_2 and H_2, when neglecting kinetic barriers.

We did however investigate the kinetics involved with the decomposition reaction on Fe metal, studying only two steps, the initial N–H bond cleavage, and the associative desorption of N_2, as these steps have been reported to be rate limiting, irrespective of the catalyst employed.[277] Figure 6.6 displays the energies and geometries associated with each of these TS structures. Energy barriers of 0.97 eV (93.59 kJ mol^{-1}) and 2.00 eV (192.97 kJ mol^{-1}) were calculated for the initial N–H dissociation (**TS_{NH}**) and the NN recombination (**TS_{NN}**), respectively. The recombination of nitrogen atoms is the rate limiting step and is qualitatively in agreement with Masel *et al.*'s findings on metallic Fe.[88] Furthermore, we

note that this barrier of $\mathbf{TS_{NN}}$ closely matches the experimentally determined value of 176.5 kJ mol^{-1} under dark conditions, as depicted in Figure 6.2d.

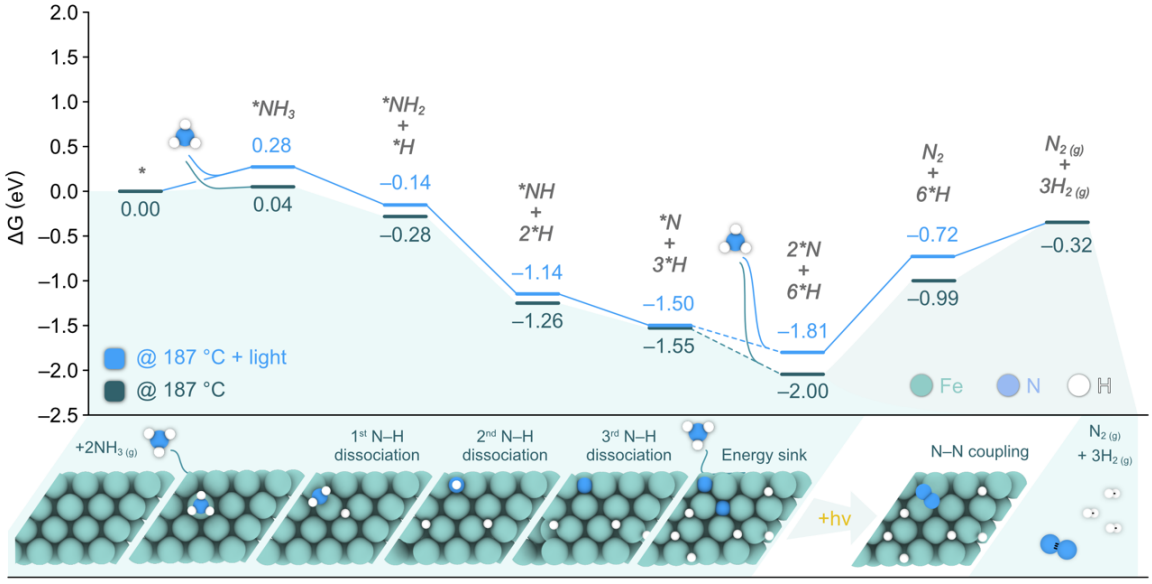

Figure 6.6. Gibbs energy profile for NH_3 decomposition on the Fe(110) surface at both high and low temperatures. Both traces are calculated under dark conditions. A second NH_3 molecule is adsorbed and completely dehydrogenated in order to explore the kinetics associated with the associative dissociation of N_2. Geometries of optimised intermediates are displayed beneath the reaction profile, whereas geometries of TS structures are shown as insets, with relevant distances given in Å.

Figure 6.6 also showcases the NH_3 decomposition mechanism calculated at an elevated temperature of 450 °C, marking the onset of NH_3 conversion under dark conditions, as illustrated in Figure 6.2c. At this higher temperature, the thermodynamic sink diminishes significantly, and the associative N_2 desorption becomes almost thermoneutral (from 1.68 eV at 187 °C to 0.10 eV at 450 °C), in excellent agreement with experimental observations. This phenomenon is attributed to the simultaneous increase and decrease in the Gibbs energies of the reaction intermediates and products relative to the reactants, respectively, driven by the entropy term. Consequently, we conclude that the reduction in the depth of the thermodynamic sink at elevated temperatures drives the formation of the reaction products under dark conditions, where thermal effects dominate, as evidenced in Figure 6.2c.

6.4.2 Reconstruction of Fe_3O_4(111) Surface

To investigate the influence of Fe_3O_4, the decomposition of NH_3 was modelled on the Fe_3O_4(111) surface slab, as discussed in Section 6.3. As mentioned briefly, in Section 6.3, the (111) facet of Fe_3O_4 is a Tasker III surface, meaning there exists a net dipole in the simulation cell perpendicular to the surface.[278] The potential due to a plane of charge q felt at a distance z from the surface is of the form,

$$V(z) = \frac{2\pi}{A} qz \tag{6.11}$$

Where A is the area of the cell. The electric field felt at z, E_{field}, is given by the gradient of the $V(z)$ and as such, is a constant.

$$E_{field} = \frac{2\pi}{A} q \tag{6.12}$$

Eq. 6.11 tells us that at an infinite distance z, the potential $V(z)$ is also infinite, and consequently, the surface energy diverges with the size of the simulation cell. As such, the Fe_3O_4(111) surface facet must undergo reconstruction to quench this dipole.[278,279] We have performed this reconstruction by simply translating half a plane of atoms from one side of the slab to the opposite face as outlined by Watson *et al*.[280] All possible translations are displayed in Figure 6.7, however there is still some nuance involved in modelling these specific oxygen and iron terminations.

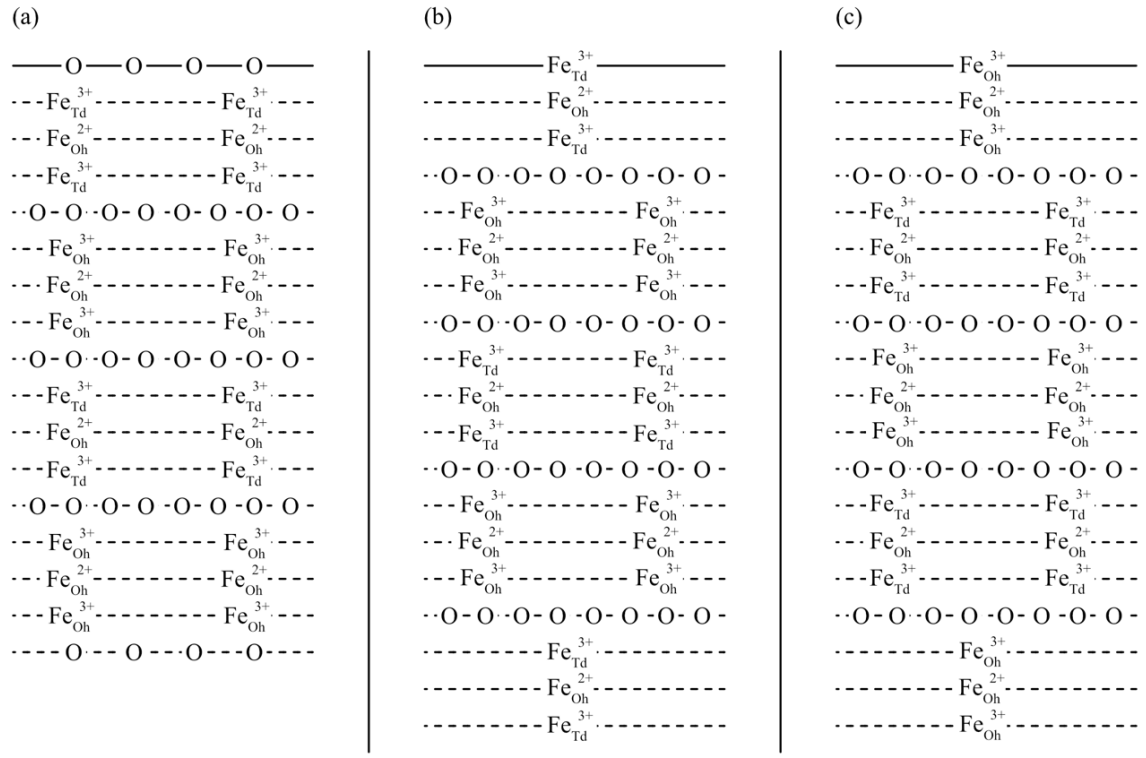

Figure 6.7. Stacking sequences for the reconstruction of Fe_3O_4(111) showing all possible configurations where the dipole is quenched. Stacking sequence (a) displays an oxygen terminated surface, whereas the sequences (b) and (c) are iron terminated. We note that there are two different layers containing iron atoms. One layer contains only octahedral iron atoms that all lie on the same plane in the direction parallel to the surface, *i.e.*, the x and y plane, whereas the other layer is staggered, with two pairs of tetrahedral iron atoms sandwiching another pair of octahedral iron atoms in the z direction.

For example, the oxygen terminated surface displayed in Figure 6.7 (left), is the result of translating half, or four oxygen atoms from the top surface face to the bottom face. It is unclear however, which four atoms to translate, and as such we have sampled all possible configurations for each reconstruction operation. Doing so led to an oxygen terminated surface as displayed in Figure 6.8 (a), which was calculated to have a surface energy of 3.25 J m^{-2}. This slab was comprised of two surface faces, with the 'top' surface consisting of Fe_{Oh}^{2+} and Fe_{Td}^{3+} ions, whereas the bottom surface face was comprised of Fe_{Oh}^{2+} and Fe_{Oh}^{3+} ions.

The charge ordering of magnetite is a much disputed topic, with substantial research efforts focusing on bulk magnetite.[258,281–286] In the case of Fe_3O_4 surfaces and nanoparticles however, there is much less information available. Consequently, we set out to optimise the

charge ordering of the oxygen terminated $Fe_3O_4(111)$ surface, while ensuring the slab was non-polar. This was done via the use of the occupational matrix control as described in the methods and involved exchanging the coordinates of Fe_{Oh}^{2+} and Fe_{Oh}^{3+} cations within layers, as seen below in Figure 6.8. Only layers containing octahedral cations were considered due to fact that their magnetic moments are all in the same direction, therefore any reorganisation of charge is assumed to be less challenging than between iron atoms of different coordination and spin direction. Additionally, electron transfer processes within magnetite are reported to occur between Fe_{Oh}^{2+} and Fe_{Oh}^{3+} cations on a time order of 10^{-11} s at room temperature.[287,288]

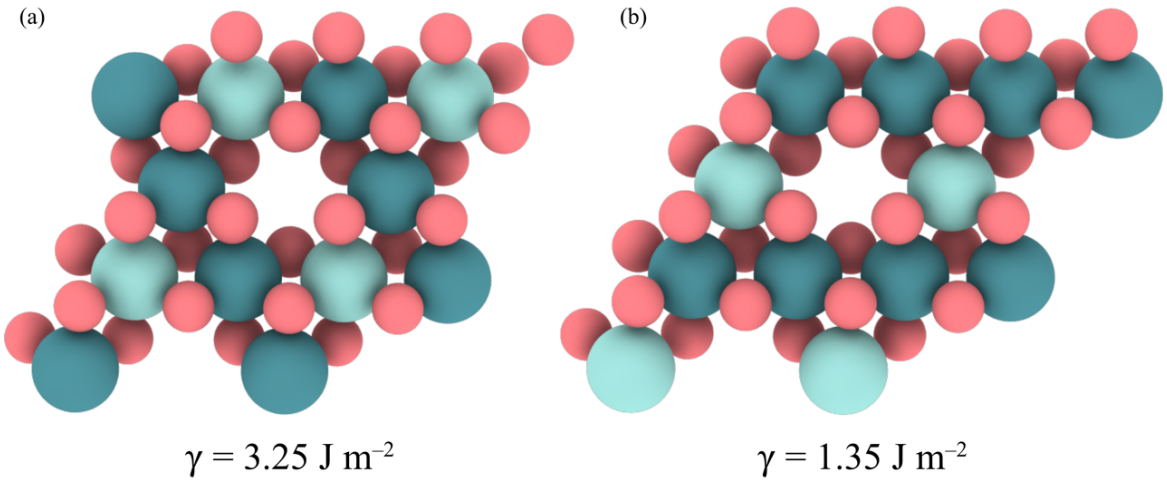

Figure 6.8. Top-down view of the charge ordering present in the second layer of the Fe_3O_4 surface slab before (left) and after (right) sampling different charge configurations. Of the configurations sampled, the most stable was one where the Fe_{Oh}^{2+} cations were arranged in the second layer so that they would be exposed in the hollows present in the top layer. This orientation decreased the surface energy by 1.90 J m^{-2}. Colour code: Fe^{2+} (light blue), Fe^{3+} (dark blue) O^{2-} (light red).

Electron transfer processes such as these, imply that there is no maintained charge ordering above the Verwey transition. Additionally, we note that the high temperatures employed experimentally may exacerbate this problem. However, in the framework of DFT, we cannot capture these dynamic processes and must attempt to optimise the surface as best we can.

6.4.3 Modelling of NH_3 Decomposition with and without Light

As the surface slab is asymmetric, we must consider the possibility that both surface faces are potentially active for the decomposition of NH_3. As such we sampled active sites on both top and bottom surface faces. The calculated reaction pathway for NH_3 decomposition, following the same sequence of steps as on iron metal, is presented in Figure 6.9, although we also included the following step instead of Eq. 6.10.

$$^*N + 3^*H + NH_{3(g)} + {}^* \rightarrow {}^*N + 3^*H + {}^*NH_3 \qquad (6.13)$$

DFT calculations indicate that NH_3 selectively binds to an Fe_{Oh}^{2+} site on the top surface, despite its lower acidity compared to Fe^{3+} ions. However, it should be noted that the surface reconstruction left Fe^{2+} ions undercoordinated, while the Fe_{Td}^{3+} were overcoordinated. With NH_3 chemisorbed, the first N–H cleavage leads to the formation of $^*NH_2$ on a *bridge* site and a surface OH group. This highlights a lack of competition for binding sites between N and H atoms, contrasting with the reactivity observed on pure Fe(110). We also note that the formation of this initial intermediate, predicted to be exergonic by –0.62 eV under dark conditions (grey trace), involves a comparable energy barrier (**TS_{NH}'**) to metallic iron (0.97 vs 0.95 eV). Subsequent N–H dissociation steps yield the intermediates $^*NH$ and $^*N$ on a three-fold site, along with two OH groups. Unlike on pure Fe metal, these steps leading to the complete decomposition of the first NH_3 molecule are uphill in energy by 0.08 and 0.27 eV, respectively. Overall, DFT calculations indicate a considerably diminished thermodynamic sink on the $Fe_3O_4(111)$ surface compared to metallic iron in the low-temperature regime, reducing from 1.68 to 1.02 eV, favouring NH_3 decomposition on $Fe_3O_4(111)$.

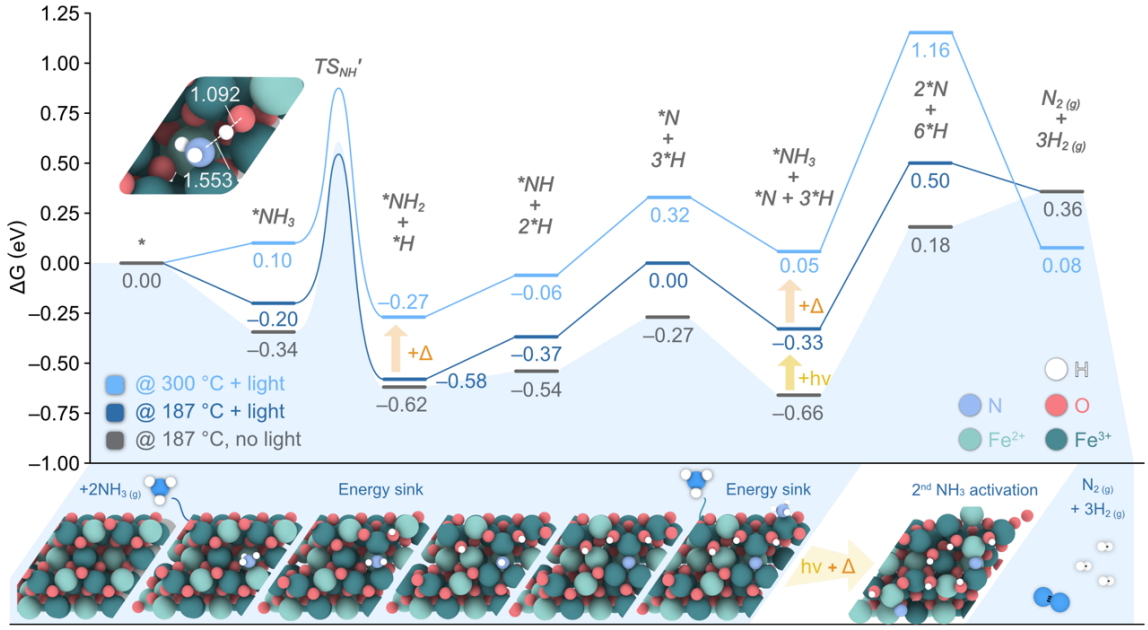

Figure 6.9. Gibbs energy profile for the decomposition of NH_3 on the $Fe_3O_4(111)$ surface. The grey trace refers to the system at low temperatures (187 °C). The dark blue trace describes the system at the same temperature, only shifted upwards due to the presence of light, denoted by hv. The light blue trace refers to the further shifting upwards of the thermodynamic profile by heating to 300 °C.

Introducing a photogenerated electron into the $Fe_3O_4(111)$ surface to mimic experiments under illumination (Figure 6.9, dark blue trace) results in its preferentially localization on a surface Fe^{3+} ion, subsequently reducing it to Fe^{2+}. In this configuration, the chemisorption of NH_3 is slightly less favourable compared to the system without the photogenerated electron. Accompanying this, the relative energy barrier for the first N–H cleavage decreases from 0.95 to 0.76 eV with the introduction of the photogenerated electron. We also note that the resulting $^*NH_2$ intermediate exhibits a similar energy under both dark and light conditions (–0.62 and –0.58 eV, respectively), while the remaining intermediates experience a notable upward shift in their energies under illumination. This shift, especially pronounced with the introduction of the second NH_3 molecule, leads to a relative energy increase from –0.33 to –0.66 eV. Consequently, the thermodynamic sink between this intermediate and the reaction products decreases from 1.02 eV under dark conditions to 0.83 eV under illumination. Crucially, this thermodynamic sink vanishes at temperatures above 300 °C (Figure 6.9, light blue trace) and the overall reaction becomes almost thermoneutral, aligning with the experimental data under illumination, where nearly equilibrium conversions are reached at temperatures of around 300 °C.

While these findings seem to agree nicely with experimental work, it must be kept in mind that there are several approximations made. For instance, the catalyst in question is a MOF-derived material and so may have several solid-solid interfaces that we have not considered. We have also neglected the role of the promoter which is claimed to be essential in donating electrons to the active site. Finally, we have approximated the role of light by including a photogenerated electron, resulting in modelling the ground state of a charged system. However, light does not add electrons to a system, rather it may induce charge separation generation electrons and associated holes. As such, it is difficult to say if modelling a charged ground state can approximate an excited state system with charge separation.

6.5 Conclusions

In this chapter we have collaborated with the group of Prof. Gascon (KAUST), who have developed a MOF derived Fe catalyst known as Fe@C for the purposes of efficient photothermal NH_3 decomposition. PXRD and XPS analysis revealed that this material was composed of mainly metallic iron and magnetite, as well as smaller amounts of haematite and iron carbide. In the absence of light, Fe@C achieved NH_3 conversion at temperatures greater than 450 °C, with an associated activation energy of 176.5 kJ mol^{-1}. Under light irradiation however, this activation energy was reduced to 29.6 kJ mol^{-1}, achieving *ca.* 50% conversion of NH_3 at temperatures of 350 °C.

Theoretical calculations allowed for the calculation of the thermodynamics and kinetics involved in the decomposition of NH_3. These calculations revealed the presence of a thermodynamic sink at low temperatures, however at 450 °C it is reduced and in equilibrium with the product species. Additionally, we have determined that the associative desorption of N_2 is hindered by a barrier of 192.97 kJ mol^{-1}, a value in good agreement with the activation energy of 176.5 kJ mol^{-1}. As such, we are confident in attributing the activity of Fe@C at hight temperatures and in the absence of light to metallic Fe. Regarding our approximation to light, Fe metal was unable to localise an extra electron and as such was deemed as likely, in the framework of our model, to be inactive for non-thermal effects involving light.

We also investigated the other major component of the Fe@C catalyst, Fe_3O_4. The (111) surface facet of Fe_3O_4 is a Tasker III surface however, necessitating the investigation of all

possible surface reconstructions. These calculations resulted in the slab being non-polar in the direction perpendicular to the surface, and revealed an oxygen terminated surface as the most stable configuration. The decomposition of NH_3 was then modelled on the $Fe_3O_4(111)$ surface, revealing the formation two energy sinks. The first sink is associated with the first NH cleavage, and the second occurs upon the adsorption of a second NH_3 molecule.

The inclusion of a fictitious photogenerated electron however, resulted in a marked decrease in the depth of the thermodynamic sinks, effectively shifting the relative energies of the NH_3 decomposition intermediates up. Consequently, this resulted in a decrease of *ca.* 0.20 eV in the effective transition state barrier for the first NH cleavage process. The inclusion of light, when paired with temperatures of 300 °C, resulted in the disappearance of the thermodynamic sink, which appears to agree with the experimental findings of equilibrium NH_3 conversion at 300 °C. It should be maintained however, that these systems are approximations to the real system. The manner in which we have approximated light informs us that photogenerated electrons may result in the easing of any energy sinks, although it is difficult to be certain of this without the effect of the correlated photogenerated hole.

Chapter 7 Conclusions and Future Work

7.1 Conclusions

The aim of this thesis was to investigate, via theoretical means, ammonia synthesis and decomposition processes on heterogeneous catalysts so as to contribute to the concept of a circular nitrogen economy. The larger part of this thesis revolved around electrocatalytic cyanide reduction towards ammonia, while the final chapter was focused on the decomposition of ammonia for the chemical storage of hydrogen.

In Chapter 4, we employed DFT methods to elucidate, for the first time, the reaction mechanism for the electrochemical reduction of a cyanide ion, in the form of NaCN, on a hydrogen covered Ni(111) surface. The reduction of cyanide occurs in an alternating manner, wherein hydrogenation occurs on the carbon and nitrogen atoms in turn. This mechanistic study revealed that methylamine dominates the product distribution due to its desorption from the surface, with calculations suggesting that should methylamine be stabilised on the surface, hydrogenation to methane and ammonia should be possible. These calculations also revealed the presence of an alternative reduction pathway, wherein hydrogen atoms are sourced from the surface coverage. This pathway disrupts the alternating hydrogenation scheme and decouples the formation of methane and ammonia. As such, methylamine does not occur, hinting at 100% Faradaic efficiency towards methane and ammonia. However, this second pathway is inhibited by the presence of a large transition state barrier (1.92 eV) associated with the isomerisation of hydrogen cyanide to hydrogen isocyanide, with energies that are comparable to isomerisation studies in the absence of the catalyst.

Chapter 5 builds upon this work, investigating the transition state that inhibits HCN isomerisation. It was found that the inclusion of one water molecule allowed for the circumvention of this large energy barrier in favour of a process that is much more energetically feasible. This process features the diffusion of the surface coverage followed by the shuttling of a hydrogen atom facilitated by a solvent water molecule, concluding in the accessing of a pathway that favours methane and ammonia formation. As this pathway

is dependent on the formation of *CN, basic conditions are required, a fact that is corroborated by experimental work.

The reduction of cyanide under acidic conditions, *i.e.,* as HCN, was then investigated through both implicit and explicit solvation models. The inclusion of the solvent as a dielectric continuum appeared to have a negligible impact on the energies and geometries of the reaction intermediates compared to those calculated in the vacuum phase. Explicit solvent molecules, in the form of a water bilayer, induced several changes in both geometries and energetics. Binding modes were also drastically affected, with previously chemisorbed intermediates converging to physisorbed intermediates due to competing interactions with the solvent. The explicit solvent allowed us to investigate kinetics associated with the eHCNRR, exposing a metastable intermediate, CHNH, which may undergo fast hydrogenation via a Grotthuss mechanism. Additionally, a different PDS is reported for the eHCNRR with explicit solvent, one which is prior to the formation of CH_3NH_2, admittedly casting doubt on the conclusions of the previous chapter.

We have also managed to account for the inclusion of the applied bias in the eHCNRR, albeit without explicit solvent molecules, applying both neutral and reducing potentials to the intermediates. We note two intermediates featuring charge separation that are apparently independent of the applied electrochemical bias, as well as several changes in geometry upon the application of reducing potentials. For instance, the lone pair present on the nitrogen atom converges to a geometry where it points away from the cathode. We also observe an overall stabilising shift in the Gibbs energy landscape, however energy differences between intermediates are not strongly decreased with the applied negative potential. As such, this chapter explores the differences between DFT calculations performed under a constant charge and constant potential.

Chapter 6, the final chapter of this thesis, is undoubtedly an outlier. We deviate from electrocatalytic ammonia synthesis, investigating the photothermal catalytic decomposition of ammonia alongside the group of Prof. Jorge Gascon in KAUST. Through theoretical calculations, we have studied their MOF-derived Fe catalyst using two surface model systems, metallic Fe and Fe_3O_4, to represent this material, whilst incorporating light via a fictitious photogenerated electron.

Fe metal was found to have strong agreement with experiments performed in the absence of light, with the transition state energy for associative nitrogen recombination, the RDS, matching well with the experimental activation energy. Additionally, DFT calculations demonstrated that at the onset temperature for NH_3 conversion, 450 °C, a thermodynamic sink of *ca.* –2.00 eV is greatly diminished, facilitating the formation of the reaction product under dark conditions. Fe_3O_4, following reconstruction and the optimisation of the charge ordering within the slab model, was found to also develop energy sinks upon the dehydrogenation of NH_3. Upon including light, *i.e.*, an extra electron, resulted in the energies of reaction intermediates being shifted upwards and reducing the depth of these thermodynamic sinks. Additionally, this resulted in the decrease of the effective transition state barrier associated with NH cleavage, implying, qualitatively, that photogenerated electrons may facilitate this bond cleavage.

Overall, in this thesis, we have explored, via periodic DFT calculations, the reaction mechanisms for electrocatalytic cyanide reduction and photothermal ammonia decomposition. The results reported herein, serve to pave the way towards a viable and sustainable circular nitrogen economy.

7.2 Future Works

7.2.1 Electrochemical Cyanide Reduction

Using nitrate reduction as a proof of concept, we have investigated the electrocatalytic reduction of cyanide for ammonia. While we have performed thorough mechanistic studies on this reduction reaction, this is an unexplored frontier in chemistry, with scant associated experimental or theoretical studies. We believe that the results within this thesis, highlight the need to utilise already fixed sources of nitrogen in a circular manner. Should we manage to close to loop between fixed nitrogen and ammonia would we need to activate atmospheric nitrogen? Transferring to a circular economy is proving to be a necessity, and it is very likely that a new circular economy will be based on nitrogen. Admittedly, this is a monumental task, and is a lot easier said than done. In the meantime, and aside from wishing that more attention be placed on the reduction of cyanide, we would like to propose some future works.

Chapter 4 of this thesis investigated the mechanism of cyanide reduction, specifically NaCN. Initially, the cation (Na^+) was placed on top of the surface, alongside the anion (CN^-), however it was moved below the slab so as to isolate the reduction of cyanide from any cationic effects. The role of the cation has been investigated heavily in regard to the field of CO_2 reduction. Hori and Murata displayed that for an electrolyte, $AHCO_3$ (A = Li, Na, K, Cs), HER was preferred with Li, whereas for all other candidates, the reduction of CO_2 occurred.[289] Regarding theoretical models, several joint experimental and theoretical works have been performed investigating cationic effects for CO_2 reduction, with reports of alkali metal cations hydrated in the electrochemical double layer inducing a dipole that has a stabilising effect on adsorbates.[290] As such, cationic effects warrant extensive investigation. Additionally, Augustynski *et al*.[82] reports small amounts of C_2 hydrocarbons following the reduction of cyanide. Mechanistic studies focused on C–N bond breaking and the formation of C_2 products could be investigated alongside studies focused on competition with HER.

Chapter 5 can be viewed as a chapter that is focused on bridging experiment and theory, investigating different methods for the representation of the metal-water interface, and how these methods influence our models. We have focused heavily on how the solvent is modelled, yet we have neglected to account for the dynamic nature of the aqueous environment and how that affects the binding of reaction intermediates. As such, future studies could focus on the use of ab initio molecular dynamics, or perhaps quantum mechanics/molecular mechanics (QM/MM) approaches. We also note that, from looking at experimentally derived Pourbaix diagrams, the nickel cathode can exist as an oxide.[291] Mechanistic studies should be performed investigating the performance of these systems. We have also deviated from the CHE model by including the applied bias dynamically in our calculations. However, the *a posteriori* correction applied by the CHE model also accounts for the pH of the system and as of yet, it is unclear how to incorporate this variable into our simulations.

7.2.2 Photothermal Ammonia Decomposition

Chapter 6 is the finale of this thesis, both literally and thematically. Following our studies on ammonia synthesis, we investigate its catalytic decomposition so that ammonia may be employed for the chemical storage of hydrogen. The Fe@C catalyst investigated in this work is a MOF derived material, constructed via pyrolysis and as such, there should be

several solid-solid interfaces present. Molecular dynamics could be useful to investigate the mechanism and end results of this pyrolysis, with the possibility for investigating any solid-solid interfaces via DFT. The use of DFT however, is not appropriate for the modelling of excited states, and therefore, processes involving light. Time dependent DFT (TD-DFT), however, allows for the modelling of excitons and may serve to provide a more accurate description of the non-thermal effects in this process. Additionally, the use of embedded correlated wavefunction methods, as performed by Carter *et al*.,[292] is an interesting, albeit presumably expensive way, to investigate excited states. Analogously to QM/MM schemes, these approaches involve a subsystem wherein a wavefunction method (configuration interaction or coupled cluster) is performed, surrounded by a system that Halas *et al*.[292] shows can be calculated at the level of DFT. Due to the expense of this method, and taking inspiration from Halas *et al*.,[99,100] perhaps only the RDSs of N–H cleavage and N–N associative desorption could be considered.

Chapter 8 Bibliography

1 P. T. Anastas and J. C. Warner, *Green chemistry: theory and practice*, Oxford University Press, Oxford, 1st Edition., 2000.

2 K. Sato, M. Aoki and R. Noyori, *Science*, 1998, **281**, 1646–1647.

3 *Closing the loop - An EU action plan for the Circular Economy*, European Commission, 2015.

4 How the EU wants to achieve a circular economy by 2050, https://www.europarl.europa.eu/topics/en/article/20210128STO96607/how-the-eu-wants-to-achieve-a-circular-economy-by-2050, (accessed 21 July 2023).

5 A. Chakravorty, *Resonance*, 2002, **7**, 3–5.

6 J. R. Jennings, Ed., *Catalytic Ammonia Synthesis: Fundamentals and Practice*, Springer US, Boston, MA, 1st Edition., 1991.

7 V. Pattabathula and J. Richardson, Introduction to Ammonia Production, https://www.aiche.org/resources/publications/cep/2016/september/introduction-ammonia-production, (accessed 24 November 2023).

8 A. Mittasch and W. Frankenburg, *Advances in Catalysis*, 1950, **2**, 81–104.

9 T. Hager, *The Alchemy of Air*, Harmony Books, New York, 2008.

10 C. Wang, S. D. C. Walsh, T. Longden, G. Palmer, I. Lutalo and R. Dargaville, *Energy Conversion and Management*, 2023, **280**, 116790.

11 H. Hirakawa, M. Hashimoto, Y. Shiraishi and T. Hirai, *ACS Catal.*, 2017, **7**, 3713–3720.

12 C. Philibert, *Renewable Energy for Industry: From green energy to green materials and fuels*, International Energy Agency, 2017.

13 G. Soloveichik, *Nature Catalysis*, 2019, **2**, 377–380.

14 A. Hellman, E. J. Baerends, M. Biczysko, T. Bligaard, C. H. Christensen, D. C. Clary, S. Dahl, R. Van Harrevelt, K. Honkala, H. Jonsson, G. J. Kroes, M. Luppi, U. Manthe, J. K. Nørskov, R. A. Olsen, J. Rossmeisl, E. Skúlason, C. S. Tautermann, A. J. C. Varandas and J. K. Vincent, *The Journal of Physical Chemistry B*, 2006, **110**, 17719–17735.

15 J. H. Montoya, C. Tsai, A. Vojvodic and J. K. Nørskov, *ChemSusChem*, 2015, **8**, 2180–2186.

16 S. L. Foster, S. I. P. Bakovic, R. D. Duda, S. Maheshwari, R. D. Milton, S. D. Minteer, M. J. Janik, J. N. Renner and L. F. Greenlee, *Nature Catalysis*, 2018, **1**, 490–500.

17 G. Ertl, D. Prigge, R. Schloegl and M. Weiss, *Journal of Catalysis*, 1983, **79**, 359–377.

18 Z. Paál, G. Ertl and S. B. Lee, *Applications of Surface Science*, 1981, **8**, 231–249.

19 G. Ertl, M. Weiss and S. B. Lee, *Chemical Physics Letters*, 1979, **60**, 391–394.

20 G. Ertl, D. Prigge, R. Schloegl and M. Weiss, *Journal of Catalysis*, 1983, **79**, 359–377.

21 T. Kandemir, M. E. Schuster, A. Senyshyn, M. Behrens and R. Schlögl, *Angewandte Chemie - International Edition*, 2013, **52**, 12723–12726.

22 R. Michalsky, A. M. Avram, B. A. Peterson, P. H. Pfromm and A. A. Peterson, *Chemical Science*, 2015, **6**, 3965–3974.

23 M. E. Gálvez, M. Halmann and A. Steinfeld, *Industrial and Engineering Chemistry Research*, 2007, **46**, 2042–2046.

24 W. Gao, J. Guo, P. Wang, Q. Wang, F. Chang, Q. Pei, W. Zhang, L. Liu and P. Chen, *Nature Energy*, 2018, **3**, 1067–1075.

25 S. F. Nielsen, D. Peters and O. Axelsson, *Synthetic Communications*, 2000, **30**, 3501–3509.

26 S. L. James, C. J. Adams, C. Bolm, D. Braga, P. Collier, T. Friić, F. Grepioni, K. D. M. Harris, G. Hyett, W. Jones, A. Krebs, J. MacK, L. Maini, A. G. Orpen, I. P. Parkin, W. C. Shearouse, J. W. Steed and D. C. Waddell, *Chemical Society Reviews*, 2012, 413–447.

27 G.-F. Han, F. Li, Z.-W. Chen, C. Coppex, S.-J. Kim, H.-J. Noh, Z. Fu, Y. Lu, C. V. Singh, S. Siahrostami, Q. Jiang and J.-B. Baek, *Nature Nanotechnology*, 2020, **16**, 325–330.

28 K. H. R. Rouwenhorst, H. H. Kim and L. Lefferts, *ACS Sustainable Chemistry and Engineering*, 2019, **7**, 17515–17522.

29 P. Mehta, P. Barboun, F. A. Herrera, J. Kim, P. Rumbach, D. B. Go, J. C. Hicks and W. F. Schneider, *Nature Catalysis*, 2018, **1**, 269–275.

30 M. Carmo, D. L. Fritz, J. Mergel and D. Stolten, *International Journal of Hydrogen Energy*, 2013, **38**, 4901–4934.

31 H. Kojima, K. Nagasawa, N. Todoroki, Y. Ito, T. Matsui and R. Nakajima, *International Journal of Hydrogen Energy*, 2023, **48**, 4572–4593.

32 A. Hauch, R. Küngas, P. Blennow, A. B. Hansen, J. B. Hansen, B. V. Mathiesen and M. B. Mogensen, *Science*, 2020, **370**, eaba6118.

33 N. Salmon and R. Bañares-Alcántara, *Sustainable Energy Fuels*, 2021, **5**, 2814–2839.

34 M. Nasser and H. Hassan, *Energy Conversion and Management*, 2023, **278**, 116693.

35 B. Lee, D. Lim, H. Lee and H. Lim, *Renewable and Sustainable Energy Reviews*, 2021, **143**, 110963.

36 B. Hinnemann and J. K. Nørskov, *Journal of the American Chemical Society*, 2003, **125**, 1466–1467.

37 B. Hinnemann and J. K. Nørskov, *Topics in Catalysis*, 2006, **37**, 55–70.

38 J. Rosing and E. C. Slater, *BBA - Bioenergetics*, 1972, **267**, 275–290.

39 J. Chatt, J. R. Dilworth and R. L. Richards, *Chemical Reviews*, 1978, **78**, 589–625.

40 Q. Li, L. He, C. Sun and X. Zhang, *Journal of Physical Chemistry C*, 2017, **121**, 27563–27568.

41 G. Duan, Y. Chen, Y. Tang, K. A. M. Gasem, P. Wan, D. Ding and M. Fan, *Progress in Energy and Combustion Science*, 2020, **81**, 100860.

42 J. Rittle and J. C. Peters, *Journal of the American Chemical Society*, 2016, **138**, 4243–4248.

43 E. Skúlason, T. Bligaard, S. Gudmundsdóttir, F. Studt, J. Rossmeisl, F. Abild-Pedersen, T. Vegge, H. Jónsson and J. K. Nørskov, *Physical Chemistry Chemical Physics*, 2012, **14**, 1235–1245.

44 P. Mars and D. W. Van Krevelen, *Chemical Engineering Science*, 1954, **3**, 41–59.

45 Y. Abghoui and E. Skúlason, *Catalysis Today*, 2017, **286**, 69–77.

46 M. Gudmundsson, V. Ellingsson, E. Skúlason and Y. Abghoui, *Top Catal*, 2022, **65**, 252–261.

47 S. Z. Andersen, V. Čolić, S. Yang, J. A. Schwalbe, A. C. Nielander, J. M. McEnaney, K. Enemark-Rasmussen, J. G. Baker, A. R. Singh, B. A. Rohr, M. J. Statt, S. J. Blair, S. Mezzavilla, J. Kibsgaard, P. C. K. Vesborg, M. Cargnello, S. F. Bent, T. F. Jaramillo, I. E. L. Stephens, J. K. Nørskov and I. Chorkendorff, *Nature*, 2019, **570**, 504–508.

48 C. Tang and S.-Z. Qiao, *Chemical Society Reviews*, 2019, **48**, 3166–3180.

49 J. Choi, B. H. R. Suryanto, D. Wang, H.-L. Du, R. Y. Hodgetts, F. M. Ferrero Vallana, D. R. MacFarlane and A. N. Simonov, *Nature Communications*, 2020, **11**, 5546.

50 B. H. R. Suryanto, H.-L. Du, D. Wang, J. Chen, A. N. Simonov and D. R. MacFarlane, *Nature Catalysis*, 2019, **2**, 290–296.

51 D. R. MacFarlane, P. V. Cherepanov, J. Choi, B. H. R. Suryanto, R. Y. Hodgetts, J. M. Bakker, F. M. Ferrero Vallana and A. N. Simonov, *Joule*, 2020, **4**, 1186–1205.

52 A. Tsuneto, A. Kudo and T. Sakata, *Chemistry Letters*, 1993, **22**, 851–854.

53 S. Li, Y. Zhou, K. Li, M. Saccoccio, R. Sažinas, S. Z. Andersen, J. B. Pedersen, X. Fu, V. Shadravan, D. Chakraborty, J. Kibsgaard, P. C. K. Vesborg, J. K. Nørskov and I. Chorkendorff, *Joule*, 2022, **6**, 2083–2101.

54 H.-L. Du, M. Chatti, R. Y. Hodgetts, P. V. Cherepanov, C. K. Nguyen, K. Matuszek, D. R. MacFarlane and A. N. Simonov, *Nature*, 2022, **609**, 722–727.

55 R. Tort, A. Bagger, O. Westhead, Y. Kondo, A. Khobnya, A. Winiwarter, B. J. V. Davies, A. Walsh, Y. Katayama, Y. Yamada, M. P. Ryan, M.-M. Titirici and I. E. L. Stephens, *ACS Catalysis*, 2023, **13**, 14513–14522.

56 H. Xu, Y. Ma, J. Chen, W. Zhang and J. Yang, *Chemical Society Reviews*, 2022, **51**, 2710–2758.

57 What is Groundwater?, https://www.un-igrac.org/what-groundwater, (accessed 23 July 2023).

58 U. Lall, L. Josset and T. Russo, *Annual Review of Environment and Resources*, 2020, **45**, 171–194.

59 M. A. Sutton, C. M. Howard, J. W. Erisman, G. Billen, A. Bleeker, P. Grennfelt, H. Van Grinsven and B. Grizzetti, Eds., *The European Nitrogen Assessment: Sources, Effects and Policy Perspectives*, Cambridge University Press, 1st Edition., 2011.

60 M. Duca and M. T. M. Koper, *Energy & Environmental Science*, 2012, **5**, 9726.

61 R. J. Diaz and R. Rosenberg, *Science*, 2008, **321**, 926–929.

62 A. Rajta, R. Bhatia, H. Setia and P. Pathania, *Journal of Applied Microbiology*, 2020, **128**, 1261–1278.

63 A. Cuesta and M. Escudero, *Physical Chemistry Chemistry Physics*, 2008, **10**, 3628.

64 V. Rosca, G. L. Beltramo and M. T. M. Koper, *Langmuir*, 2005, **21**, 1448–1456.

65 Y. Wang, A. Xu, Z. Wang, L. Huang, J. Li, F. Li, J. Wicks, M. Luo, D.-H. Nam, C.-S. Tan, Y. Ding, J. Wu, Y. Lum, C.-T. Dinh, D. Sinton, G. Zheng and E. H. Sargent, *Journal of the American Chemical Society*, 2020, **142**, 5702–5708.

66 J. Li, G. Zhan, J. Yang, F. Quan, C. Mao, Y. Liu, B. Wang, F. Lei, L. Li, A. W. M. Chan, L. Xu, Y. Shi, Y. Du, W. Hao, P. K. Wong, J. Wang, S.-X. Dou, L. Zhang and J. C. Yu, *Journal of the American Chemical Society*, 2020, **142**, 7036–7046.

67 D. A. Dzombak, R. S. Ghosh and G. M. Wong-Chong, *Cyanide in water and soil: chemistry, risk, and management*, CRC/Taylor & Francis, Boca Raton, 2006.

68 E. Jaszczak, Ż. Polkowska, S. Narkowicz and J. Namieśnik, *Environmental Science and Pollution Research*, 2017, **24**, 15929–15948.

69 M. Zagrobelny, S. Bak and B. L. Møller, *Phytochemistry*, 2008, **69**, 1457–1468.

70 R. M. Gleadow and B. L. Møller, *Annual Review of Plant Biology*, 2014, **65**, 155–185.

71 G. Volpi, *Journal of Chemical Education*, 2016, **93**, 891–897.

72 N. Kuyucak and A. Akcil, *Minerals Engineering*, 2013, **50–51**, 13–29.

73 P. D. Kondos, G. Deschênes and R. M. Morrison, *Hydrometallurgy*, 1995, **39**, 235–250.

74 C. N. Mpinga, S. M. Bradshaw, G. Akdogan, C. A. Snyders and J. J. Eksteen, *Hydrometallurgy*, 2014, **142**, 36–46.

75 G. J. Zagury, K. Oudjehani and L. Deschênes, *Science of The Total Environment*, 2004, **320**, 211–224.

76 K. Dong, F. Xie, W. Wang, Y. Chang, D. Lu, X. Gu and C. Chen, *Journal of Cleaner Production*, 2021, **302**, 126946.

77 H. Vapur and O. Bayat, *Minerals Engineering*, 2007, **20**, 729–737.

78 R. W. F. Hardy and E. Knight, *Biochimica et Biophysica Acta (BBA) - Enzymology*, 1967, **139**, 69–90.

79 C. C. Lee, Y. Hu and M. W. Ribbe, *Angewandte Chemie - International Edition*, 2012, **51**, 1947–1949.

80 C. C. Lee, Y. Hu and M. W. Ribbe, *Angewandte Chemie - International Edition*, 2015, **54**, 1219–1222.

81 J. Rittle and J. C. Peters, *Angewandte Chemie - International Edition*, 2016, **55**, 12262–12265.

82 M. Fedurco, C. J. Sartoretti and J. Augustynski, *Journal of The Electrochemical Society*, 2001, **148**, D19.

83 A. Valera-Medina, H. Xiao, M. Owen-Jones, W. I. F. David and P. J. Bowen, *Progress in Energy and Combustion Science*, 2018, **69**, 63–102.

84 N. Morlanés, S. P. Katikaneni, S. N. Paglieri, A. Harale, B. Solami, S. M. Sarathy and J. Gascon, *Chemical Engineering Journal*, 2021, **408**, 127310.

85 F. Schüth, R. Palkovits, R. Schlögl and D. S. Su, *Energy Environ. Sci.*, 2012, **5**, 6278–6289.

86 A. Klerke, C. H. Christensen, J. K. Nørskov and T. Vegge, *Journal of Materials Chemistry*, 2008, **18**, 2304.

87 S. Peters, A. M. Abdel-Mageed and S. Wohlrab, *ChemCatChem*, 2023, **15**, e202201185.

88 J. C. Ganley, F. S. Thomas, E. G. Seebauer and R. I. Masel, *Catalysis Letters*, 2004, **96**, 117–122.

89 S. F. Yin, B. Q. Xu, X. P. Zhou and C. T. Au, *Applied Catalysis A: General*, 2004, **277**, 1–9.

90 S. F. Yin, B. Q. Xu, W. X. Zhu, C. F. Ng, X. P. Zhou and C. T. Au, *Catalysis Today*, 2004, **93–95**, 27–38.

91 S. J. Wang, S. F. Yin, L. Li, B. Q. Xu, C. F. Ng and C. T. Au, *Applied Catalysis B: Environmental*, 2004, **52**, 287–299.

92 Z. Zhang, S. Liguori, T. F. Fuerst, J. D. Way and C. A. Wolden, *ACS Sustainable Chemistry & Engineering*, 2019, **7**, 5975–5985.

93 J. Yang, D. He, W. Chen, W. Zhu, H. Zhang, S. Ren, X. Wang, Q. Yang, Y. Wu and Y. Li, *ACS Applied Materials & Interfaces*, 2017, **9**, 39450–39455.

94 P. Yu, J. Guo, L. Liu, P. Wang, F. Chang, H. Wang, X. Ju and P. Chen, *The Journal of Physical Chemistry C*, 2016, **120**, 2822–2828.

95 C. Chen, K. Wu, H. Ren, C. Zhou, Y. Luo, L. Lin, C. Au and L. Jiang, *Energy Fuels*, 2021, **35**, 11693–11706.

96 A. Gellé, T. Jin, L. De La Garza, G. D. Price, L. V. Besteiro and A. Moores, *Chemical Reviews*, 2020, **120**, 986–1041.

97 D. Mateo, J. L. Cerrillo, S. Durini and J. Gascon, *Chemical Society Reviews*, 2021, **50**, 2173–2210.

98 M. L. Brongersma, N. J. Halas and P. Nordlander, *Nature Nanotech*, 2015, **10**, 25–34.

99 L. Zhou, D. F. Swearer, C. Zhang, H. Robatjazi, H. Zhao, L. Henderson, L. Dong, P. Christopher, E. A. Carter, P. Nordlander and N. J. Halas, *Science*, 2018, **362**, 69–72.

100 Y. Yuan, L. Zhou, H. Robatjazi, J. L. Bao, J. Zhou, A. Bayles, L. Yuan, M. Lou, M. Lou, S. Khatiwada, E. A. Carter, P. Nordlander and N. J. Halas, *Science*, 2022, **378**, 889–893.

101 N. C. Handy, in *Lecture Notes in Quantum Chemistry II*, ed. B. O. Roos, Springer Berlin Heidelberg, Berlin, Heidelberg, 1994, vol. 64, pp. 91–124.

102 P. Hohenberg and W. Kohn, *Physical Review*, 1964, **136**, B864–B871.

103 W. Kohn and L. J. Sham, *Physical Review*, 1965, **140**, A1133–A1138.

104 D. M. Ceperley and B. J. Alder, *Physical Review Letters*, 1980, **45**, 566–569.

105 S. H. Vosko, L. Wilk and M. Nusair, *Canadian Journal of Physics*, 1980, **58**, 1200–1211.

106 C. J. Cramer, in *John Wiley & Sons Ltd*, 2004.

107 J. P. Perdew, K. Burke and M. Ernzerhof, *Physical Review Letters*, 1996, **77**, 3865–3868.

108 M. Swart, DFT2022 poll, https://www.marcelswart.eu/dft-poll/news2022.pdf, (accessed 3 July 2023).

109 J. Wellendorff, K. T. Lundgaard, A. Møgelhøj, V. Petzold, D. D. Landis, J. K. Nørskov, T. Bligaard and K. W. Jacobsen, *Physical Review B - Condensed Matter and Materials Physics*, 2012, **85**, 235149.

110 J. P. Wagner and P. R. Schreiner, *Angewandte Chemie - International Edition*, 2015, **54**, 12274–12296.

111 W. Koch and M. C. Holthausen, *A Chemist's Guide to Density Functional Theory*, Wiley, 1st Edition., 2001.

112 L. Goerigk, *J. Phys. Chem. Lett.*, 2015, **6**, 3891–3896.

113 N. Mardirossian and M. Head-Gordon, *Journal of Chemical Theory and Computation*, 2016, **12**, 4303–4325.

114 K. Lee, É. D. Murray, L. Kong, B. I. Lundqvist and D. C. Langreth, *Physical Review B - Condensed Matter and Materials Physics*, 2010, **82**, 081011-(1-4).

115 S. L. Dudarev, G. A. Botton, S. Y. Savrasov, C. J. Humphreys and A. P. Sutton, *Physical Review B*, 1998, **57**, 1505–1509.

116 M. Cococcioni and S. De Gironcoli, *Physical Review B*, 2005, **71**, 035105.

117 S. Lany and A. Zunger, *Physical Review B*, 2009, **80**, 085202.

118 J. P. Allen and G. W. Watson, *Physical Chemistry Chemical Physics*, 2014, **16**, 21016–21031.

119 M. C. Payne, M. P. Teter, D. C. Allan, T. A. Arias and J. D. Joannopoulos, *Reviews of Modern Physics*, 1992, **64**, 1045–1097.

120 G. Henkelman and H. Jónsson, *The Journal of Chemical Physics*, 2000, **113**, 9978–9985.

121 G. Henkelman, B. P. Uberuaga and H. Jónsson, *The Journal of Chemical Physics*, 2000, **113**, 9901–9904.

122 G. Henkelman and H. Jónsson, *The Journal of Chemical Physics*, 1999, **111**, 7010–7022.

123 A. Heyden, A. T. Bell and F. J. Keil, *The Journal of Chemical Physics*, 2005, **123**, 224101.

124 A. Jain, S. P. Ong, G. Hautier, W. Chen, W. D. Richards, S. Dacek, S. Cholia, D. Gunter, D. Skinner, G. Ceder, and others, *APL materials*, 2013, **1**, 011002.

125 R. T. Downs and M. Hall-Wallace, *American Mineralogist*, 2003, **88**, 247–250.

126 S. Gražulis, D. Chateigner, R. T. Downs, A. F. T. Yokochi, M. Quirós, L. Lutterotti, E. Manakova, J. Butkus, P. Moeck and A. Le Bail, *Journal of Applied Crystallography*, 2009, **42**, 726–729.

127 S. Gražulis, A. Daškevič, A. Merkys, D. Chateigner, L. Lutterotti, M. Quirós, N. R. Serebryanaya, P. Moeck, R. T. Downs and A. Le Bail, *Nucleic Acids Research*, 2012, **40**, D420–D427.

128 S. Gražulis, A. Merkys, A. Vaitkus and M. Okulič-Kazarinas, *Journal of Applied Crystallography*, 2015, **48**, 85–91.

129 A. Merkys, A. Vaitkus, J. Butkus, M. Okulič-Kazarinas, V. Kairys and S. Gražulis, *Journal of Applied Crystallography*, 2016, **49**, 292–301.

130 M. Quirós, S. Gražulis, S. Girdzijauskaitė, A. Merkys and A. Vaitkus, *Journal of Cheminformatics*, 2018, **10**, 23.

131 A. Vaitkus, A. Merkys and S. Gražulis, *Journal of Applied Crystallography*, 2021, **54**, 661–672.

132 A. Merkys, A. Vaitkus, A. Grybauskas, A. Konovalovas, M. Quirós and S. Gražulis, *Journal of Cheminformatics*, 2023, **15**, 25.

133 A. Vaitkus, A. Merkys, T. Sander, M. Quirós, P. A. Thiessen, E. E. Bolton and S. Gražulis, *Journal of Cheminformatics*, 2023, **15**, 123.

134 J. E. Saal, S. Kirklin, M. Aykol, B. Meredig and C. Wolverton, *JOM*, 2013, **65**, 1501–1509.

135 S. Kirklin, J. E. Saal, B. Meredig, A. Thompson, J. W. Doak, M. Aykol, S. Rühl and C. Wolverton, *npj Computational Materials*, 2015, **1**, 15010.

136 R. Sundararaman and K. Schwarz, *The Journal of Chemical Physics*, 2017, **146**, 084111.

137 H. H. Heenen, J. A. Gauthier, H. H. Kristoffersen, T. Ludwig and K. Chan, *The Journal of Chemical Physics*, 2020, **152**, 144703.

138 J. A. Gauthier, S. Ringe, C. F. Dickens, A. J. Garza, A. T. Bell, M. Head-Gordon, J. K. Nørskov and K. Chan, *ACS Catalysis*, 2019, **9**, 920–931.

139 K. Mathew, R. Sundararaman, K. Letchworth-Weaver, T. A. Arias and R. G. Hennig, *The Journal of Chemical Physics*, 2014, **140**, 084106.

140 K. Mathew, V. S. C. Kolluru, S. Mula, S. N. Steinmann and R. G. Hennig, *The Journal of Chemical Physics*, 2019, **151**, 234101.

141 D. Gunceler, K. Letchworth-Weaver, R. Sundararaman, K. A. Schwarz and T. A. Arias, *Modelling and Simulation in Materials Science and Engineering*, 2013, **21**, 074005.

142 J. VandeVondele, F. Mohamed, M. Krack, J. Hutter, M. Sprik and M. Parrinello, *The Journal of Chemical Physics*, 2005, **122**, 014515.

143 M. J. Gillan, D. Alfè and A. Michaelides, *The Journal of Chemical Physics*, 2016, **144**, 130901.

144 X. He, Y. Zhu, A. Epstein and Y. Mo, *npj Computational Materials*, 2018, **4**, 18.

145 E. Tayyebi, Y. Abghoui and E. Skúlason, *ACS Catalysis*, 2019, **9**, 11137–11145.

146 Á. B. Höskuldsson, E. Tayyebi and E. Skúlason, *Journal of Catalysis*, 2021, **404**, 362–370.

147 J. K. Nørskov, J. Rossmeisl, A. Logadottir, L. Lindqvist, J. R. Kitchin, T. Bligaard and H. Jónsson, *Journal of Physical Chemistry B*, 2004, **108**, 17886–17892.

148 W. Schmickler and E. Santos, *Interfacial Electrochemistry*, Springer Berlin Heidelberg, Berlin, Heidelberg, 2010.

149 J. A. Gauthier, C. F. Dickens, L. D. Chen, A. D. Doyle and J. K. Nørskov, *The Journal of Physical Chemistry C*, 2017, **121**, 11455–11463.

150 C. Shi, C. P. O'Grady, A. A. Peterson, H. A. Hansen and J. K. Nørskov, *Physical Chemistry Chemical Physics*, 2013, **15**, 7114.

151 M. Henderson, *Surface Science Reports*, 2002, **46**, 1–308.

152 H. Ogasawara, B. Brena, D. Nordlund, M. Nyberg, A. Pelmenschikov, L. G. M. Pettersson and A. Nilsson, *Phys. Rev. Lett.*, 2002, **89**, 276102.

153 S. Schnur and A. Groß, *New Journal of Physics*, 2009, **11**, 125003.

154 A. Michaelides, *Applied Physics A*, 2006, **85**, 415–425.

155 A. Michaelides, A. Alavi and D. A. King, *Physical Review B*, 2004, **69**, 113404.

156 E. Skúlason, G. S. Karlberg, J. Rossmeisl, T. Bligaard, J. Greeley, H. Jónsson and J. K. Nørskov, *Physical Chemistry Chemical Physics*, 2007, **9**, 3241–3250.

157 L. D. Chen, M. Bajdich, J. M. P. Martirez, C. M. Krauter, J. A. Gauthier, E. A. Carter, A. C. Luntz, K. Chan and J. K. Nørskov, *Nature Communications*, 2018, **9**, 3202.

158 K. Chan and J. K. Nørskov, *The Journal of Physical Chemistry Letters*, 2015, **6**, 2663–2668.

159 J. Rossmeisl, E. Skúlason, M. E. Björketun, V. Tripkovic and J. K. Nørskov, *Chemical Physics Letters*, 2008, **466**, 68–71.

160 G. Di Liberto and L. Giordano, *Electrochemical Science Advances*, 2023, **4**, e2100204.

161 A. Rendón-Calle, S. Builes and F. Calle-Vallejo, *Applied Catalysis B: Environmental*, 2020, **276**, 119147.

162 Y. Basdogan, A. M. Maldonado and J. A. Keith, *WIREs Computational Molecular Science*, 2020, **10**, e1446.

163 R. F. W. Bader, *Atoms in Molecules: A Quantum Theory*, Clarendon Press, 1994.

164 E. Sanville, S. D. Kenny, R. Smith and G. Henkelman, *Journal of Computational Chemistry*, 2007, **28**, 899–908.

165 A. Otero-de-la-Roza, M. A. Blanco, A. M. Pendás and V. Luaña, *Computer Physics Communications*, 2009, **180**, 157–166.

166 A. Otero-de-la-Roza, E. R. Johnson and V. Luaña, *Computer Physics Communications*, 2014, **185**, 1007–1018.

167 J. Contreras-García, E. R. Johnson, S. Keinan, R. Chaudret, J.-P. Piquemal, D. N. Beratan and W. Yang, *Journal of Chemical Theory and Computation*, 2011, **7**, 625–632.

168 E. R. Johnson, S. Keinan, P. Mori-Sánchez, J. Contreras-García, A. J. Cohen and W. Yang, *Journal of the American Chemical Society*, 2010, **132**, 6498–6506.

169 L. M. Torres, A. F. Gil, L. Galicia and I. González, *Journal of Chemical Education*, 1996, **73**, 808.

170 A. J. Bard, L. R. Faulkner and H. S. White, *Electrochemical methods: fundamentals and applications*, John Wiley & Sons, Ltd., Hoboken, NJ, 3rd Edition., 2022.

171 S. Kurth, J. P. Perdew and P. Blaha, *International Journal of Quantum Chemistry*, 1999, **75**, 889–909.

172 H. Oberhofer, in *Handbook of Materials Modeling*, eds. W. Andreoni and S. Yip, Springer International Publishing, Cham, 2020, pp. 1505–1537.

173 A. Ciotti and M. García-Melchor, *Current Opinion in Electrochemistry*, 2023, **42**, 101402.

174 S. Trasatti, *Electrochimica Acta*, 1990, **35**, 269–271.

175 S. Trasatti, *Pure and Applied Chemistry*, 1986, **58**, 955–966.

176 M. Van den Bossche, E. Skúlason, C. Rose-Petruck and H. Jónsson, *The Journal of Physical Chemistry C*, 2019, **123**, 4116–4124.

177 L. Wang, M. Xia, H. Wang, K. Huang, C. Qian, C. T. Maravelias and G. A. Ozin, *Joule*, 2018, **2**, 1055–1074.

178 H. Stam, A. H. Stouthamer and H. W. van Verseveld, *FEMS Microbiology Letters*, 1987, **46**, 73–92.

179 B. Hinnemann and J. K. Nørskov, *Topics in Catalysis*, 2006, **37**, 55–70.

180 L. Pospíšil, J. Bulíčková, M. Hromadová, M. Gál, S. Civiš, J. Cihelka and J. Tarábek, *Chemical Communications*, 2007, 2270–2272.

181 R. Lan, K. A. Alkhazmi, I. A. Amar and S. Tao, *Electrochimica Acta*, 2014, **123**, 582–587.

182 X. Guo, Y. Zhu and T. Ma, *Journal of Energy Chemistry*, 2017, **26**, 1107–1116.

183 B. D. Darwent, in *National Standard Reference Data System, National Bureau of Standards*, 1970, p. 23.

184 V. M. Luque-Almagro, M. J. Huertas, M. Martínez-Luque, C. Moreno-Vivián, M. D. Roldán, L. J. García-Gil, F. Castillo and R. Blasco, *Applied and Environmental Microbiology*, 2005, **71**, 940–947.

185 R. J. Geller, C. Barthold, J. A. Saiers and A. H. Hall, *Pediatrics*, 2006, **118**, 2146–2158.

186 K. Brennan, G. W. Watson and M. García-Melchor, *Catalysis Science & Technology*, 2021, **11**, 5633–5640.

187 P. E. Blöchl, *Physical Review B*, 1994, **50**, 17953–17979.

188 G. Kresse and J. Furthmüller, *Computational Materials Science*, 1996, **6**, 15–50.

189 G. Kresse and J. Furthmüller, *Physical Review B - Condensed Matter and Materials Physics*, 1996, **54**, 11169–11186.

190 J. E. Angelo, N. R. Moody and M. I. Baskes, *Modelling and Simulation in Materials Science and Engineering*, 1995, **3**, 289–307.

191 F. Mittendorfer, A. Eichler and J. Hafner, *Surface Science*, 1999, **423**, 1–11.

192 H. A. Mook, *Physical Review*, 1966, **148**, 495–501.

193 A. Hjorth Larsen, J. JØrgen Mortensen, J. Blomqvist, I. E. Castelli, R. Christensen, M. Dułak, J. Friis, M. N. Groves, B. Hammer, C. Hargus, E. D. Hermes, P. C. Jennings, P. Bjerre Jensen, J. Kermode, J. R. Kitchin, E. Leonhard Kolsbjerg, J. Kubal, K. Kaasbjerg, S. Lysgaard, J. Bergmann Maronsson, T. Maxson, T. Olsen, L. Pastewka, A. Peterson, C. Rostgaard, J. SchiØtz, O. Schütt, M. Strange, K. S. Thygesen, T. Vegge, L. Vilhelmsen, M. Walter, Z. Zeng and K. W. Jacobsen, *Journal of Physics Condensed Matter*, 2017, **29**, 273002.

194 X. Cui, C. Tang and Q. Zhang, *Advanced Energy Materials*, 2018, **8**, 1800369.

195 B. M. Hoffman, D. Lukoyanov, Z. Y. Yang, D. R. Dean and L. C. Seefeldt, *Chemical Reviews*, 2014, **114**, 4041–4062.

196 M. Fedurco, C. J. Sartoretti and J. Augustynski, *Journal of The Electrochemical Society*, 2001, **148**, D19.

197 H. Yang and J. L. Whitten, *The Journal of Chemical Physics*, 1993, **98**, 5039.

198 V. Tripković, E. Skúlason, S. Siahrostami, J. K. Nørskov and J. Rossmeisl, *Electrochimica Acta*, 2010, **55**, 7975–7981.

199 J. H. Baraban, P. B. Changala, G. Ch. Mellau, J. F. Stanton, A. J. Merer and R. W. Field, *Science*, 2015, **350**, 1338–1342.

200 Z. W. Seh, J. Kibsgaard, C. F. Dickens, I. Chorkendorff, J. K. Nørskov and T. F. Jaramillo, *Science*, 2017, **355**, eaad4998.

201 X. Zhao, G. Hu, G. Chen, H. Zhang, S. Zhang and H. Wang, *Advanced Materials*, 2021, **33**, 2007650.

202 S. Hammes-Schiffer and G. Galli, *Nature Energy*, 2021, **6**, 700–705.

203 R. Sundararaman, D. Vigil-Fowler and K. Schwarz, *Chemical Reviews*, 2022, **122**, 10651–10674.

204 S. Maheshwari, G. Rostamikia and M. J. Janik, *The Journal of Chemical Physics*, 2019, **150**, 041708.

205 X. Nie, M. R. Esopi, M. J. Janik and A. Asthagiri, *Angewandte Chemie - International Edition*, 2013, **52**, 2459–2462.

206 E. Romeo, F. Illas and F. Calle-Vallejo, *The Journal of Physical Chemistry C*, 2023, **127**, 10134–10139.

207 M. M. Montemore, O. Andreussi and J. W. Medlin, *The Journal of Chemical Physics*, 2016, **145**, 074702.

208 T. Roman and A. Groß, *Catalysis Today*, 2013, **202**, 183–190.

209 M. T. Tang, X. Liu, Y. Ji, J. K. Norskov and K. Chan, *The Journal of Physical Chemistry C*, 2020, **124**, 28083–28092.

210 S. Ringe, N. G. Hörmann, H. Oberhofer and K. Reuter, *Chemical Reviews*, 2022, **122**, 10777–10820.

211 Y.-H. Fang and Z.-P. Liu, *Journal of the American Chemical Society*, 2010, **132**, 18214–18222.

212 C. D. Taylor, S. A. Wasileski, J.-S. Filhol and M. Neurock, *Physical Review B*, 2006, **73**, 165402.

213 M. Garcia-Ratés and N. López, *Journal of Chemical Theory and Computation*, 2016, **12**, 1331–1341.

214 M. Van den Bossche, C. Rose-Petruck and H. Jónsson, *The Journal of Physical Chemistry C*, 2021, **125**, 13802–13808.

215 J. D. Goodpaster, A. T. Bell and M. Head-Gordon, *The Journal of Physical Chemistry Letters*, 2016, **7**, 1471–1477.

216 W. Zhang, F.-L. Sun, Q.-J. Fang, Y.-F. Yu, J.-K. Pan, J.-G. Wang and G.-L. Zhuang, *The Journal of Physical Chemistry C*, 2022, **126**, 2349–2364.

217 C. Cui, J. Han, X. Zhu, X. Liu, H. Wang, D. Mei and Q. Ge, *Journal of Catalysis*, 2016, **343**, 257–265.

218 Q. Zhang and A. Asthagiri, *Catalysis Today*, 2019, **323**, 35–43.

219 U. Benedikt, W. B. Schneider and A. A. Auer, *Physical Chemistry Chemical Physics*, 2013, **15**, 2712.

220 E. Tayyebi, Á. B. Höskuldsson, A. Wark, N. Atrak, B. M. Comer, A. J. Medford and E. Skúlason, *The Journal of Physical Chemistry Letters*, 2022, **13**, 6123–6129.

221 Y. A. Alsunni, A. W. Alherz and C. B. Musgrave, *The Journal of Physical Chemistry C*, 2021, **125**, 23773–23783.

222 IEA, *Ammonia Technology Roadmap*, Paris, 2021.

223 R. R. Dash, A. Gaur and C. Balomajumder, *Journal of Hazardous Materials*, 2009, **163**, 1–11.

224 M. Rezaul Haque and J. Howard Bradbury, *Food Chemistry*, 2002, **77**, 107–114.

225 K. Brennan, G. W. Watson and M. García-Melchor, *Catalysis Science & Technology*, 2024, **14**, 1043–1051.

226 G. Kresse and J. Furthmüller, *Computational Materials Science*, 1996, **6**, 15–50.

227 H. Jónsson, G. Mills and K. W. Jacobsen, in *Classical and Quantum Dynamics in Condensed Phase Simulations*, World Scientific, Lerici, Villa Marigola, 1998, pp. 385–404.

228 G. W. Watson, R. P. K. Wells, D. J. Willock and G. J. Hutchings, *The Journal of Physical Chemistry B*, 2001, **105**, 4889–4894.

229 B. Bhatia and D. S. Sholl, *The Journal of Chemical Physics*, 2005, **122**, 204707.

230 S. Mirizadeh, S. Yaghmaei and Z. Ghobadi Nejad, *Journal of Environmental Health Science and Engineering*, 2014, **12**, 85.

231 R. Urrego-Ortiz, S. Builes and F. Calle-Vallejo, *ChemCatChem*, 2021, **13**, 2508–2516.

232 N. Agmon, *Chemical Physics Letters*, 1995, **244**, 456–462.

233 S. Niaz, T. Manzoor and A. H. Pandith, *Renewable and Sustainable Energy Reviews*, 2015, **50**, 457–469.

234 J. Ikäheimo, J. Kiviluoma, R. Weiss and H. Holttinen, *International Journal of Hydrogen Energy*, 2018, **43**, 17295–17308.

235 P. Liu, L. Sun, Z. Zhang, X. Wang, Y. Zhang and X. Yang, *Molecular Catalysis*, 2023, **543**, 113160.

236 M. Aziz, A. T. Wijayanta and A. B. D. Nandiyanto, *Energies*, 2020, **13**, 3062.

237 Ruthenium, https://pmm.umicore.com/en/prices/ruthenium/, (accessed 21 March 2024).

238 A. Fujishima and K. Honda, *Nature*, 1972, **238**, 37–38.

239 S. Sayas, N. Morlanés, S. P. Katikaneni, A. Harale, B. Solami and J. Gascon, *Catalysis Science & Technology*, 2020, **10**, 5027–5035.

240 W. Al Maksoud, R. K. Rai, N. Morlanés, M. Harb, R. Ahmad, S. Ould-Chikh, D. Anjum, M. N. Hedhili, B. E. Al-Sabban, K. Albahily, L. Cavallo and J.-M. Basset, *Journal of Catalysis*, 2021, **394**, 353–365.

241 M. He, B. Xiao, S. Liu, X. Guo, S. Luo, Z. Xu, Y. Feng and Z. Hu, *International Journal of Hydrogen Energy*, 2009, **34**, 2174–2183.

242 M. J. Kale, T. Avanesian and P. Christopher, *ACS Catalysis*, 2014, **4**, 116–128.

243 P. Christopher, H. Xin and S. Linic, *Nature Chemistry*, 2011, **3**, 467–472.

244 M. Ghoussoub, M. Xia, P. N. Duchesne, D. Segal and G. Ozin, *Energy & Environmental Science*, 2019, **12**, 1122–1142.

245 X. Li, H. O. Everitt and J. Liu, *Nano Research*, 2019, **12**, 1906–1911.

246 X. Li, X. Zhang, H. O. Everitt and J. Liu, *Nano Letters*, 2019, **19**, 1706–1711.

247 J. Wang, Y. Li, L. Deng, N. Wei, Y. Weng, S. Dong, D. Qi, J. Qiu, X. Chen and T. Wu, *Advanced Materials*, 2017, **29**, 1603730.

248 J. Wellendorff, K. T. Lundgaard, A. Møgelhøj, V. Petzold, D. D. Landis, J. K. Nørskov, T. Bligaard and K. W. Jacobsen, *Physical Review B - Condensed Matter and Materials Physics*, 2012, **85**, 32–34.

249 S. Grimme, J. Antony, S. Ehrlich and H. Krieg, *The Journal of Chemical Physics*, 2010, **132**, 154104.

250 P. Błoński and A. Kiejna, *Surface Science*, 2007, **601**, 123–133.

251 E. Aghemenloh, J. O. Umukoro, S. O. Azi, S. Yusuf and J. O. A. Idiodi, *Computational Materials Science*, 2011, **50**, 3290–3296.

252 M. Alden, S. Mirbt, H. L. Skriver, N. M. Rosengaard and B. Johansson, *Physical Review B*.

253 H. Liu and C. Di Valentin, *Journal of Physical Chemistry C*, 2017, **121**, 25736–25742.

254 S. Dudarev and G. Botton, *Physical Review B - Condensed Matter and Materials Physics*, 1998, **57**, 1505–1509.

255 D. Santos-Carballal, A. Roldan, R. Grau-Crespo and N. H. de Leeuw, *Physical Chemistry Chemical Physics*, 2014, **16**, 21082–21097.

256 J. E. Saal, S. Kirklin, M. Aykol, B. Meredig and C. Wolverton, *Jom*, 2013, **65**, 1501–1509.

257 E. J. W. Verwey, *Nature*, 1939, **144**, 327–328.

258 M. S. Senn, J. P. Wright and J. P. Attfield, *Nature*, 2012, **481**, 173–176.

259 J. P. Wright, J. Paul Attfield and P. G. Radaelli, *Physical Review B - Condensed Matter and Materials Physics*, 2002, **66**, 1–15.

260 A. Kiejna, T. Ossowski and T. Pabisiak, *Physical Review B - Condensed Matter and Materials Physics*, 2012, **85**, 1–11.

261 P. Piekarz, K. Parlinski and A. M. Oleś, *Physical Review B - Condensed Matter and Materials Physics*, 2007, **76**, 1–16.

262 J. Noh, O. I. Osman, S. G. Aziz, P. Winget and J.-L. Brédas, *Science and Technology of Advanced Materials*, 2014, **15**, 044202.

263 J. Noh, O. I. Osman, S. G. Aziz, P. Winget and J.-L. Brédas, *Chemistry of Materials*, 2015, **27**, 5856–5867.

264 A. Roldan, D. Santos-Carballal and N. H. De Leeuw, *The Journal of Chemical Physics*, 2013, **138**, 204712.

265 R. Arras, B. Warot-Fonrose and L. Calmels, *Journal of Physics: Condensed Matter*, 2013, **25**, 256002.

266 J. P. Allen and G. W. Watson, *Physical Chemistry Chemical Physics*, 2014, **16**, 21016–21031.

267 M. S. Pires, T. C. Silva, L. C. T. Lacerda, A. A. De Castro, S. Corrêa, I. S. S. De Oliveira, V. S. Vaiss, F. G. E. Nogueira and T. C. Ramalho, *Chemical Physics Letters*, 2021, **781**, 138984.

268 X. Li and J. Paier, *Journal of Physical Chemistry C*, 2016, **120**, 1056–1065.

269 G. S. Parkinson, P. Lackner, O. Gamba, S. Maaß, S. Gerhold, M. Riva, R. Bliem, U. Diebold and M. Schmid, *Surface Science*, 2016, **649**, L120–L123.

270 W. Weiss and W. Ranke, *Progress in Surface Science*, 2002, **70**, 1–151.

271 X. Yu, C. F. Huo, Y. W. Li, J. Wang and H. Jiao, *Surface Science*, 2012, **606**, 872–879.

272 U. Aschauer and A. Selloni, *The Journal of Chemical Physics*, 2015, **143**, 044705.

273 J. Ahdjoudj, C. Martinsky, C. Minot, M. A. Van Hove and G. A. Somorjai, *Surface Science*, 1999, **443**, 133–153.

274 T. Kendelewicz, P. Liu, C. S. Doyle, G. E. Brown, E. J. Nelson and S. A. Chambers, *Surface Science*, 2000, **453**, 32–46.

275 A. Hjorth Larsen, J. J. Mortensen, J. Blomqvist, I. E. Castelli, R. Christensen, M. Dułak, J. Friis, M. N. Groves, B. Hammer, C. Hargus, and others, *Journal of Physics: Condensed Matter*, 2017, **29**, 273002.

276 X. Cui, C. Wang, A. Argondizzo, S. Garrett-Roe, B. Gumhalter and H. Petek, *Nature Physics*, 2014, **10**, 505–509.

277 T. E. Bell and L. Torrente-Murciano, *Topics in Catalysis*, 2016, **59**, 1438–1457.

278 P. W. Tasker, *Journal of Physics C: Solid State Physics*, 1979, **12**, 4977–4984.

279 K. W. Kolasinski, *Surface Science: Foundations of Catalysis and Nanoscience*, Wiley, Chichester, West Sussex; Hoboken, N.J, 3rd Edition., 2012.

280 M. J. Davies, S. C. Parker and G. W. Watson, *Journal of Materials Chemistry*, 1994, **4**, 813.

281 H. Liu and C. Di Valentin, *The Journal of Physical Chemistry C*, 2017, **121**, 25736–25742.

282 J. P. Wright, J. P. Attfield and P. G. Radaelli, *Physical Review Letters*, 2001, **87**, 266401.

283 I. Leonov, A. N. Yaresko, V. N. Antonov, M. A. Korotin and V. I. Anisimov, *Physical Review Letters*, 2004, **93**, 146404.

284 H.-T. Jeng, G. Y. Guo and D. J. Huang, *Physical Review Letters*, 2004, **93**, 156403.

285 J. Schlappa, C. Schüßler-Langeheine, C. F. Chang, H. Ott, A. Tanaka, Z. Hu, M. W. Haverkort, E. Schierle, E. Weschke, G. Kaindl and L. H. Tjeng, *Physical Review Letters*, 2008, **100**, 026406.

286 S.-C. Weng, Y.-R. Lee, C.-G. Chen, C.-H. Chu, Y.-L. Soo and S.-L. Chang, *Physical Review Letters*, 2012, **108**, 146404.

287 B. Balko and G. R. Hoy, *Physica B+C*, 1977, **86–88**, 953–954.

288 F. N. Skomurski, S. Kerisit and K. M. Rosso, *Geochimica et Cosmochimica Acta*, 2010, **74**, 4234–4248.

289 A. Murata and Y. Hori, *Bulletin of the Chemical Society of Japan*, 1991, **64**, 123–127.

290 J. Resasco, L. D. Chen, E. Clark, C. Tsai, C. Hahn, T. F. Jaramillo, K. Chan and A. T. Bell, *Journal of the American Chemical Society*, 2017, **139**, 11277–11287.

291 L.-F. Huang, M. J. Hutchison, R. J. Santucci, J. R. Scully and J. M. Rondinelli, *The Journal of Physical Chemistry C*, 2017, **121**, 9782–9789.

292 F. Libisch, C. Huang and E. A. Carter, *Accounts of Chemical Research*, 2014, **47**, 2768–2775.